ON THE STRUCTURE AND PHASE SPEEDS OF THE KELVIN WAVES AND MJO OVER THE INDIAN OCEAN.

by

Ahmed Shaaban

A Dissertation

Submitted to the University at Albany, State University of New York

in Partial Fulfillment of

the Requirements for the Degree of

Doctor of Philosophy

College of Art & Sciences

Department of Atmospheric and Environmental Science
University at Albany
Albany, New York

May 2021

Parent, sister and brother.

ABSTRACT

Kelvin waves in the stratosphere are well known to behave as radiative gravity waves. Yet, the tropospheric component of these Kelvin waves (and other tropical modes) has often been described as superpositions between the baroclinic modes. By decomposing the Kelvin waves into upward and downward-phase components, we found that only upward-phase Kelvin waves occupy the troposphere, indicating that the tropospheric Kelvin waves are not vertical standing oscillations as previously thought. Fast Kelvin waves were found to obey the structure of radiating gravity waves, like their stratospheric counterpart, more than the moist waves. The unexpected lack of variation in vertical tilt of tropospheric Kelvin waves suggest than fast tropospheric waves exist in high static stability environments when compared to slow waves. Limitations of the radiative view of the Kelvin waves are discussed.

The second part of this dissertation focuses on the behavior of the stratospheric Kelvin waves when approaching critical layers, where the phase speed of the waves in an atmosphere at rest would match the speed of the background flow. The structure of the Kelvin waves, as indicated by the in-phase relationship between the zonal wind and geopotential, were found to fade away when reducing the quasi Doppler shifted speed. Further reduction of the Doppler shifted speed was associated with the appearance of structures consistent with the Gill pattern circulation instead of structures consistent with theoretical Kelvin waves. Results are consistent with Kelvin waves being absorbed in Easterly or westerly vertical shear only if the critical layer occurs among the shear layers. Although Vertical wind shear of the zonal wind was found to decelerate the Kelvin waves, the Richardson number varies a lot with the depth of the shear layer, adding more uncertainty to the calculated phase speed of the Kelvin waves.

Part 3 of the dissertation deals with the phase speed of the MJO. In contrast to the deceleration of the convectively coupled equatorial waves with convection, a method of varying regression slope coefficients shows that the MJO accelerates and intensify during high background moisture conditions over East Africa and Indian Ocean. This result suggests that MJO might take on some characteristics consistent with the moisture mode hypotheses (i.e., a moist environment is associated with larger amplitude), yet results also showed that

environments with more moisture also tend to be associated with stronger upper tropospheric easterlies, which would also result in faster eastward movement of the MJO because less westward advection by the background wind would offset the MJO's eastward propagation less.

ACKNOWLEDGMENT

I would like to thank Professor Paul E. Roundy from the bottom of my heart. The milestone that I have achieved is literally because of him. Dr. Roundy provided an opportunity for me to purse PhD program at university at Albany. From the first day, Dr. Roundy encouraged me to investigate the data and to question what I see. The frequent discussions with Dr. Roundy usually end with ideas and information that are challenging to encompass, which motivated me further to deepen my ideas and understanding of the tropical dynamics. By the time my newbie feelings that most scientific problems have been already solved have been eliminated. The whole process was not only about knowledge and experience transfer but ultimately guidance for me to discover my own path of conducting scientific research. Dr. Roundy keeps his office door open, and he used to be patient with my frequent questions, which grew with the expansion of my knowledge circle. Dr. Roundy used to compliment me after each achievement. I was not only fortunate to work under the supervision of a well-known professor in the field of tropical meteorology but also a good-natured person.

I would like to thank Dr. Chris Thorncroft, Dr. Liming Zhou, and Dr. George Kiladis for serving on my Ph.D. committee. Dr. Kiladis's comments on the manuscripts were deep and detailed, and his comments on the posters that I presented during the American Meteorological Society (AMS) meetings were invaluable.

Many thanks to my officemates and classmates for the wonderful discussions that we have. Aside from the scientific discussion, we have a lot of fun talking on languages (Arabic, English, Spanish, and Chines), cultural traditions, memories, many other topics. I would like to extend my sincere thanks to my colleague and buddy Hesham. I know him since I started to work at the Egyptian Meteorological Authority. He was the first person I met once I arrived at Albany, my first roommate until his family arrival. He taught me how to cook, and he helped me get settled at Albany. I would like also to thank the IT and secretary staff for their quick and friendly support. The National Science Foundation (NSF).

No words can express my love and gratitude for my parents, sister, and brother. During our frequent chats, they used to share their happy moments back in Cairo with me. They used to pray to Allah for me to succeed not only in my study but also in my whole life.

When I was young, I used to get excited to wake up to see the new books my father used to buy for us every morning during summer. My brother is taking care of my parents, and without him, I would not be able to come here to study. I would also like to thank my future wife that I did not yet meet, and my unborn kids for waiting for me all that time.

This PhD work was funded by NSF grant number 1560627 awarded to Dr. Paul Roundy.

CONTENTS

LIST OF FIGURES

CHAPTER 1

Introduction

Atmospheric Kelvin waves are a particular type of gravity waves that are trapped around the equator. Kelvin waves were derived mathematically by Matsuno [1966] using shallow water model on beta plane centered around the equator and were then observed in the stratosphere by Wallace and Kousky [1968]. Madden Julian Oscillation [MJO, Zhang, 2005], which is called after their discoverer Madden and Julian, is the key intraseasonal oscillation in the tropics. MJO is a coupling between convection and large-scale atmospheric circulation, resembling approximately a traveling first baroclinic structure with an average speed of 5 m s^{-1}. The structure of the Kelvin wave and MJO ~~is~~ well observed but not yet well understood. A brief look at reviews of Kelvin waves or MJO [e.g., Kiladis et al., 2009b, Zhang, 2005] reveals dozens of mechanisms and theories that explain different aspects of those tropical modes reflecting a rather unsettled and interesting tropical dynamics [Straub and Kiladis, 2003, Straub, 2013].

Dry Kelvin waves are characterized by an in-phase relationship between the zonal wind and geopotential height, with no meridional component of wind [Matsuno, 1966]. The in-phase relationship between the zonal wind and geopotential height relaxes with the moist Kelvin waves [Roundy, 2012]. Moist Kelvin waves are coupled with the convection so that large-scale circulation associated with the Kelvin waves reinforces the convection and vise versa. Different mechanisms have been suggested to understand and quantify the feedback between the convection and circulation, which is at the heart of the tropical dynamics, associated with the moist Kelvin waves [Straub and Kiladis, 2003]. Wave-conditional instability of the second kind (CISK) and stratiform-instability [Mapes, 2000] are suggested to work with the moist Kelvin waves [Straub and Kiladis, 2003].

Moist waves are slower than dry waves because the static stability felt by the moist waves is weaker than that felt by the dry waves [Wheeler and Kiladis, 1999], which is the case with the gravity waves in general. From the normal mode perspective, moist waves are represented by a superposition of low-order baroclinic modes where the speed of the baroclinic

modes is inversely proportional with the order of the baroclinic mode [Gill, 1982, ch6,] and [LeBlond and Mysak, 1981, ch3,]. Stratospheric Kelvin waves are excited by tropospheric convection with preferable phase speeds set by the peak projection mode of the tropospheric convection besides the static stability and background wind state of the stratosphere [Salby and Garcia, 1987, Garcia and Salby, 1987].

Stratospheric Kelvin waves have been interpreted as radiating gravity waves since their first discovery by Wallace and Kousky [1968]. Yet, our understanding of the tropospheric Kelvin waves has ~~been~~ evolved in terms of the traditional normal modes, in which the tropopause is assumed to act as a rigid lid, so the vertical velocity vanishes at the tropopause as on the Earth's surface. Before discovering the stratiform clouds in tropics [Houze, 1997], the vertical structure of the tropical modes was approximated as the first baroclinic mode, which could be tied with the deep convective heating. Later, mapping the stratiform heating with the second baroclinic mode aids in a more accurate representation of the tropical modes; For example, Kiladis et al. [2005] found that the tilted structure of the Kelvin wave and MJO could be simulated using the superposition of the first two baroclinic modes. Given the simplicity of the traditional normal mode paradigm, many tropospheric tropical phenomena have been analyzed and simulated using it like large-scale low-frequency circulations [e.g., Walker circulation Gill, 1980], MJO [Rui and Wang, 1990], equatorial waves [Haertel and Kiladis, 2004]. Yet, the traditional normal mode decomposition was actually built on a rather unrealistic assumption that the transmissivity of the tropopause is zero. Lindzen [2003] and Chumakova et al. [2013] criticize the rigidly of the tropopause given that the static stability in the stratosphere is only two-fold of the static stability in the troposphere. Furthermore, gravity, Kelvin, and equatorial Rossby waves excited in the troposphere are known to propagate through the tropopause.

Stratospheric tropical waves do not propagate forever; rather they deposit their energy and momentum in the mean flow under some conditions. Quasi-biennial oscillation [QBO, Baldwin et al., 2001b] is manifestation of the eddy mean-flow interaction in the stratosphere. QBO is a fluctuation of equatorial zonal-mean zonal wind in the stratosphere with an average period of 28 months. Time-level Hovmoller of the QBO [e.g., Fig 1 Baldwin et al., 2001b] shows perpetual descending and then decaying patterns of the zonal-mean zonal wind. ~~M~~omentum source of the QBO was a matter of debate in the ~~sixties~~s until it has been theo-

retically hypothesized, by Lindzen and Holton [1968], that the QBO is driven by a ceaseless bombardment of equatorial eddies. The deposition of the eddies' energy and momentum were theorized to be achieved via ~~the~~ critical layer interaction dynamics. Nevertheless, the relative contribution of equatorial eddies, e.g., Kelvin, equatorial Rossby, gravity waves, in the momentum budget of the QBO is still an area of active research [Ern and Preusse, 2009b,a, Pahlavan et al., 2021a,b].

Wave plane propagating in layer with a background vertical shear might change their tilt till they become horizontal. In ~~this~~ case, the wave deposits its energy to the background flow, and the phase speed of the wave matches that of the background flow. Most studies have focused on the attenuation of the waves' power or budget~~ing~~ analysis of momentum forcing of waves in bulk associated with QBO phase transitions. However, the structure (e.g., vertical tilt, amplitude) of the stratospheric waves as they are approaching the critical layer when the phase speed of the wave approaches the background zonal wind has not yet been thoroughly analyzed. The horizontal structure of the tropospheric Kelvin waves was found to deviate from the that predicted by the shallow water model under different phase speed (moisture states) [Roundy, 2012]. The structure of the stratospheric Kelvin waves is expected to vary under different background zonal wind and vertical wind shear environments.

MJO is known to accelerate over Eastern Pacific when it decouples from the convection resembling the structure of dry Kelvin waves [e.g., Salby and Hendon, 1994, and many others]. Although the MJO was not predicted by Matsuno's solutions, the MJO structure arose when targeting slow Kelvin waves, suggesting that MJO might share common aspects of ~~the~~ gravity waves dynamics with ~~the~~ Kelvin waves [Roundy, 2014, 2019]. MJO is known to thrive during moist background conditions. For example, advection of the background specific humidity by the intraseasonal flow was found to precede the development of new convective MJO events over the western Indian Ocean [Zhao et al., 2013], and also to align with the moist static energy tendency [Andersen and Kuang, 2012]. It is not clear if the transition from the slow MJO to the fast spontaneous Kelvin waves over the Pacific encompasses MJO transition from slow to fast speed while decoupling from the convection following gravity wave dynamics or the surplus of the background moisture is the essence behind the eastward propagation of the MJO.

1.1 Outlines of the dissertation:

1. Chapter two presents an analysis of the troposphere and stratosphere Kelvin waves. We mentioned in the introduction that the rigidity of the tropopause is questionable; thus, we present a pathway to analyze the tropospheric Kelvin waves as radiating gravity waves rather than a superposition of baroclinic modes. We target kelvin waves using wavelet regression. Also, we use temporal-vertical wavelength analysis to decompose the dependent dataset into an upward and downward component. This study aims to provide a unified paradigm, radiating gravity wave dynamics, through observations to understand the tropospheric and stratospheric Kelvin waves' structure.

2. Chapter three focuses on the stratospheric Kelvin waves structure during different background wind and vertical wind shear states. We shed light on the evolving structure of the Kelvin waves near the critical line, where the energy of the eddies is transferred to the mean flow. We used a special regression technique to target the Kelvin wave at a particular state of the background wind or the vertical wind shear, or both. We also derive a dispersion equation for the Kelvin waves under vertical wind shear. This equation shows the variability of the phase speed of the Kelvin waves under vertical wind shear and shows the vertical wind shear criteria required to induce turbulence while evanescing the Kelvin wave.

3. Chapter four discusses the variability of the MJO phase speed and structure associated with the low-level background moisture states over Eastern Africa, western Indian Ocean, eastern Indian Ocean, and Maritime Continent. The purpose of this analysis, besides understanding the background states modulation of the MJO phase speed, is to understand how the characteristics of the MJO, e.g., phase speed, could resemble that of the gravity wave or moisture mode.

4. Chapter five concludes the main ideas and results found in this Ph.D. work.

5. The appendix discusses the upward-phase and downward-phase wave decomposition technique implemented in chapter two.

CHAPTER 2

Upward and Downward Atmospheric Kelvin Waves across Different Speeds over the Indian Ocean.

2.1 Abstract

Stratospheric Kelvin waves are understood as plane gravity waves, yet tropospheric Kelvin waves have been interpreted as a superposition between the baroclinic modes. The eastward tilt of stratospheric Kelvin wave with height is explained in terms of the Kelvin wave frequency and the Brunt-Väisälä frequency, yet the westward tilt of the tropospheric Kelvin wave is hypothesized as a superposition between the convective (first baroclinic) mode and stratiform (second baroclinic) mode. Fourier filtering is used to decompose the ECMWF Interim reanalysis dynamical fields into upward and downward propagating components. Then, wavelet regression is used to isolate the propagating Kelvin waves over the Indian Ocean across different speeds at zonal wavenumber four.

Results for fast waves show dry upward-phase signal in the troposphere, while downward-phase Kelvin waves occupy most of the stratosphere. The presence of upward-phase tilted waves in the troposphere suggests that the tropospheric Kelvin wave is not a superposition of the upward and downward components, as one might expect in a normal mode. We found that propagating Kelvin waves in the troposphere obey gravity wave dynamics with geopotential height in phase with the zonal wind, the vertical velocity out of phase with the zonal wind, and the temperature in quadrature with the zonal wind. Both dry and moist tropospheric Kelvin waves show a westward vertical tilt, suggesting that tilt probably cannot be a superposition between baroclinic modes coupled to convective and stratiform heating. Under the context of radiating gravity waves, results suggest that faster tropospheric Kelvin waves appear to be associated with higher Brunt-Väisälä frequencies, and waves maintain similar vertical tilt across a wide range of phase speeds.

Keywords — Kelvin wave, equivalent depth, Barotropic, Baroclinic, plane wave, gravity wave, Rigid lid approximation, static stability.

2.2 Introduction

Kelvin waves tilt westward with height in the troposphere [e.g., Wheeler et al., 2000, Yang et al., 2007, Straub and Kiladis, 2003, Roundy, 2012, and many others] and eastward with height in the stratosphere [see Wallace, 1973, and references therein]. The eastward tilt is the only possible configuration for stratospheric Kelvin waves with a tropospheric energy source [Holton and Hakim, 2013, sec 12.5.1]. Although plane gravity wave dynamics explain the eastward tilt of the stratospheric Kelvin wave, superposition between the normal modes (baroclinic modes) has been used to explain the westward tilt in the troposphere. Straub and Kiladis [2003] used the terms "vertical mode" to describe Kelvin wave vertical structure in the troposphere and "vertically propagating wave" to describe vertical structure in the stratosphere. This model of Kelvin waves in the troposphere assumes that a rigid or semi-rigid lid exists at the tropopause. The model for Kelvin wave propagation in the stratosphere assumes that the tropopause is transparent, hence plane waves freely propagate across it. Although it is widely understood that Kelvin wave energy must cross the tropopause to get to the stratosphere, the simple model framework in the troposphere assumes a rigid lid for convenience of obtaining a simple solution there that also meets the boundary condition of zero vertical velocity through the surface of the earth.

Sections 2.2.1 and 2.2.2 summarize the two perspectives.

2.2.1 Normal mode perspective.

Normal modes of a multi-layered shallow water model are called barotropic (external gravity waves) and baroclinic (internal gravity waves). The speed of the barotropic mode is a function in the total depth of flow, while the speed of the baroclinic mode is defined in terms of a virtual depth called the equivalent depth, an analog to the single-layer shallow water model solution characterized by the same phase speed and meridional width (for the derivation see Gill [1982]), a factor used to connect the vertical and the horizontal equations when solving the shallow water model Matsuno [1966] or tidal equations [see Lindzen, 1967]. Taylor [1936] found that a wave in a shallow layer of water matches the phase speed of the atmospheric oscillation if the water has specific depth. Equivalent depth is a term of convenience, allowing us to use solutions for a constant density flow of water as a basis for describing the horizontal structure of wave modes in different media such as the atmosphere.

In most convectively coupled equatorial waves (CCEW) literature, equivalent depth is defined as the depth of the barotropic mode that has the same speed as the baroclinic one, thus higher baroclinic modes are associated with shallower equivalent depths [LeBlond and Mysak, 1981, p126-127]. Observations suggest that slow Kelvin waves are often coupled with convection, while fast Kelvin waves are not [Wheeler and Kiladis, 1999]. In this context, "dry" and "fast", and "moist" and "slow" Kelvin waves are often used interchangeably. This convention is applied even though moisture is not the only factor governing the phase speeds of Kelvin waves (e.g., Doppler shifting by the background flow also impacts phase speed [Dias and Kiladis, 2014]).

Integrating the numerical equations of the oceanic equatorial waves yields both the barotropic mode and baroclinic modes. The barotropic mode is the fastest solution, hence it requires a small time step to satisfy the Courant-Friedrich-Levy criteria of numerical solution stability, hence simulating it is computationally expensive. The rigid lid approximation was first introduced by Bryan [1969] to eliminate the barotropic mode to speed up the integration of the numerical equations of oceanic waves. Although the rigid lid approximation was first used to fix a computational problem for oceanic models, it later became one of the most rooted assumptions in simple models of variability in tropical atmospheric circulation. Large-scale circulations in the tropics are often understood in terms of individual baroclinic modes or superpositions between them. For instance, the basic model for the heat-induced circulation constructed by Gill [1980] explains the Walker circulation in terms of the first baroclinic mode associated with symmetric convective heating around the equator. Later, the discovery of stratiform cloud clusters in the tropics encouraged the tropical community to study the large-scale circulation associated with stratiform heating [Houze, 1997, Schumacher and Houze, 2003]. Mapes [2000] introduced the concept of stratiform instability as a mechanism for wave growth triggered by a reduction of convective inhibition. The stratiform diabatic heating structure resembles a dipole with cooling in the lower layer and heating in the upper layer. This pattern of diabatic heating is often interpreted as the second baroclinic mode. Hartmann et al. [1984] found that a diabatic heating structure centered in the upper troposphere (stratiform heating) leads to a more realistic Walker circulation than deep convective heating. Superposition between the first and the second baroclinic mode has been used to explain the tilted structure of the Madden Julian oscillation [MJO, Kiladis et al., 2005], atmospheric convectively coupled Kelvin waves [Straub and Kiladis, 2003], and 2-day

disturbances [Haertel and Kiladis, 2004, Haertel et al., 2008]. Also, superposition between the first and the second baroclinic modes has been hypothesized to explain the speed reduction of convectively coupled equatorial waves [Straub and Kiladis, 2003, Tulich et al., 2007].

To understand how the superposition between normal modes could simulate the vertical structure of the Kelvin wave, let us project an anomalous vertical structure of zonal wind and heating on the first few normal modes, and assume that the barotropic mode implies a constant horizontal wind with height. In contrast, the first baroclinic mode implies an out of phase relationship between the upper and lower layer wind with a deep region of heating of the same sign extending through the troposphere that achieves its maximum value in the mid troposphere. The second baroclinic mode implies that the wind at the mid levels is out of phase with the wind at the lower and upper boundaries and the heating has opposite sign between the lower and upper troposphere. Higher modes have a similar vertical structure with greater repetition in the vertical. The vertical structure of the observed tropospheric Kelvin wave shows a zonal wind semi-out of phase between the lower and upper layers, suggesting that the vertical structure could be simulated as a first baroclinic mode. However, the vertical structure of the Kelvin wave does not resemble a perfect out of phase relationship between the lower and the upper layers, rather a tilted structure in the vertical [Straub and Kiladis, 2003]. Many authors have suggested that the tilted structure in the vertical could be simulated as a superposition between first and second baroclinic modes held in quadrature by coupling to convection or by other nonlinear processes. Those structures emerge only when the rigid lid boundary condition is applied. Those simple vertical structures models are so popular that the rigid lid assumption that they were based on is often forgotten.

2.2.2 Radiative plane wave

The radiative boundary condition [Durran, 2001] implies that the tropopause is transparent (lid-free) or semi-transparent (leaky lid), thus tropospheric waves can freely or partially propagate to the stratosphere. Lindzen [2003] argued that the "rigid lid" approximation is not supported by the transmissivity of the tropopause. The plane wave view of tropical waves is sometimes used to explain phenomena like the downward propagation of zonal wind associated with the QBO Baldwin et al. [2001b], and fluctuations of tropopause height [Ryu

et al., 2008]. Other phenomena may be understood better assuming a radiative condition at the tropopause, for example Halliday et al. [2018] conducted simulations for tropospheric gravity waves using the radiative condition by raising the upper boundary of the model; they found a decrease in the overall tropospheric response (in vertical wind), which might be more realistic than when the gravity waves are trapped in the troposphere. Chumakova et al. [2013] constructed a hydrostatic, non-rotating model that simulates a leaky, a rigid, and a transparent tropopause. They assumed that if $N1$ and $N2$ are the tropospheric and stratospheric Brunt-Väisälä frequencies, then the tropopause could behave as a rigid lid if $N1/N2 \to 0$, could radiate waves if $N1/N2 \to 1$, and could leak a portion of the waves if the value of $N1/N2$ is between the previous two extreme conditions. They found that almost all normal modes, except the zeroth order baroclinic mode, under the conditions of a leaky or transparent lid, are tilted, in contrast to waves under rigid lid. Under the rigid lid tropopause, superposition between the baroclinic modes is necessary to achieve similarly tilted structures. The structure of the baroclinic modes associated with the leaky or free lid boundary are different from those associated with the rigid lid boundary Chumakova et al. [2013]. Edman and Romps [2017] found that a buoyancy pulse in the troposphere could be dispersed by the gravity wave around the globe in 10 days under the radiative upper air condition without imposing artificial damping that is used with the traditional baroclinic modes under the rigid lid.

Kelvin waves propagating their energy upward do not propagate forever. They could dump their momentum in to the background flow via mechanical or thermal damping or when they encounter a critical layer. The activity of Kelvin waves is often high during the QBO transition from its easterly to its westerly phase Kim and Chun [2015b], Ern and Preusse [2009a], with some exceptions [Das and Pan, 2013]. Near the tropopause, the activity of Kelvin waves sometimes occurs in association with convectively coupled tropospheric Kelvin waves. Yet, the background wind and static stability could modulate the Kelvin wave activity near the tropopause, explaining part of the temporal inconsistency between the activity of the convectively coupled Kelvin waves and Kelvin waves near the tropopause [Flannaghan and Fueglistaler, 2013, Scherllin-Pirscher et al., 2017]

In this paper, we provide new avenues to answer the following two questions: Is the superposition between baroclinic modes the essence behind the tilt of tropospheric Kelvin

waves? Could we understand the tropospheric Kelvin wave as an upward-phase wave? Instead of using two different dynamical frameworks to explain the same wave that probably was emitted by the same source, but crossing through different environments of the troposphere and the stratosphere, we adopt the plane wave view of Kelvin waves. Although plane wave solutions do not meet the surface boundary condition, we diagnose the extent to which such solutions can effectively describe the observed evolution of Kelvin waves above the boundary layer. In section 2.4.5, we shed light on the structure of the upward and downward-phase propagating Kelvin waves. In section 2.4.6, we discuss the characteristics of the upward and downward-phase Kelvin waves at different phase speeds.

2.3 Data

Daily mean zonal and vertical wind, temperature, and geopotential height data were constructed from 6 hour ECMWF interim reanalysis [ERA-I, Dee et al., 2011] data on 2.5° × 2.5° grid, which is sufficient to partially resolve up to wavenumber 72, and well resolves the scales of interest here. In the vertical, the dataset is gridded onto unevenly distributed 32 pressure levels from 1000 hPa to 1 hPa so that a grid point occurs every nearly 0.5 km from 1000 to 500 hPa followed by a grid point roughly every 1 km from 450 to 100 hPa. From 100 to 10 hPa, the vertical resolution decreases further, so that a grid point is found every 2.5 to 5.4 km. All available pressure levels in the stratosphere were used to get the highest possible vertical resolution. Although this dataset has been used to study tropical modes, caution should be exercised when analyzing waves with vertical wavelengths that are twice of the vertical grid resolution Yang et al. [2011a]. The dataset was obtained for the period from 1979 to 2017. We used NOAA outgoing long-wave radiation (OLR) data as a proxy for the deep convection, from 1979 to 2017 on 2.5° × 2.5° grid. Anomalies were estimated by removing the mean and the first four harmonics of the seasonal-cycle based on the period 1980-2010 [Narapusetty et al., 2009b].

2.4 Methods

2.4.1 Wavelet-based predictors

Real-value wavelet filtering is used to generate a base-index for eastward-moving signals at a specific location, wavenumber, and speed to be used later as a predictor in a linear regression model to diagnose the preferred structure associated with the wavelet-filtered signal. As the wavelet kernel is a tapered sinusoid, the pointwise product of wavelet kernel with any function amplifies the points at the center of the function more than those at the edges. Amplification of the points at the center of the function with respect to the points at the edges is called localization, which is the essence behind using the wavelet. In contrast, a base-index created using Fourier filtering is not localized because Fourier transformation is, in its simplest form, a summation of the dot product of sinusoidal harmonics with the targeted dataset (all targeted points are treated in an even way). Although wavelet transforms are often calculated in the frequency or wavenumber or both domains [Torrence and Compo, 1998], we apply them in the time and longitude domain [Roundy, 2017b]. Wavelet filtering in the Fourier domain is faster than in the time-space domain, yet targeting a specific frequency is not achievable. We used a two dimensional (space and time) wavelet following [Roundy, 2017b]:

$$\psi(x,t) = \frac{1}{\sqrt{a\pi}}\frac{1}{\sqrt{b\pi}}\cos(2\pi(f_x x - f_t t))\exp(-\frac{x^2}{b})\exp(-\frac{t^2}{a}) \tag{2.1}$$

Equation (3.1) represents a decaying sinusoidal function with scale factors a in time and b in space that stretch or compress the wavelet kernel. f_x and f_t are the frequencies in both space and time, and their ratio provides the speed of the target signal. We target wavenumber four, which is among the highest power of the Kelvin wave spectrum [Wheeler and Kiladis, 1999, see Fig. 3]. Targeting wavenumber $\lambda_n = 4$ means that $f_x = 4/360$ and $f_t = \left(\frac{\lambda_n}{2\pi Re}\right)\sqrt{gh} \times 60 \times 60 \times 24$, where R_e is the radius of the Earth. The frequency f_t and scaling factor a are related to each other here following $a = 8\left(\frac{2\pi f_t}{2\pi}\right)^{-3/2}$. There is no optimum widely accepted value for a. We optimized so that this relationship ensures that whatever the value of the equivalent depth, we still can get the same number of cycles in the wavelets at each frequency. We set b to 8000 after trial and error experiments, but we keep in mind that wavelet kernel should not be too wide as wavelet kernel must taper to zero in time and space (see Fig.2.1), otherwise localization is not fulfilled, and the wavelet

reduces to some form of the discrete Fourier transform. On the other hand, a wavelet kernel that is too short might detect more noise-scale patterns rather than the large-scale Kelvin waves that we are interested in. Roundy [2017b] added one globe to the east and another to the west of the original globe to allow for a spatial extension of the Kernel so that it could taper to zero. The wavelet is customizable more than the discrete Fourier transform as it is responsive to adjustments of the above parameters, yet some conditions, as we mentioned, must be fulfilled.

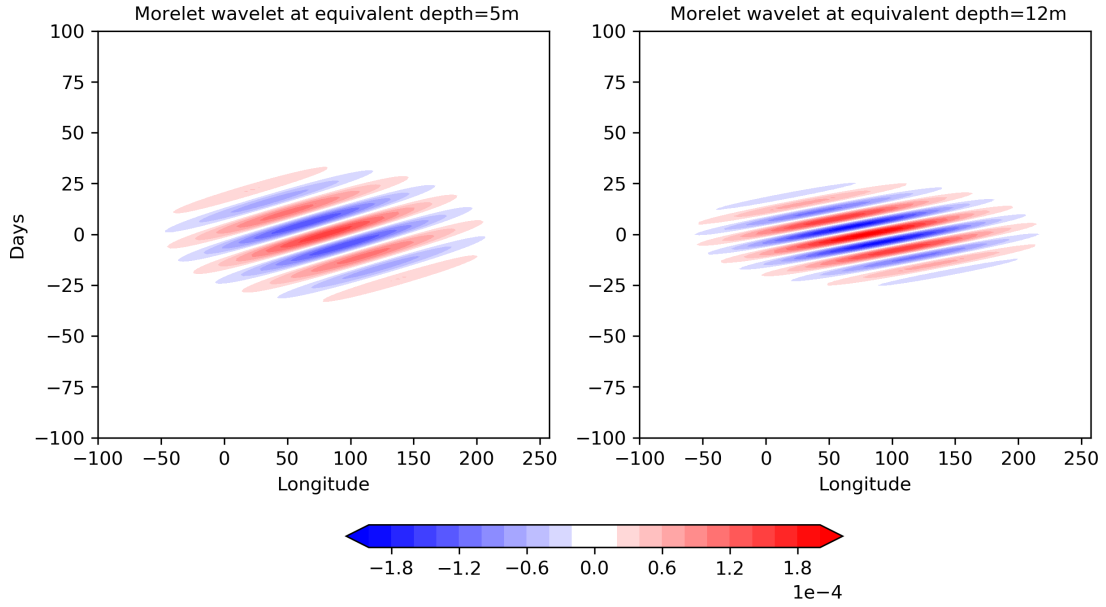

Figure 2.1: Wavelet kernel used to filter a traveling Kelvin wave: equivalent depths of 5 m (left) and 12 m (right)

To create the wavelet kernel, we set the wavenumber λ_n, speed c (or equivalent depth), and the decay parameter in space b. We target zonal wavenumber four [Roundy, 2012], across phase speeds that span from 7 to 29.7 m s^{-1}. We target waves across a set of speeds because there is no specific threshold that could be used to distinguish dry or fast Kelvin waves from those slow or moist waves [Yasunaga and Mapes, 2014], and there is evidence that these waves exist along a continuum [e.g. Roundy, 2012, 2019]. The upper bound of speed is necessary because daily data are not sufficient to provide quality-filtered data at faster speeds (see table 2.1). For example, at equivalent depth 200 m, the speed is 44 m s^{-1} and period is 2.6 days, which is not well resolved on daily data grid. Near those speeds, we plot the wavelet kernel at each frequency to see if the wavy structure is still well represented on the grid. For simplicity, we round the targeted phase speeds in table 2.1 with their nearest

rounding integer.

To create the wavelet indexes that we use for regression analysis, we follow these steps: (1) We used a two-dimensional wavelet kernel that extended globally in space and spans from -100 to 100 days at a given speed. We center the two-dimensional wavelet at the appropriate location and time of the reanalysis data. The wavelet kernel is centered spatially over the equator and 80°E. The base longitude (80°E) was chosen following Roundy [2012], who found a clear and statistically significant Kelvin wave signal at variety of horizontal phase speeds at 80 °E. We also centered the wavelet kernel at the time of interest, but as the temporal dimension of the wavelet kernel extends from -100 to 100 days, then the first day of the reanalysis data that we could target is day 101, and the last day that we can target is 101 days before the end of the dataset. (2) After the wavelet kernel is centered at day 101 of the reanalysis and at 80°E, we calculate the two dimensional average of the point-wise multiplication between the wavelet kernel and dataset; hence the real valued result represents the wavelet index at time 101 of the reanalysis and at 80°E. (3) To get the values of the index at the subsequent times, steps 1 and 2 are repeated after shifting the wavelet kernel one-time step (a day) ahead. (4) We repeat steps 1, 2, and 3 to create new wavelet indexes at different horizontal phase speeds.

Equivalent depth (m)	5	12	20	25	40	60	80	90	100	200
speed (m s^{-1})	7	10.84	14	15.65	19.80	24.25	28	29.7	31.30	44.27
period (days)	16.5	10.6	8.2	7.3	5.8	4.7	4.1	3.9	3.7	2.6

Table 2.1: Equivalent depth (m), horizontal speed (m s^{-1}), and period (days).

2.4.2 Upward and downward data decomposition

We adapted the Wheeler and Kiladis [1999] filtering technique to decompose the dynamical variables into upward and downward components instead of decomposing the anomalies into an eastward and westward components. Most literature on the Kelvin waves uses the "upward" or "downward" terminology to refer to the energy propagation. Yet in this manuscript, we are interested more in the phase direction, because the wavelet upward and downward filtering techniques decompose phase speeds rather than group-velocities. Hence, we use the upward-phase and downward-phase waves to refer to the upward and downward phase direction of the waves, while upward-energy and downward-energy to refer to the en-

ergy propagation of the waves. To accomplish the upward-phase and downward-phase wave decompositions, the discrete Fourier transform is applied in time and vertical level instead of time and longitude. A two-dimensional complex FFT yields four quadrants of positive and negative frequencies and vertical wavenumbers combinations. The inverse Fourier transformation of the positive frequency and vertical wavenumber quadrant and negative frequency and vertical wavenumber quadrant yields the downward components. The inverse transform of the other two quadrants yields the upward component. Maps of the upward and downward Kelvin waves were constructed by the projection of the upward and downward anomalies onto the wavelet-constructed Kelvin index at different speeds. The data are on an uneven vertical grid, but tests show that the algorithm nevertheless separates well upward and downward propagating components across a wide range of scales (see Supplemental material).

2.4.3 Wavelet linear regression and statistical significance test

Linear regression maps of dynamical fields and OLR data were conducted against the wavelet-based indexes. Those dynamical fields are the unfiltered, upward, and downward-filtered data explained in section 4.4.2. Each time series at each grid point or level of the independent variable was regressed against the wavelet index. To track a signal at a given phase speed, for example, 30 m s^{-1}, we regress the dynamical fields against the 30 m s^{-1} wavelet index. These phase speeds refer to the signal in the base index at the base longitude and pressure level. Since the regressions are performed in the time domain, the wavelet index at the base index and pressure level may correlate with signals moving at different speeds at other locations (for example, see Fig. 2.3) or pressure levels, but with a frequency that phases with the index. Targeting Kelvin waves at a specific wavenumber and phase speed reveal wave patterns that are difficult to get when filtering Kelvin waves over a band of wavenumbers and frequencies, as that approach conflates many different structures associated with signals of the different scales included in the filter band.

We constructed the wavelet indexes based on zonal wind at 850 and 70 hPa, and OLR anomalies at 80°E across a list of speeds spanning from 7 m s^{-1} to 30 m s^{-1} (see Table 2.1) or equivalently from 5 m to 90 m equivalent depths at wavenumber four using the wavelet technique explained in section 2.4.1. OLR-based indexes are often used to trace the convectively coupled equatorial waves. However, the presented regression maps are

based on zonal wind at 850 hPa except Fig. 2.6, which is based on zonal wind at 70 hPa. Regression maps based on OLR show similar patterns as those based on zonal wind over the Indian Ocean, but use of the zonal wind allows us to also analyze dry waves. To give the reader some ideas about the difference between OLR data and zonal wind indexes, we show the coefficients of determination (correlations squared R^2) between OLR and zonal wind anomalies and also the wavelet-indexes (Table 2.2). Correlations between the wavelet indexes and variables at the base point imply that wavenumber four Kelvin waves based on the OLR and zonal wind predictors represent 1-5% of the OLR variance and 1-3% of the zonal wind variance. This small amount of variance is a consequence of extraction of the signal associated with a tiny part of the whole wavenumber frequency spectrum. The OLR and zonal wind variances represented by moist Kelvin waves are five and three times those represented by the dry Kelvin waves. The zonal wind wavelet index is negatively correlated with the OLR index, implying that the strongest convection is associated with westerlies at 850 hPa, especially with moist waves. The correlation between the OLR and zonal wind indexes hits its minimum for the fastest (driest) waves, which indicates that zonal wind indexes tend to target non-moist waves at fast speeds.

Speed (m s^{-1})	30	28	24	20	16	14	11	7
R^2(OLR index , OLR anom)	0.01	0.01	0.02	0.02	0.03	0.03	0.04	0.05
R^2(U850 index , U850 anom)	0.01	0.01	0.01	0.01	0.02	0.02	0.02	0.03
R (OLR index , U850 index)	-0.27	-0.35	-0.5	-0.57	-0.54	-0.51	-0.47	-0.5

Table 2.2: Correlations squared (R^2) between OLR and 850 hPa zonal wind indexes and total unfiltered anomalies (first and second rows). Correlations (R) between OLR and 850 hPa zonal wind indexes at 80°E (third row). All correlations are statistically significant above the 90% confidence level.

As both of the dependent and independent variables of the linear regressions were filtered using Fourier or wavelet transforms, we used a non-parametric hypothesis test to test if the slopes are statistically different from zero following Roundy [2014]. Hence the null hypothesis is that the slopes are zero. A bootstrap test [see Ch. 5 of Wilks, 2011] was implemented by generating 10,000 predictors that have the same spectral power as the original predictor but random phases [Roundy, 2019]. Then each predictor was used to in place of the original predictor in the regression models. Hence, for a given grid point in a field of predictands, we get 10,000 slopes that constitute the null distribution. Not surprisingly, the mean of the null distribution is zero. Hence the regressed field is statistically significant

above the two-tailed 95% level if it lies before the 250th or after the 9750th ranked slope.

2.4.4 Horizontal structure of the Kelvin waves.

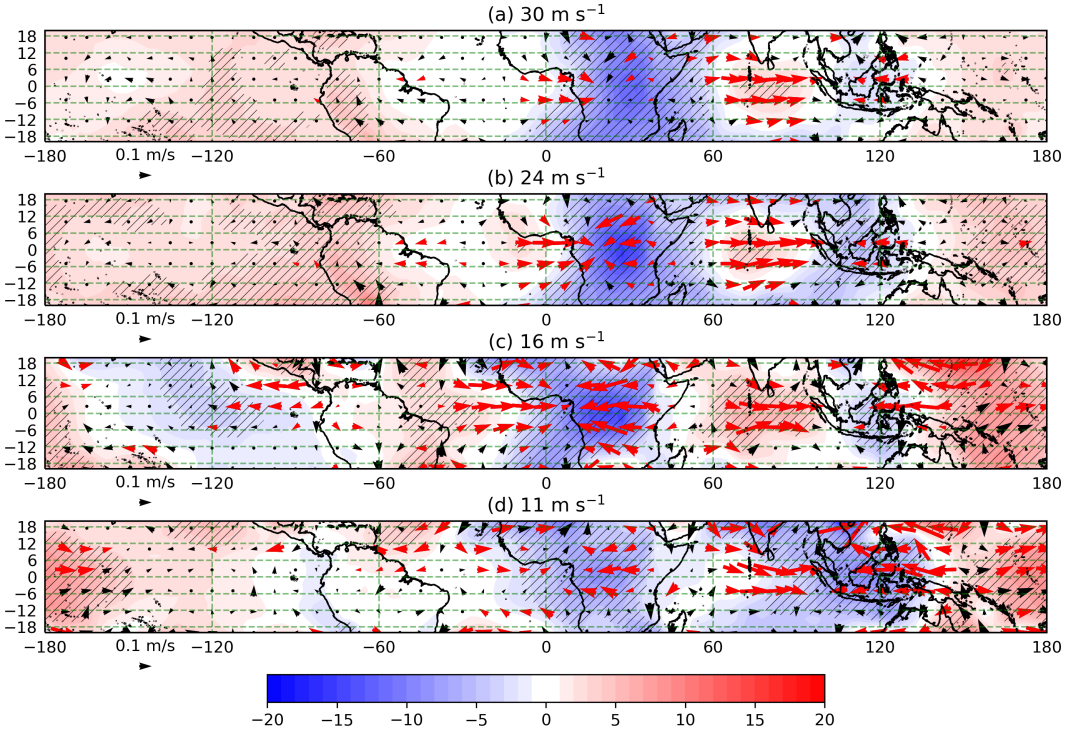

Figure 2.2: Regressed 850 hPa geopotential (shaded at interval of 1 m^2 s^{-2}) and wind (represented by the vectors where key wind represents 0.1 m s^{-1}) against wavelet index based on zonal wind at 850 hPa, filtered at 30, 24, 16, and 11 m s^{-1} at 80°E. Hatches and red vectors indicate that the geopotential and zonal wind are statically significantly different from zero above the 90% level using student's t-test.

The Horizontal structures of the regressed wave against U850 base index are depicted in Fig. 2.2. At 30 m s^{-1} as shown in Fig. 2.2a, westerlies collocate with a ridge over the Indian ocean, and easterlies collocate with a trough over Maritime-continent. The trough over Africa, however significant, is not collocated with strong easterlies. The pattern at 28 m s^{-1} (not shown) is similar to that 30 m s^{-1}. At 24 m s^{-1} which is displayed in Fig. 2.2b, easterlies develop over Africa, and a small ridge develops immediately west of Africa, hence forming strong convergence over western Africa. This ridge-trough couplet center is located to the west when targeting slower speed Kelvin as shown in Fig. 2.2c-d. At 16 m s^{-1} as presented at Fig. 2.2c, the ridge over the Indian Ocean reaches its maximum intensity. Easterlies appear over the eastern portion of the Maritime-Continent in association with the

equator-ward side of an extra-tropical ridge. At 11 m s^{-1} as demonstrated in Fig. 2.2d, the in phase relationship between the zonal wind and height relaxes (westerlies shift eastward with respect to the ridge anomalies). Fast Kelvin wave structure agrees with the structure of the dry Kelvin wave as described by Matsuno [1966]. However, at slower speeds, a relaxation in the in-phase relationship between the zonal wind and the geopotential becomes more evident. The deviation from the theory of the dry kelvin wave apparently arises because convection creates its own dynamical field in a way that does not phase completely with the dry Kelvin wave structure. A similar pattern occurs in the MJO, but also in slow eastward-moving signals at wavenumber four highlighted by Roundy [2012]. Since these signals are broadly consistent with Kelvin waves, throughout the rest of the paper, structures are referred to as Kelvin waves.

The interaction of the propagating Kelvin waves at different speeds with the convection is analyzed using lagged regression of zonal wind and OLR anomalies (Fig. 2.3). As anticipated, Kelvin waves decelerate with intensification of the the convection (see Fig. 2.3a-d). The 30 m s^{-1} Kelvin wave suddenly accelerates once it leaves East Africa with abrupt weakening of the convection (Fig. 2.3a). Similar Kelvin waves decoupling from convection proximate to the Western Indian ocean are also observed associated with 24 m s^{-1} Kelvin waves (Fig. 2.3b). The discontinuities around Africa might result from land-sea contrast or interaction of Kelvin wave winds and convection with topography.

2.4.5 Upward and downward Kelvin waves

To get more insight into the vertical structure of the Kelvin wave, we present the upward-phase and downward-phase components of the Kelvin waves. To show that, the zonal wind, geopotential, vertical wind, and temperature prefiltered for upward-phase and downward-phase moving signals were regressed against the wavelet bases during northern spring (March-May), the peak season of the Kelvin wave [Roundy and Frank, 2004]. Besides that, we present maps of the regressed unfiltered (neither decomposed into upward-phase nor downward-phase components) aforementioned dynamical fields. Figure 2.4 shows the regressed unfiltered (first column), downward-phase filtered (second column), and upward-phase filtered (third column) data averaged between 10°S and 10°N associated with the wavelet-filtered zonal wind at different phase-speeds. By comparing Fig. 2.4a with Figs.

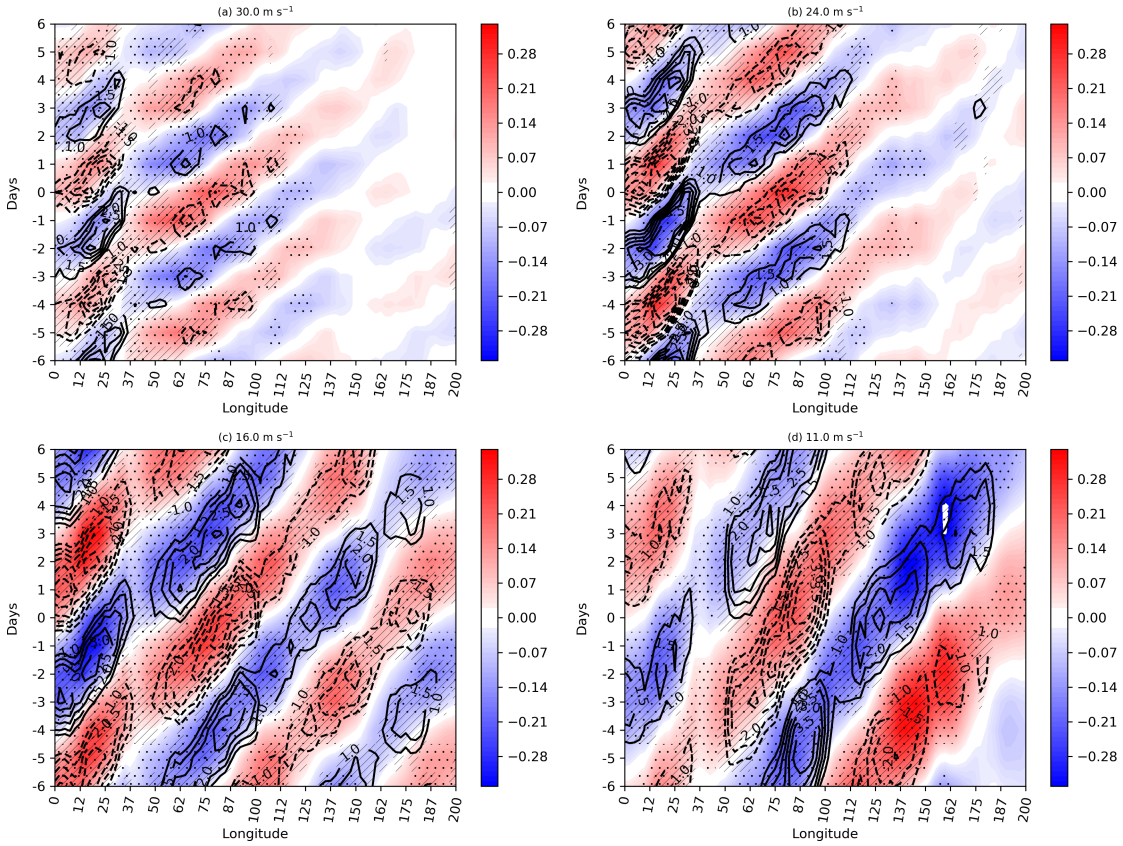

Figure 2.3: Lagged regression of the zonal wind anomalies at 850 hPa (shaded at intervals of 0.01 m s^{-1}) and the OLR anomalies (contoured at interval of 0.5 W m^{-2}) based on the zonal wind index at (a) 30 m s^{-1}, (b) 24 m s^{-1}, (c) 16 m s^{-1}, (d) 11 m s^{-1}. Dots and hatches indicate that the zonal wind and OLR are statistically significant different from zero above the 90% level using student's t-test.

2.4d, g, we find that the downward-phase component of the Kelvin wave (Fig. 2.4d) is the stratospheric part of the unfiltered Kevin wave (Fig. 2.4a), which was discovered by Wallace and Kousky [1968] using radiosonde data, and the upward-phase component of the Kelvin wave (Fig. 2.4g) is the tropospheric part of the unfiltered Kelvin wave (Fig. 2.4a). The tropospheric component is often described in term of the superposition of the baroclinic modes [Straub and Kiladis, 2003, and many others]. The downward-phase and upward-phase components of the waves correspond to upward and downward group velocities, which are not diagnosed here because of the need to include multiple neighboring wavenumbers to reveal clear group propagation. The context of the upward-group and downward-group waves could be understood by imagining a wave source, somewhere in the upper middle troposphere, that radiates energy upward and downward away from the wave source, and we

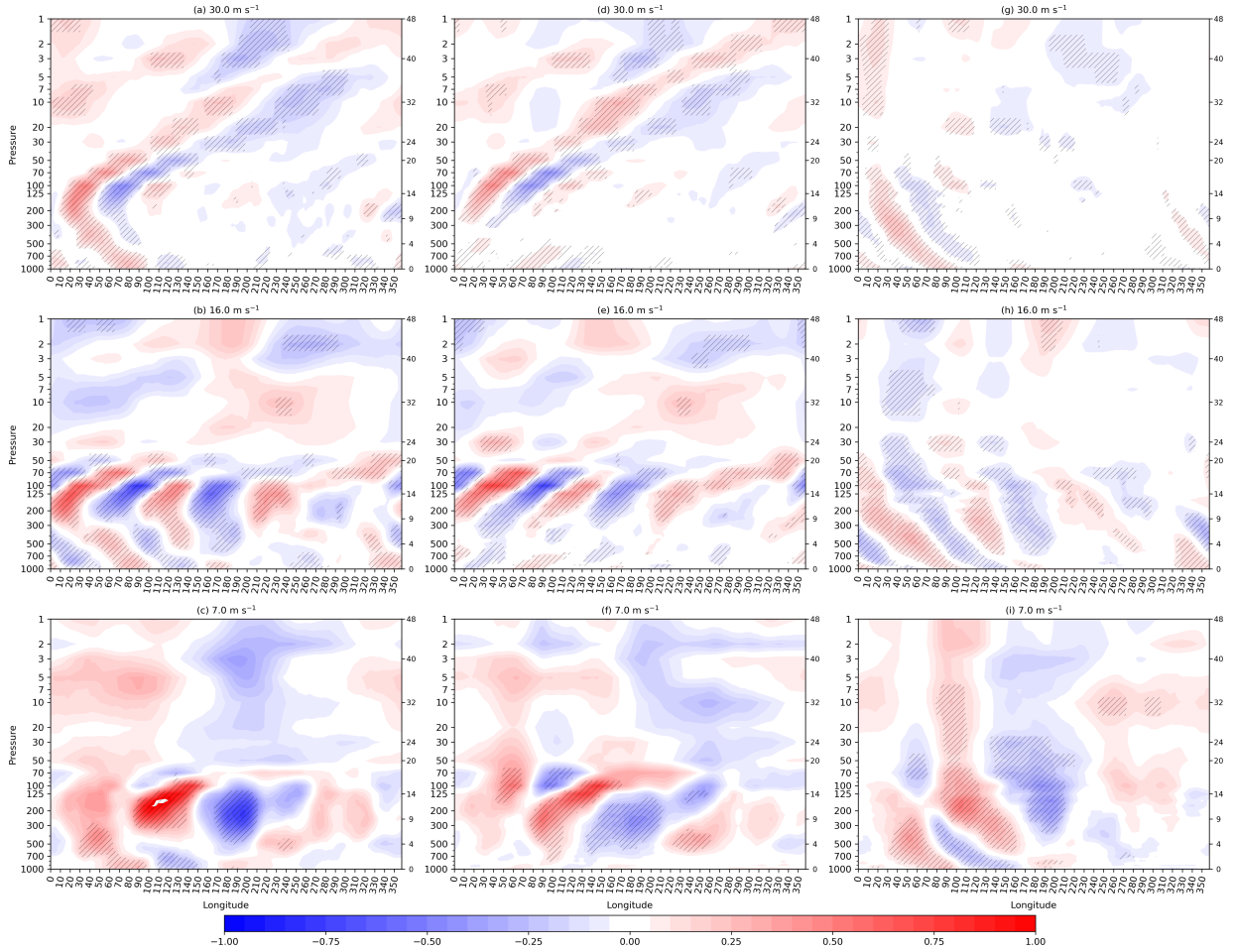

Figure 2.4: Regressed unfiltered zonal wind anomalies (first column), downward-phase filtered zonal wind anomalies (second column), upward-phase filtered zonal wind anomalies (third column) averaged between 10°S and 10°N on the wavelet-filtered kelvin wave predictors based on the zonal wind at 850 hPa at 30 m s^{-1} (a,d,g), 16 m s^{-1} (b,e,h), 7 m s^{-1} (c,f,i). Zonal wind are shaded in interval of 0.05 m s^{-1}. The hatches refers to location that are statistically significant above the 90% level using the bootstrap technique mentioned in section 4.4.2.

know from the gravity wave dynamics that the phase velocity and the group velocity must be perpendicular in the vertical. Thus, the upward-energy component of the Kelvin wave must radiate energy and momentum upward, and the downward-energy component of the Kelvin wave must radiate energy and momentum downward. Although the following analyses were performed based on zonal wavenumber four, the wavelet filtered Kelvin wave represents a wave-packet centered at wavenumber four rather than a single wave.

At 30 m s^{-1}, the unfiltered Kelvin wave amplitude peaks at the elbow joint, between 200 and 125 hPa (Fig. 2.4a). Although different reanalysis data sets show different vertical

structures and peaks of the climatological diabatic heating, most reanalysis data show upper peaks between 300 and 400 hPa or between 400 and 500 hPa [Ling and Zhang, 2013]. The location of the elbow joint of the regressed zonal wind associated with the 30 m s^{-1} index is higher than the location of the climatological diabatic heating. The downward-phase component of the Kelvin wave extends horizontally almost around the globe, and vertically from below 200 hPa (if most of the elbow joint is considered a part of the unfiltered wave) to 1 hPa (Fig. 2.4a) or from 300 to 1 hPa based on the upward component (Fig. 2.4d). On the other hand, the upward-phase Kelvin wave (Fig. 2.4g) extends from the surface of the earth to around 70 hPa as shown in the upward-phase component (Fig. 2.4g) or below 200 hPa (if the elbow joint is not considered a part of the unfiltered wave) (Fig. 2.4a). The upward-phase component of the Kelvin wave as depicted in Fig. 2.4g shows a vertical plane wave above 70 hPa, which indicates that Kelvin wave oscillates with the maximum allowed frequency, which is the Brunt-Väisälä angular frequency, if there is no diabatic forcing or large thermal or mechanical sink.

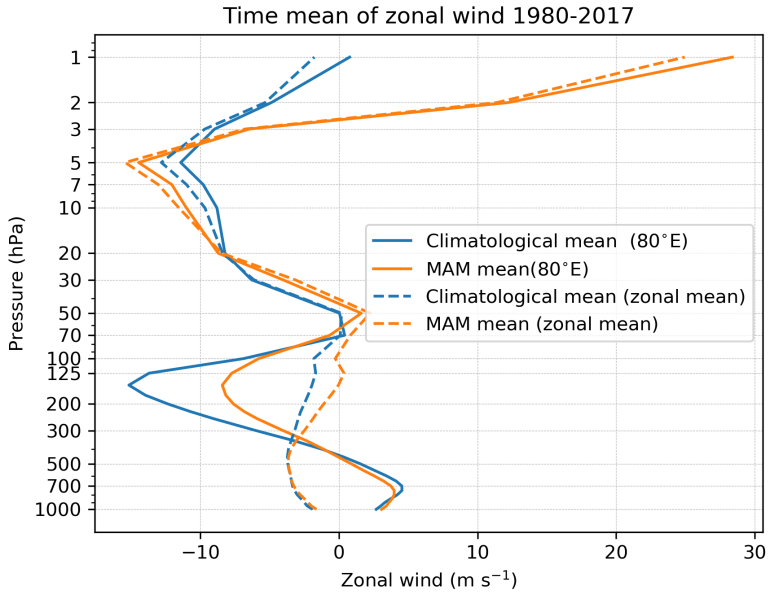

Figure 2.5: Climatological mean based on 1980-2017 of zonal wind at 80°E (solid blue) and zonal-mean zonal wind (dashed blue), and MAM mean based on the same period at 80°E (dashed orange) and zonal-mean zonal wind (solid orange).

At 16 m s^{-1}, the Kelvin wave does not extend as far into the stratosphere (Figs. 2.4b,e) compared to the 30 m s^{-1} Kelvin wave (Figs. 2.4a,d). Additionally, the 16 m s^{-1}

downward-phase Kelvin wave seems to straddle around about 50 to 70 hPa in the unfiltered Kelvin wave (Fig. 2.4b). Figure 2.4b shows that, at 50 hPa, the tilt of the phase-lines decreases strongly till it resembles a horizontal plane wave. The upward-phase component of the regressed Kelvin wave decays suddenly around 70 hPa (Fig. 2.4e). The sudden horizontal change of the plane wave tilt (Fig. 2.4b) might occur if Kelvin waves face strong wind shear by the background wind [Wallace, 1973, see section 4]. The abrupt decay of the of the wave amplitude (Fig. 2.4e) suggests that Kelvin waves dump their energy to the mean flow Andrews et al. [1987] by either: (1) losing its energy via mechanical or thermal damping factors, (2) approaching the critical layer where the speed of the Kelvin wave matches that of the mean flow [Bretherton, 1966, Booker and Bretherton, 1967]. The existence of the critical layer or background wind shear could be verified by examining the vertical distribution of the time-mean zonal wind depicted in Fig.2.5. The 30, 16, and 7 m s^{-1} wavenumber four Kelvin waves are faster than the background zonal wind at the upper troposphere and lower stratosphere (Fig. 2.5), thus wavenumber four Kelvin waves at the aforementioned phase-speeds may not deposit their energy into the mean flow via the critical layer interaction (method (2) above) under the assumption that those Kelvin waves maintain their high speeds relative to the background flow. On the other hand, westerly wind shear is clearly present from 150 hPa to 70 hPa, which might decrease the tilt of the Kelvin wave as shown in (Figs. 2.4b,e). However, it is not clear why the 30 m s^{-1} Kelvin wave seems not to be disrupted by such background wind shear. Figure 2.4h depicts the upward-phase component of the vertical Kelvin wave which extends farther to east covering most of the eastern hemisphere. The weakening of the upward-phase component between 500 and 300 hPa in the regression map of the unfiltered data (Fig. 2.4b) is a result of the passage of the downward-phase Kelvin wave.

For the 7 m s^{-1} base index, the wavy structure, previously seen associated with the dry Kelvin wave weakens (Figs. 2.4c,f,i), suggesting the rising role of the moist dynamics. At this phase speed, the frequency is so low that no Kelvin wave can occur in the stratosphere, given its stratification, lack of moisture, and its background flow. At 160°E, deep convergence extends from around 700 hPa to the tropopause overlays a shallow layer of divergence and capped with a shallow divergence layer around 70 hPa. The downward-phase component shown in Fig. 2.4f depicts a strongly trapped wave as the wave planes tilt horizontally. In contrast to the Kelvin wave at higher speeds, both the downward (Fig. 2.4f) and upward-

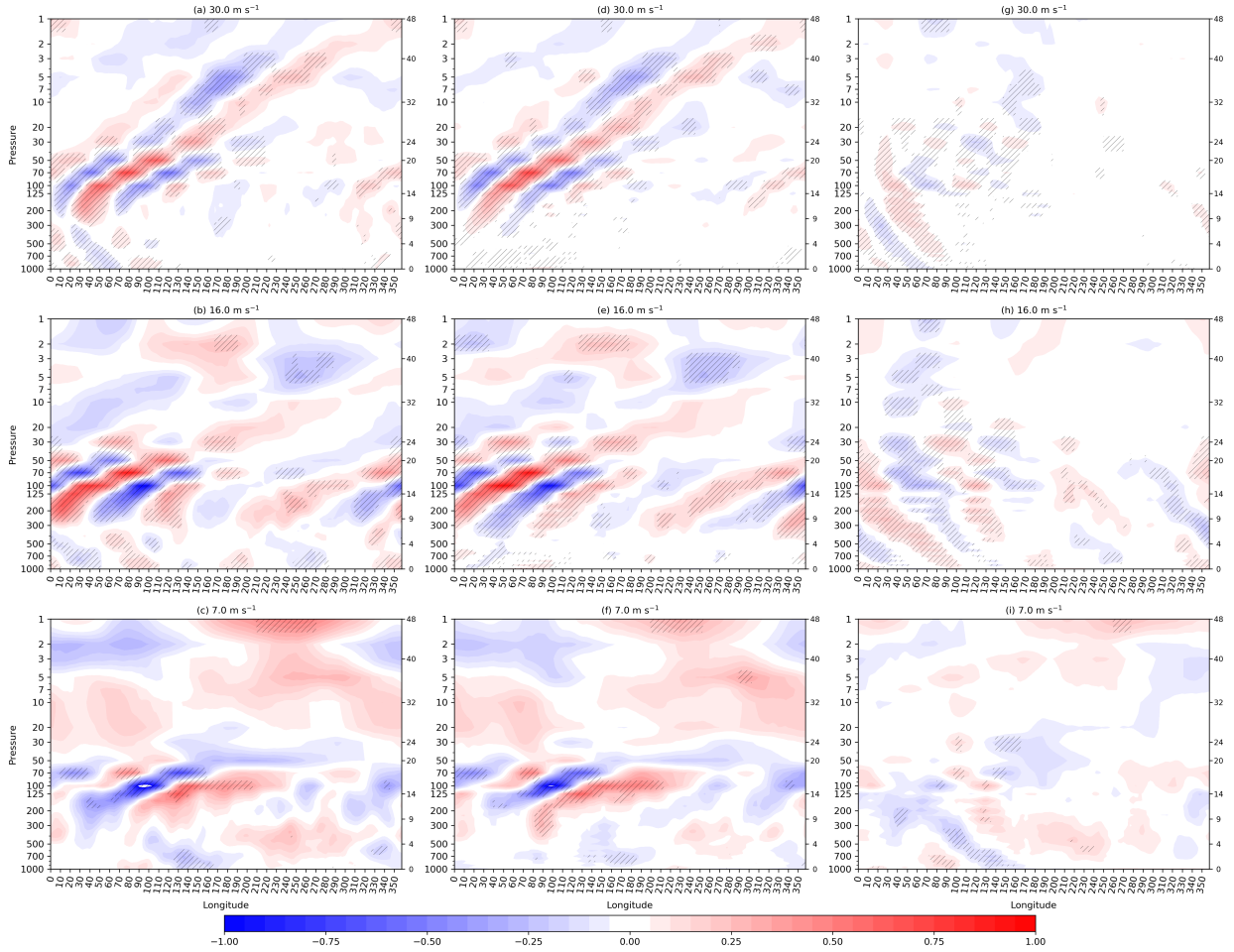

Figure 2.6: The same as Fig.2.4 except that the predictor is based on zonal wind at 70 hPa.

phase (Fig. 2.4i) components seem to contribute to the equatorial circulations found in the troposphere (including the overturning circulation associated with convection). The height of the elbow joint decreases with decreasing the phase-speeds. At 30 m s^{-1}, the elbow joint is centered above 200 hPa, and it relocates at about 200 hPa at 16 m s^{-1}.

The regressions in Fig. 2.4 were reproduced but against wavelet filtered zonal wind at 70 hPa (Fig. 2.6) instead of at 850 hPa. The general structure of the regressed Kelvin wave based on zonal wind at 70 hPa matches that at 850 hPa, reflecting the robustness of the Kelvin wave signal. The downward-phase Kelvin wave regressed against zonal wind at 70 hPa is stronger than that based on the 850 hPa zonal wind. For example, in the slowest filtered wave (Figs. 2.6c,f), the regressed downward-phase signal seems to replace the overturning circulation in (Figs. 2.4c,f). On the other hand, the upward-phase component associated

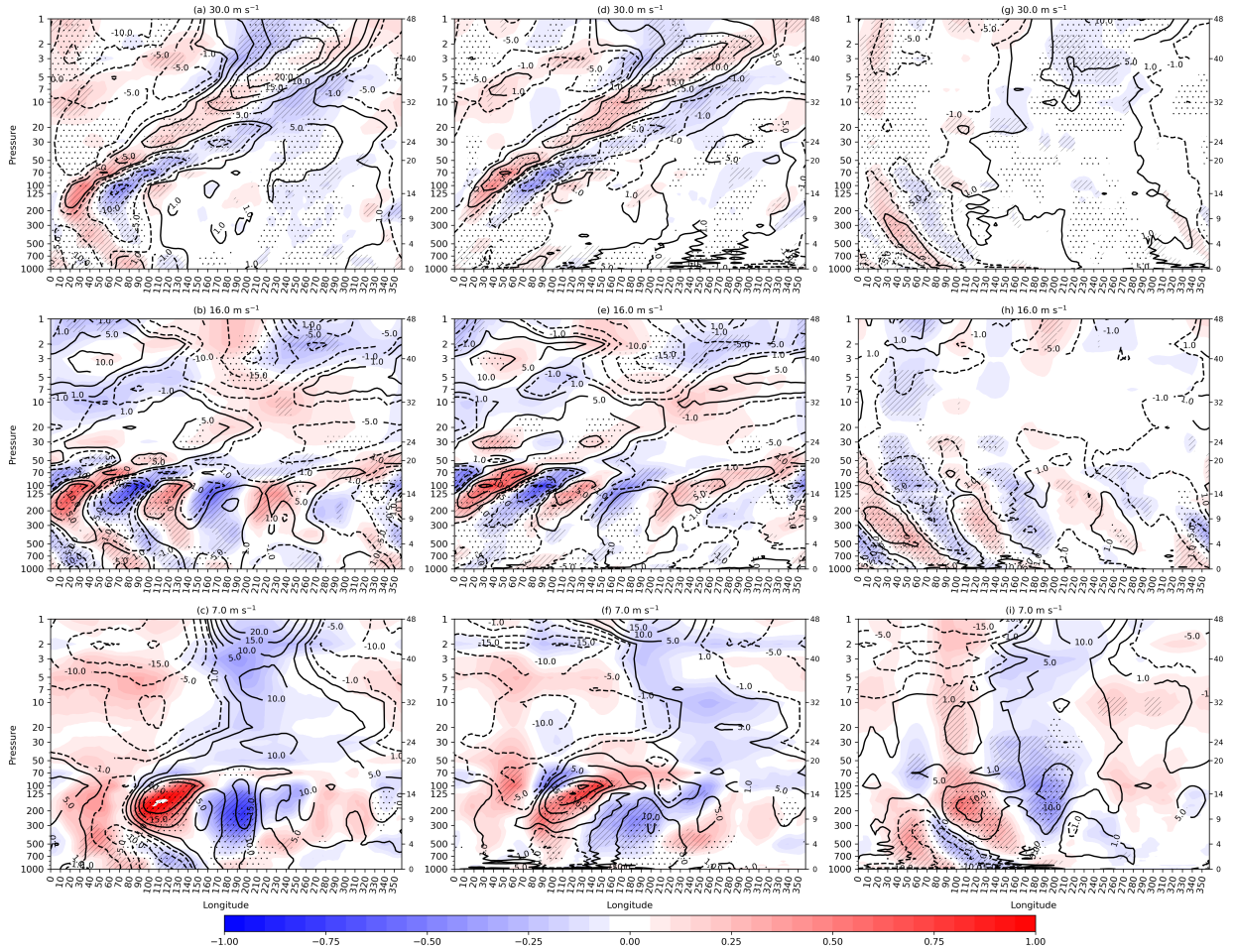

Figure 2.7: The same as Fig.2.4 but with overlaying geopotential contours at interval of 5 m^2 s^{-2}. The hatches and dots refers to location of zonal wind and height that are statistically significant above the 90% level using the bootstrap technique mentioned in section 4.4.2.

with the zonal wind at 70 hPa (Fig. 2.6g,h,i) looks weaker in amplitude than those associated with zonal wind at 850 hPa (Figs. 2.4g,h,i).

Figure 2.7 depicts the regressed geopotential anomaly overlaid on the regressed zonal wind. The regressed zonal wind pattern is in phase with the regressed geopotential (Figs. 2.7a,b,d,e,g,h). Although the in-phase relationship prevails in the regressed zonal wind and geopotential, an out-of-phase pattern between the zonal wind and geopotential appears on the upper left side of the stratospheric regression map (Fig. 2.7a), and above 50 hPa at the slowest wave (Fig. 2.7c), where westerlies collocate with troughs and easterlies collocate with ridges. This pattern is consistent with the phase relationship anticipated on the equatorward side of gyres in Rossby waves. The appearance of the Rossby wave-like pattern is not

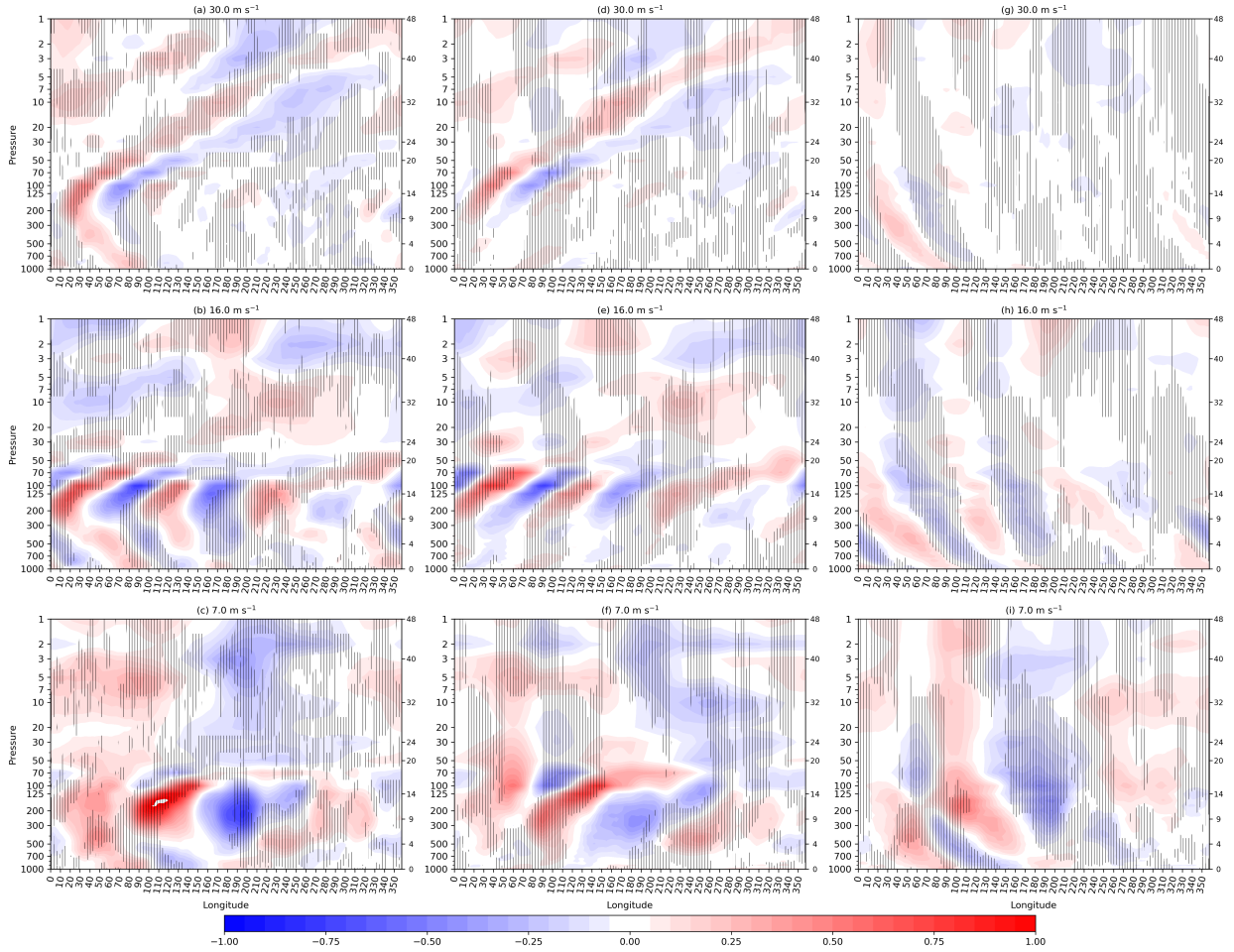

Figure 2.8: The same as Fig.2.4, yet with vertical wind included as vertical dashes for positive values while unshaded regions indicate a downward motion.

surprising as it is consistent with previous analysis, such as Roundy [2019], who showed that slow Kelvin wave like features over the warm pool region are correlated with extratropical Rossby waves approaching the equator over the Western Hemisphere [Sakaeda and Roundy, 2015]. Although the wavelet kernel is a two-dimensional array that targets only eastward traveling waves at certain wavenumber and speed, the index used in the regression is only a function in time, a result of the average of the dot product between the wavelet kernel and the anomalies at each time step. Thus, any structure with a temporal scale that matches that of the predictor with a sufficiently consistent phase in time will appear in the regression maps. At 7 m s^{-1}, Fig. 2.7c shows that, to the west of 150°E, westerlies collocate with ridges implying a Kelvin wave-like structure, yet to the east of the 150°E easterlies collocate with ridges that might be associated with Rossby waves approaching the equator.

To get a comprehensive view on the vertical structure of the regressed waves, we show the vertical structure of both the vertical wind and the temperature. The vertical motion of both the downward-phase and upward-phase Kelvin waves is depicted in Fig. 2.8 where vertical dashes refer to upward motions. Figures 2.8a,b,c shows that, in the stratosphere, upward or downward motion correlates with westerlies or easterlies. However, in the troposphere, the opposite occurs where upward or downward motion correlates with easterlies or westerlies. The in-phase relationship between the vertical velocity and zonal wind in the stratosphere maintains the upward-flux of momentum, and the out-of-phase relationship in the troposphere is important to direct the momentum out from the wave source to the lower layers Andrews et al. [1987]. At 16 m s^{-1}, the same relationship holds for the Kelvin waves between 1000 and 70 hPa, as shown in Figs. 2.8b,e,h. At 7 m s^{-1}, Fig. 2.8c shows an overturning circulation with ascending motion centered at 90°E and descending motion centered at 140°E. Large part of the downward-phase component (Fig. 2.8f) of the slowest wave is confined in the troposphere rather than the stratosphere, and the in-phase relationship between the zonal and vertical wind still holds. Figure 2.9 shows the regressed temperature and zonal wind. The temperature in the stratosphere is in quadrature with the zonal wind following thermal wind balance [Wallace and Kousky, 1968], the maximum zonal wind lies to the east of the minimum temperature and to the west of the maximum temperature as in Figs. 2.9a,b,d,e. The same quadrature relationship between the temperature and the zonal wind holds in the troposphere (Figs. 2.9a,b,g,h). However, the upward component of the 7 m s^{-1} Kelvin wave shows an in-phase relationship between the zonal wind and temperature (Fig. 2.9f), and the downward component does not show a clear quadrature relationship (Fig. 2.9i).

2.4.6 Characteristics of the Downward-phase and Upward-phase Wave Components among Different Phase Speeds.

Wave characteristics are deduced from the dispersion equations. The dispersion equation of the downward-phase Kelvin waves is well documented [see Andrews et al., 1987], yet the vertical component of the upward-phase component (suggested in this paper) is not since the vertical structures of the tropospheric Kelvin waves are often explained in terms of the normal modes. For a comprehensive view of the downward-phase and upward-phase wave components, Table 2.3 lists the Boussinesq Doppler-shifted (or more accurately quasi

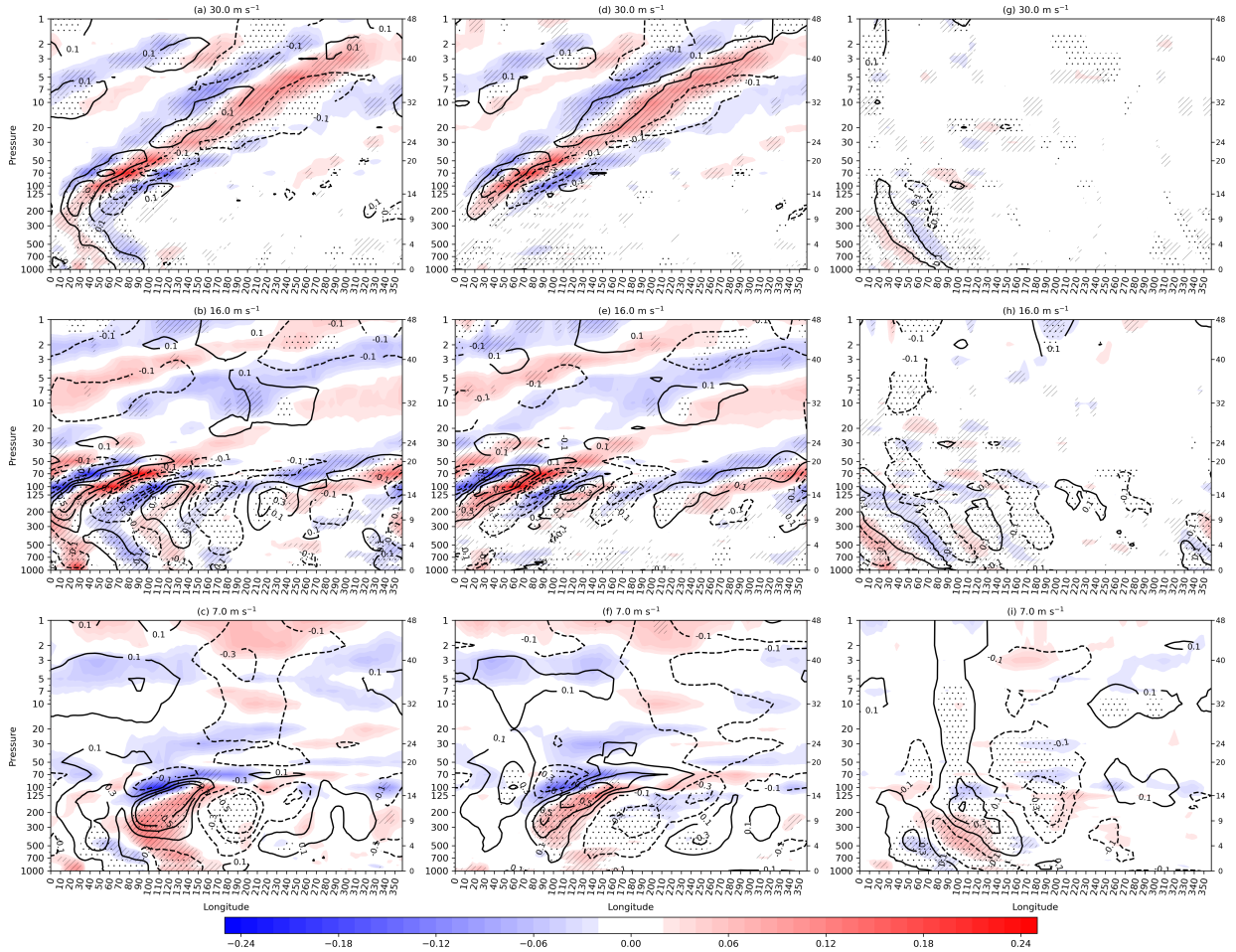

Figure 2.9: The same as in Fig. 2.4 with shading represents the temperature contoured at interval of 0.1 K and the contours represent zonal wind at interval of 0.1 m s^{-1}. Dotes and hatches indicate that the zonal wind and temperature are statistically significantly different from zero above the 90% level using the bootstrap technique mentioned in section 4.4.2.

Doppler-shifted as introduced by Gerkema et al. 2013) horizontal and vertical phase and group velocities for the the downward-phase and upward-phase Kelvin waves. The quasi Doppler-shifted horizontal phase c_x^* and group c_{gx}^* velocities for both the downward-phase and upward-phase waves are directed in the same (positive) direction, hence directed eastward (see Table 2.3). On the other hand, the quasi Doppler-shifted vertical phase c_z^* and group c_{gz}^* velocities are oppositely directed to each other (see Table 2.3). Hence, downward-phase waves transport momentum upward and upward-phase waves transport momentum downward.

As the horizontal phase speed of the theoretical Kelvin wave is not a function in the

horizontal wavenumber, Kelvin waves are not dispersive in the horizontal ($c_x^* = c_{gx}^*$). On the other hand, Kelvin waves are known to be dispersive in the vertical ($c_z^* = -c_{gz}^*$), since vertical phase speed of the Kelvin wave is a function of the horizontal wavenumber. Waves that have shorter horizontal wavelengths move faster in the vertical than waves with the longer zonal wavelengths.

The listed dispersion equations (see Table 2.3) account for the background wind (quasi Doppler shifted), but they do not account for the vertical wind shear. The background zonal wind $\overline{u}$, vertical wavenumber m, and the Brunt-Väisälä angular frequency N used to derive the listed dispersion equations are in essence constants. However, those parameters could vary slowly with height if their values at specific height are much larger than their derivative with height when evaluating the vertical derivative of the wave solution $e^{(kx+mz-\omega t)}$ [Andrews et al., 1987].

Downward-phase waves ($m < 0$)	Upward-phase waves ($m > 0$)
$\omega^* = \omega - k\overline{u} = -\dfrac{Nk}{m}$	$\omega^* = \omega - k\overline{u} = \dfrac{Nk}{m}$
$c_x^* = c_x - \overline{u} = -\dfrac{N}{m}$	$c_x^* = c_x - \overline{u} = \dfrac{N}{m}$
$c_z^* = \dfrac{\omega}{m} - \dfrac{k}{m}\overline{u} = -\dfrac{Nk}{m^2}$	$c_z^* = \dfrac{\omega}{m} - \dfrac{k}{m}\overline{u} = \dfrac{Nk}{m^2}$
$c_{gx}^* = \dfrac{\partial(\omega - k\overline{u})}{\partial k} = -\dfrac{N}{m} = c_x^*$	$c_{gx}^* = \dfrac{\partial(\omega - k\overline{u})}{\partial k} = \dfrac{N}{m} = c_x^*$
$c_{gz}^* = \dfrac{\partial\omega}{\partial m} = \dfrac{Nk}{m^2} = \dfrac{(\omega - k\overline{u})^2}{Nk}$	$c_{gz}^* = \dfrac{\partial\omega}{\partial m} = -\dfrac{Nk}{m^2} = -\dfrac{(\omega - k\overline{u})^2}{Nk}$

Table 2.3: Quasi-Doppler shifted angular frequency ω^*, horizontal c_x^* and vertical c_z^* phase velocities, and horizontal c_{gx}^* and vertical c_{gz}^* group velocities of the downward-phase and upward-phase waves. The superscript $*$ refers to doppler shifted component. k and m are the horizontal and vertical wave numbers.

To compare the targeted wave speeds (listed in Table 2.1) with the phase speed of the observed patterns, lagged regression maps are created at different pressure levels (Figs. 2.10). Both the observed speeds (found from the regression maps) and targeted speeds (listed in Table 2.1) of the Kelvin waves represent the wave speeds relative to the ground. Figures 2.10 displays lagged-longitude maps of the 850 hPa based 30 and 16 m s^{-1} Kelvin waves at different pressure levels. The first thing to notice in Fig. 2.10 is the prevalence of an eastward propagating Kelvin waves in the Eastern Hemisphere. To get an idea on the change of the phase speed of the Kelvin wave with pressure levels, we draw reference lines for the phase speed (Figs. 2.10). The reference lines are drawn to match the bulk of the

contoured anomalies. Nevertheless, subjective methods are known to prone to human errors. Uncertainties could also appear based on our own interpretation of the signals when there are discontinuances or acute changes of the phase speed. Those uncertainties are inevitable and they exist in both subjective and objective methods. To get an idea on this type of uncertainty, we show two reference lines for the 30 m s^{-1} wave at 850 hPa. The 23.6 m s^{-1} reference line excludes the signal between 40° and 60°E, which is faster than those over the Indian Ocean, yet we get the 28.6 m s^{-1} reference line when accounting for the signal between 40° and 60°E, which is closer to the targeted signal. The reference line of the 16 m s^{-1} Kelvin wave at 850 hPa (the base level) shows propagation with 18 m s^{-1}, which is 2 m s^{-1} faster than the targeted phase speed. The 30 m s $^{-1}$ Kelvin wave at 850 hPa achieves a minimum speed of 17 m s $^{-1}$ at 500 hPa possibly due to dissipation Garcia and Salby [1987], and maximum speed of 28.9 m s $^{-1}$ at 50 hPa. The same behavior also is found when targeting the 16 m s $^{-1}$ (7 day) Kelvin wave at 850 hPa. A minimum speed of 12.8 m s $^{-1}$ is evident at 500 hPa, and maximum speed of 20 m s $^{-1}$ is observed at 50 hPa. Above 50 hPa, the Kelvin wave velocities increase substantially (not shown). Although we set the wavenumber and frequency (hence zonal phase speed) of the wavelet index, linear regression captures only the patterns with the same frequency of the index. Hence, the mismatch between the 30 m s^{-1} targeted Kelvin wave and the observed patterns at other levels indicates that, at the 4 day period, more power is confined at different speed signal (with different wavenumber) rather than the 30 m s^{-1} Kelvin wave. The structure of the Kelvin wave at various background zonal wind speeds is analyzed thoroughly in a separate study.

Vertical wavelengths of the Kelvin waves could be obtained using the time-height maps (Fig. 2.11) of the lagged regressed zonal wind. Figure 2.11 shows that the downward-phase Kelvin waves occupies stratosphere while upward-phase Kelvin waves lie in the troposphere, which is consistent with the results in section 2.4.5. Theoretical local vertical wavenumber could be calculated from the dispersion relationship $m = \frac{N}{c_x - \overline{u}}$, where $N = 0.024s^{-1}$ (see table 2.3). Background zonal wind $\overline{u}$ is defined as the zonal mean of the zonal wind and both $\overline{u}$ and m varies with height [Andrews et al., 1987]. However, different authors followed different approaches to calculate it. For example, Yang et al. [2011a] used a temporal-zonal mean of the 10°S-10°N latitudinal average over 70 - 20 hPa levels. Holton et al. [2001] used the temporal mean of zonal wind at Nauru island. Although the dispersion equation seems simple to use, the phase speed of the filtered signal c_x and the background wind

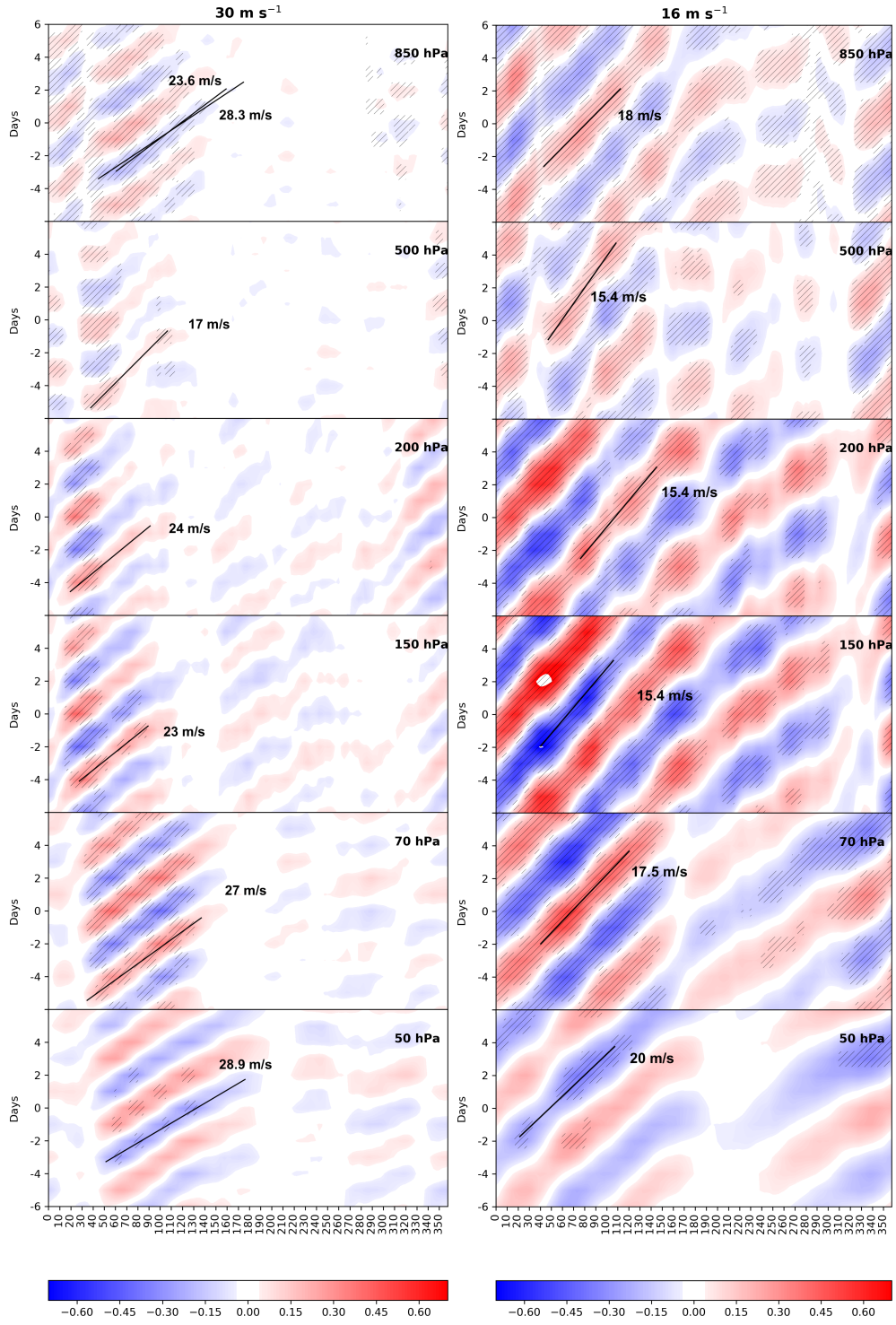

Figure 2.10: Lagged regression of unfiltered zonal wind anomalies averaged between 10°S and 10°N (shaded at interval of 0.01 m s^{-1}) based on the wavelet-filtered zonal wind at 850 hPa at 30 m s^{-1} (first column) and 16 m s^{-1} (second column). The rows represent the regressed unfiltered zonal wind anomalies at 850, 500, 200, 150, 70, and 50 hPa, respectively. The dashes refers to locations that are statistically significant different from zero above the 90% level using student's t-test. Slanted lines mark reference phase speeds.

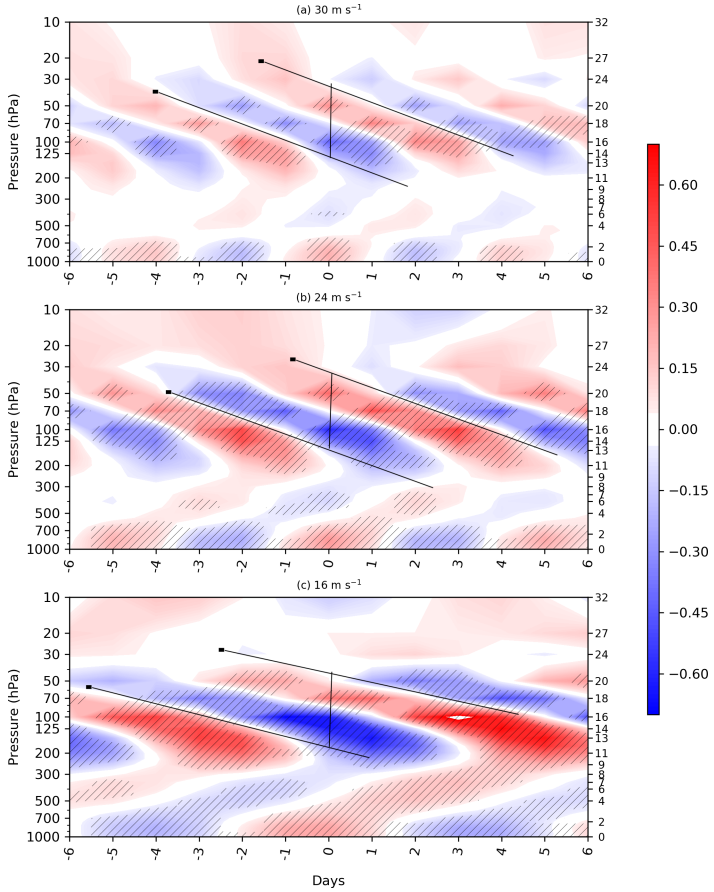

Figure 2.11: Time-height maps of the regressed unfiltered zonal wind anomalies (shaded at interval of 0.1 m s^{-1}) averaged between 10°S and 10°N based on wavelet-filtered zonal wind at 850 hPa at (a) 30 m s^{-1}, (b) 24 m s^{-1}, and (c) 16 m s^{-1}. The dashes refer to locations that are statistically significant different from zero above the 90% level. Slanted lines mark reference phase speeds. The vertical line between the slanted lines refer to the observed vertical wavelength.

$\overline{u}$ could be computed using different approaches as the following: (1) The observed phase speeds change with height far from the base level of the wavelet index, and hence they deviate from the targeted phase speed, as we discussed in the previous paragraph, (2) The background profile of the zonal wind changes with height, and averaging it may reduce the value of the $\overline{u}$, given the tilted structure of the QBO, (3) Although m is the local vertical wavenumber, the observed vertical wavenumber might not be a good representation of a local vertical wavenumber given the vertical resolution of the data; also it not clear how to estimate the depth of the vertical layer associated with the background zonal wind that has the most impact on the Kelvin waves, (4) The Kelvin waves (and all equatorial waves) have been dynamically rooted as perturbations superimposed on the mean zonal flow $\overline{u}$. Yet

statistically, they are considered as a deviation from the temporal and zonal mean flow as those wave are filtered in the two dimensional time-space or frequency-wavenumber domains. $\overline{u}$ is considered as the climatology of the zonal mean zonal flow. Yet, instead of using the climatology of the zonal mean zonal flow, we used the composite the zonal mean zonal wind over the course of active periods of the wavelet index. Also, given the localization of the wave at 80°E, we considered the zonal wind at 80°E, and (5) Strong vertical shear of the background zonal wind could modify the local vertical wavenumber.

To calculate the vertical wavelength of the stratospheric Kelvin waves, we found the background wind $\overline{u}$ associated with each targeted Kelvin wave. To do that, we applied a 15-day moving average on the squared wavelet indices at various phase speeds; then, we choose all dates of events with an amplitude higher than the mean of the 15-day moving average on the squared wavelet indices. We calculated the mean of the zonal mean of the zonal wind averaged between 100 and 30 hPa along the course of selected events. The calculated theoretical vertical wavelengths of the 30, 24, and 16 m s^{-1} stratospheric Kelvin waves are 7.7, 6.4, and 3.9 km when the background wind speeds $\overline{u}$ are 0.2, -0.36, and 0.4. We repeated the calculation again using the zonal wind at 80°E instead of the zonal mean of the zonal wind. The theoretical vertical wavelengths at the aforementioned phase speeds at 80°E are 8.2, 6.9, and 4.5 when the background wind speeds are -1.86, -2.3, -1.7 (see Table **??** for vertical wavelengths at other speeds). We also conducted those calculations again using the zonal wind at 80°E and 100 hPa, the vertical wavelengths of the 30, 24, and 16 m s^{-1} stratospheric Kelvin waves were 9.2, 7.7, and 5.6 km when the background wind is -5.6, -5.3, and -6 m s^{-1}. The vertical wavelengths increase with the background zonal easterlies, and stronger easterlies conflate when conducting the vertical average of the zonal wind. The observed (directly estimated from Fig. 2.11) vertical wavelengths for the 30 and 24 m s^{-1} are around about 10 km and they decrease a little for the 16 m s^{-1} signals. It hard to find an accurate estimation not only because subjective measurements are prone to human errors, but also the vertical resolution is not fine enough to get precise measurements. Nevertheless, estimating the vertical wavelengths is still useful when comparing with theoretical wavelengths. The observed vertical wavelength of the 16 m s^{-1} wave is roughly twice the calculated value. This mismatch between the observed and the theoretical vertical wavelengths encouraged us to recalculate the theoretical vertical wavelength using the background wind at each available vertical level between 100 and 30 hPa. We found that the strongest easterly background zonal wind speed is not sufficient to match the observed vertical wavenumber. Also, the observed phase speeds, which could deviate from the target speeds far from the base longitude and level, do not account for the the mismatch between the observed and theoretical wavelengths. Hence, we think that it is necessary to revisit the assumptions used to derive the dispersion equations. The vertical wind shear of the background wind (Fig. 2.5), which is missing from the model used to derive the dispersion equations in Table 2.3, might tilt the wave axes and hence change the vertical wavelength.

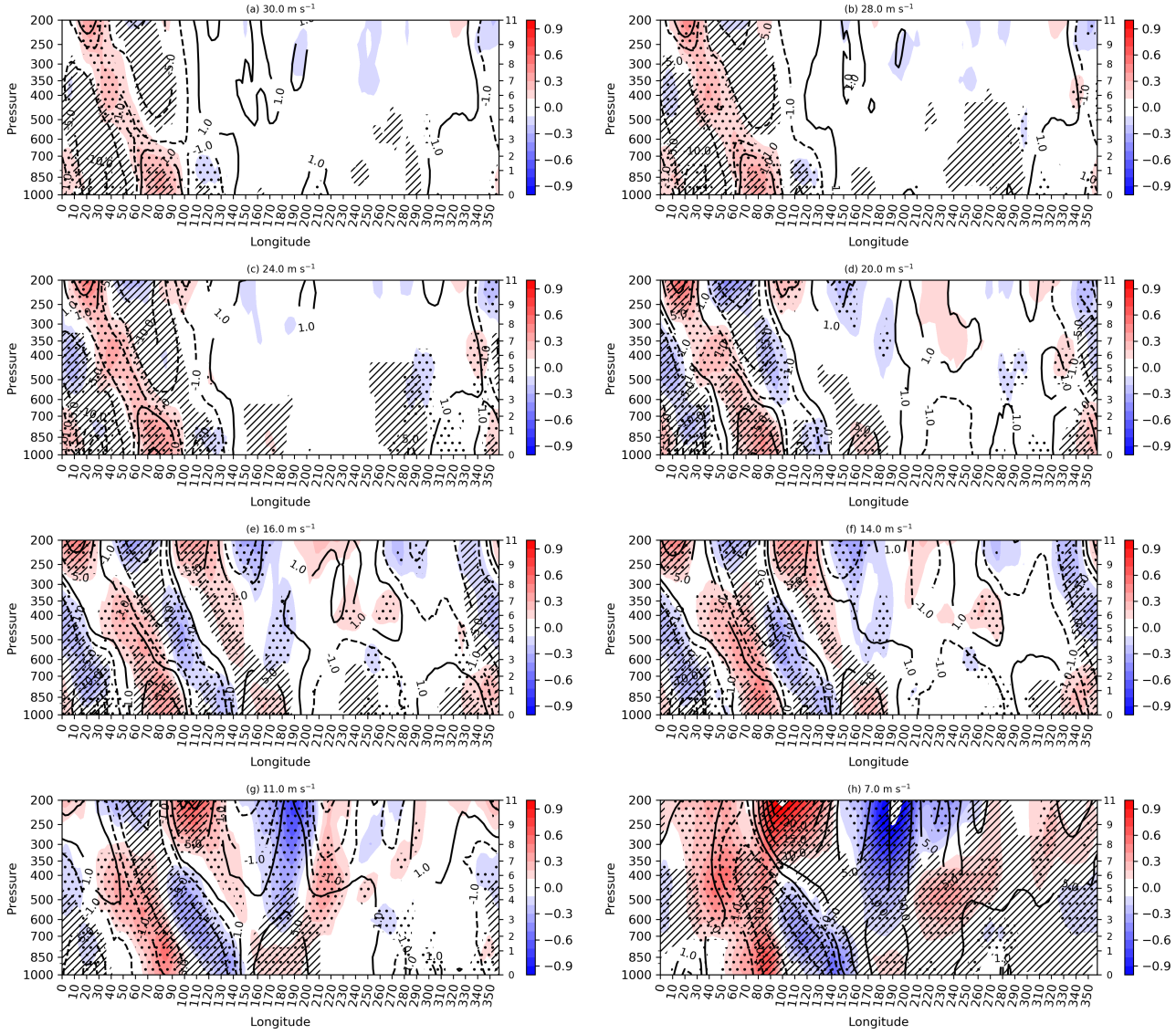

Figure 2.12: Longitude-level regressed map of equatorial zonal wind anomalies(shaded at interval of 0.1 m s^{-1}) and geopotential anomalies (black contours at interval of 5 m^2 s^{-2}, where solid and dashed black contours represent positive and negative geopotential anomalies) based on wavelet-filtered zonal wind at 30, 28, 24, 20, 16, 14, 11, and 7 m s^{-1} at 80°E. Dots and hatches indicate that the regressed zonal wind and geopotential anomalies are statistically significantly different from zero above the 90% level using a student's t-test. This figure is similar to Fig. 2.7, yet with focus on the tropospheric Kelvin component.

In this paragraph, we discuss the properties of the tropospheric Kelvin waves. The theoretical tropospheric vertical wavelengths increases with the horizontal wave speed as expected from dispersion equation (Table 2.3). The observed horizontal wavelengths λ_x the 30, 28, 24, 20, 16, and 14 m s^{-1} Kelvin waves seem to be invariant if we consider the waves

that begin roughly from 10-20°E to 100°E at 1000 hPa as a full cycle waves (Figs. 2.12a-f). The tilts $\frac{\lambda_z}{\lambda_x}$ of the aforementioned Kelvin waves (Figs. 2.12a-f) change by nearly a couple of degrees among the aforementioned phase speeds. Hence, the vertical wavelength λ_z could be also invariant with the aforementioned phase speeds. We did not measure the tropospheric vertical wavelength directly from Fig. 2.11, where the vertical resolution of the dataset in the troposphere is much better than that at the stratosphere, because it is difficult to get a measure of the vertical wavelength without touching the elbow joint. If the tilt of the waves is invariant, then the ratio of the quasi Doppler angular frequency to Brunt-Väisälä frequency has to be constant,

$$\frac{\lambda_z}{\lambda_x} = \frac{\omega - k\overline{u}(z)}{N} \approx constant \tag{2.2}$$

Therefore, waves at different frequencies (hence phase speeds) might favor different environmental static stability conditions (Eq. 2.2). To get more sense of the variation of the N with the phase speeds and the background zonal wind, we set the vertical wavelength to 16 Km, horizontal wavelength to wavenumber four. Then, for demonstration, N values are contoured at different phase speeds (shown on the horizontal axes of Fig. 2.13) and background zonal wind (presented on the vertical axes of Fig. 2.13). Figure 2.13 shows that fast Kelvin wave exists at high Brunt-Väisälä frequency. When the Kelvin wave speed approaches the mean background wind speed, N approaches infinity (see the upper left corner of Fig. 2.13). Also, waves during background easterlies sense a slow variation of N, while waves during background westerlies could sense a rather rapid change of N. The relationship between the phase speeds of the convectively coupled equatorial waves and static stability lie at the heart of tropical wave dynamics. In their pioneering paper, Wheeler and Kiladis [1999] found that the convectively coupled Kelvin waves project on shallower equivalent depths than those suggested by deep convection. They attributed this reduction of the phase speed of the convectively coupled waves to either a reduction of the static stability felt by the waves due to the convection or that the superposition between the first baroclinic mode (convective heating) and the second baroclinic mode (stratiform heating). We found that the tilts of the Kelvin waves between 30 and 14 m s^{-1} (Fig. 2.12a-f) are a semi invariant, then the tilts change at 11 and 7 m s^{-1} (Fig. 2.12g-h). The semi invariance of the tilt of the Kelvin wave across different phase speeds (especially those the fastest analyzed in this study) raises the

question whether the superposition between the convective and stratiform associated modes, instead of the reduced static stability, is the basic mechanism behind the tilt of the wave and the speed reduction. In the beginning of this paper, we raised some questions regarding whether the tilt of Kelvin waves emerges from a superposition between baroclinic modes, and whether we can understand the tropospheric wave as a simple upward-phase wave. Although answering these questions deserves further analysis (e.g. Matching the observed vertical wavenumber to the linear wave theory), we think that structure of the wavenumber four upward-phase and downward-phase Kelvin waves as apparent in the dynamical fields localized over the Indian Ocean could be understood in terms of plane wave dynamics.

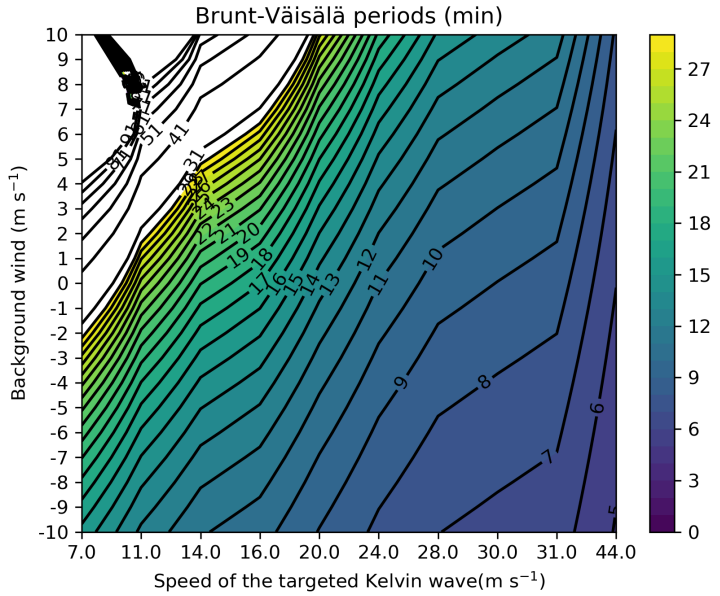

Figure 2.13: Brunt-Väisälä periods as a function in the Kelvin wave velocity and background zonal wind ($N = m(c - \overline{u})$) given that the vertical wavelength is 16 km. Shading includes only Brunt-Väisälä periods less than 31 minutes.

2.5 Discussion and conclusion

2.5.1 The Upward and Downward-Phase Waves and the Normal Mode Assumption.

Upward and downward-phase Kelvin waves centered at wavenumber four over the Indian Ocean spanning from 3.9 days to 16.5 days were analyzed using both the discrete

Fourier transform and wavelet regression techniques. We found that the downward-phase component of the 30 m s^{-1} Kelvin waves as represented by the zonal wind anomalies dominates in the stratosphere with extension in the upper troposphere, while the upward-phase component of the 30 m s^{-1} Kelvin waves dominates in the troposphere with an extension in the lower stratosphere, which is consistent with Yang et al. [2011a], Randel and Wu [2005], Wheeler et al. [2000]. Both the upward and downward-phase waves overlap at the elbow joint, which is thought to be the source of the Kelvin waves, although it is more elevated than the climatological diabatic heating. Slower waves, as the 16 m s^{-1} Kelvin downward-phase wave, weaken sharply near 70 hPa. Similar weakening of the Kelvin wave at 70 hPa was observed by Yang et al. [2011a], who analyzed Kelvin waves interactions with QBO during 1993. Fast Kelvin waves have phase speeds generally larger than the background zonal wind, so kelvin wave cannot deposit their energy to the mean flow via the critical layer interaction. But Kelvin wave energy could be modulated by the vertical wind shear. For example, westerly wind shear between 150 and 70 hPa could decrease the tilt of the Kelvin wave planes, thereby reducing wave energy as the parcel oscillation axes tilts horizontally. The 7 m s^{-1} Kelvin waves show more overlap between the downward and upward-phase phase components. Moist dynamics are thought to dominate the slow Kelvin waves. Upward and downward-phase Kelvin waves as represented in the regressed geopotential anomaly, temperature, and vertical wind fields show the same patterns as the zonal wind discussed above (More about that in the next subsection). We think that plane wave dynamics is essential for understanding wavenumber four Kelvin waves localized over the Indian Ocean in the light of the observed upward and downward-energy Kelvin waves emanating from around the elbow joint. The dominance of only one component of Kelvin waves (upward-phase) rather a reflections of waves in the troposphere over the Indian Ocean suggests that we can abandon the well-known normal mode representation of tropospheric wavenumber four Kelvin waves over the Indian Ocean. This is the most important finding in the manuscript that we found from the upward and downward-phase decomposition technique. To justify that result, we discuss, in the next subsections, the extent to which the structure and the characteristics of the upward and downward-phase waves fit plane wave dynamics. Limitations of the current analysis is also discussed.

2.5.2 Structure of the Upward and Downward-Phase Waves.

The regressed patterns of the dynamical fields suggest that the dynamics of the upward-phase and downward-phase Kelvin waves are similar as follows: The zonal wind and geopotential anomalies are in phase for both the upward-phase and downward-phase Kelvin waves as shown in Figs. 2.7, 2.14, indicating that the horizontal pressure gradient is the principle force acting on the fluid in the x-direction. The relationship between the zonal wind and geopotential could be derived from the momentum equation in the x-direction as by Andrews et al. [1987] and Roundy and Janiga [2012]. The vertical velocity (hence, zonal wind) and temperature anomalies are in quadrature in both the upward-phase and downward-phase waves (Figs. 2.9, 2.14), thereby the downward motion is on the west of the warm anomaly and on the east of the cold anomaly. This leads to an eastward propagation of the phase lines and also indicates that there is no upward flux of heat. The relationship between temperature and vertical wind is derived from the thermodynamics equation or by considering the thermal wind in the y-direction [Andrews et al., 1987]. The relationship between the vertical $\hat{w}$ and zonal velocity $\hat{u}$ is $\hat{w} = -\frac{k}{m}\hat{u}$, under the Boussinesq approximation [Roundy and Janiga, 2012]. The vertical wavenumber m is negative in the stratosphere and positive in the troposphere; therefore, the vertical and zonal wind are in phase in the stratosphere and out of phase in the troposphere (Figs. 2.8, 2.14). Contrary to the vertical wavenumber m, the horizontal wavenumber k is positive in both the troposphere and the stratosphere. The relationship between zonal wind and geopotential, and also between vertical velocity and temperature anomalies are not functions of the vertical wavenumber, thereby they show the same pattern in both the troposphere and stratosphere. The vertical wind could be related to the zonal wind as

$$\hat{w} = -\frac{\omega^2}{N^2 k^2}(m - \frac{i}{2H})\hat{u} \tag{2.3}$$

using an Eulerian zonal-mean log-pressure model with relaxing the Boussinesq approximation (see section 4.7 of Andrews et al. 1987 or section 12.5 of Holton and Hakim 2013), where H is the scale height, ω is the angular frequency. Under this model, the zonal and the vertical wind deviate from the in phase relationship in the stratosphere and also depart from the out of phase relationship in the troposphere. These deviations depend on the magnitude difference between m and $(2H)^{-1}$. As the vertical wavenumbers (see Table 2.3) are at least an order of magnitude larger than the $(2\mathrm{H})^{-1}$, it is reasonable to use the Boussinesq approximation

by ignoring $(2H)^{-1}$ when compared to m.

Wallace and Kousky [1968, see their Fig. 7] presented a schematic for the stratospheric plane Kelvin wave. To complete the picture, we present two schematics that include both the tropospheric and stratospheric Kelvin wave for fast and slow Kelvin waves (Fig. 2.14), suggesting structures of the waves consistent with the analyzed data and plane wave dynamics. The weakening of the downward-energy Kelvin wave just beneath the elbow could be understood in terms of destructive interface between the upward-energy and downward-energy components (see Fig. 2.7, 2.12). The upward-energy and the downward-energy propagating waves could be produced experimentally in a tank, as internal gravity waves, using a smoothly stratified fluid with a wave source in the middle of tank [Mowbray and Rarity, 1967]. These internal waves are produced if the frequency produced by the wave source is less than the Brunt-Väisälä frequency of the fluid. The tropospheric and stratospheric Kelvin waves was also simulated by solving a model of primitive equations [e.g. Wheeler and Nguyen, 2015].

The structure of the CCEW deviates from that of pure internal Kelvin waves. For example, the upward-phase component of the 30 m s^{-1} signal depicts a quadrature relationship between the temperature and the zonal wind (hence, vertical motion), which maintains the propagation of internal gravity phase wave fronts. Yet, the 7 m s^{-1} signal conveys an in-phase relationship between the temperature and the vertical motion, which might support the growth of the CCEW under the paradigm of wave-conditional instability of the second kind [CISK, Straub and Kiladis, 2003]. The transition from the dry gravity wave structure to the CCEW depends not only on the phase speed but also on height. Straub and Kiladis [2003] found an in-phase relationship between the temperature and zonal wind at 300 hPa, but a quadrature relationship at 700 hPa based on Kelvin wave filtered between the 8 and 30 m s^{-1} dispersion lines.

2.5.3 Characteristics of the Upward and Downward-phase Kelvin Waves.

Results suggest that Kelvin waves change their horizontal phase speeds, and hence zonal wavelengths, as they propagate vertically, in manner to match the frequency of the 850 hPa base index. In other words, the regression technique diagnoses all correlated signals with the same frequency, and thus projects on waves with different phase speeds. Regression

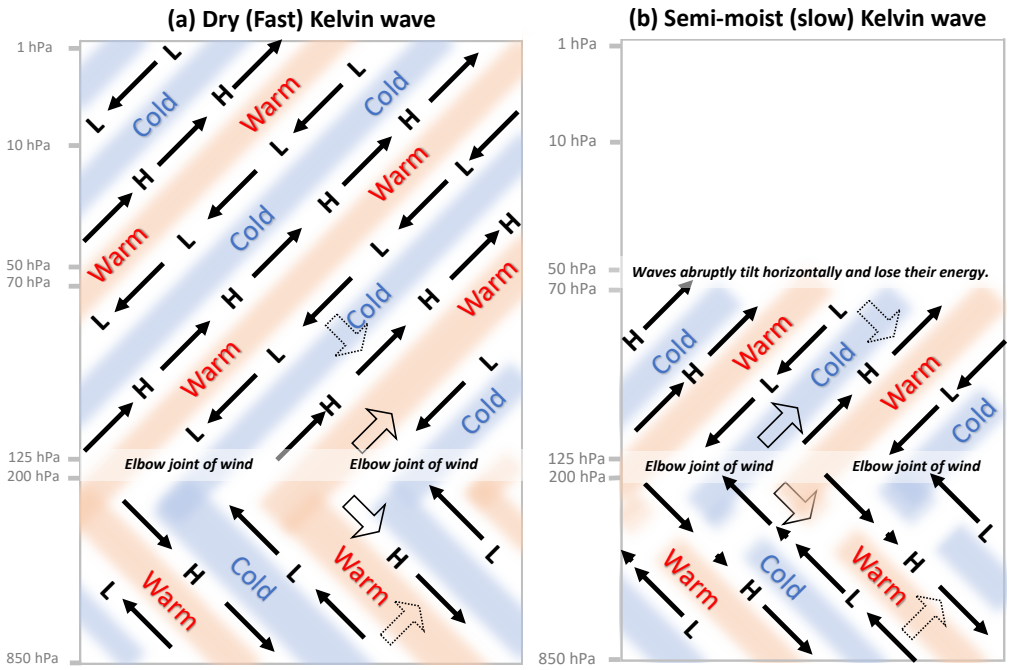

Figure 2.14: Schematics of (a) dry Kelvin wave and (b) semi-moist Kelvin wave. L and H symbols refer to low and high geopotential height anomalies. Bold solid and dotted arrows refer to the direction of the group velocity and phase velocity. Little wind arrows and fading of colors of the warm and cold belts represent the weakening of the downward plane wave in the middle of the troposphere due to its interference with the upward plane wave.

analyses show that the 16 m s^{-1} Kelvin waves reach their minimum phase speed at around 500 hPa, and accelerate in the lower stratosphere (Fig. 2.10), and their phase speed peaks in the upper stratosphere. Different phase speeds of the Kelvin waves project on different dispersion curves as suggested by the Wheeler and Kiladis diagram [Wheeler and Kiladis, 1999]. The low slope (low phase speed) dispersion line represents moist wave or wave encountering easterly background wind, or both. On the other hand, large slope (high phase speed) dispersion line expresses dry waves or waves propagating in westerly background wind or both Dias and Kiladis [2014].

The vertical wavelengths of the stratospheric plane waves are deduced from the dispersion relationship (Table 2.3). Although precise measurements of the vertical wavelengths weren't feasible, the observed vertical wavelengths of the 16 m s^{-1} is apparent to be larger than the corresponding theoretical wavelength. We found that the background zonal wind did not account for this mismatch. At this point, revising the premises used to derive the

dispersion equation is of an essence. The dispersion equations listed in Table 2.3 do not include the vertical wind shear of the zonal wind, which could tilt the wave and hence change its wavenumber.

Contrary to the stratospheric plane waves, dispersion equations have not been used, by other authors, to study the tropospheric Kelvin waves as they were understood in terms of baroclinic modes (or standing waves). By using the upward-downward filtering technique, we found that the tropospheric Kelvin waves behave as upward-phase waves consistent with a downward group velocity. Under the normal mode thinking, the inclusion of higher-order baroclinic modes explain the speed reduction of the tropospheric Kelvin waves. On the other hand, under the plane wave dynamics, the reduced effective Brunt-Väisälä frequency [Emanuel et al., 1994] account for the reduction of the wave speed. For example, the 30 m s^{-1} Kelvin wave could exist under different background zonal winds ranging from -10 to 10 m s^{-1} when the Brunt-Väisälä varies from 6 and 13 minutes as demonstrated in Fig. 2.13. The red power spectrum of eastward-moving convective signals in the tropics suggests that Kelvin waves can occur over a wide range of frequencies or phase speeds as they respond to different background wind and convective states (e.g., Salby and Garcia 1987, Roundy 2019).

We found that the tilt of the tropospheric Kelvin wave does not vary substantially over a subset of speeds analyzed in this study (30 to 14 m s^{-1}). For example, the 30 m s^{-1} Kelvin wave, which is the fastest wave that we analyzed, is weakly associated with rainfall signals (see Fig. 2.3), yet still nearly shows the tilted structure of the 14 m s^{-1} Kelvin wave. If dry waves show similar tilt to moist waves, superposition between the baroclinic modes cannot be the primary explanation for the tilt. On the other hand, static stability conditions along with the background wind speed might account for the speed variability of the wave. The plane wave view of the tropospheric Kelvin wave proposed in this work provides a pathway based on linear gravity wave dynamics, where the tilt is a function in the Brunt-Väisälä and wave frequencies.

2.5.4 Limitations and Future Work.

The results presented in this work are based on the structure of wavenumber four Kelvin waves filtered over the Indian Ocean. We think that a rather comprehensive conclusion on

the plane wave dynamics of the tropospheric Kelvin wave should be based on Kelvin waves filtered at different wavenumbers and locations. Although we analyzed the structure of the Kelvin waves among a range of phase speeds, faster Kelvin waves could be analyzed using a relatively higher temporal resolution reanalysis. A higher vertical resolution, especially in the stratosphere, is essential for a precise evaluation of the suggested mismatch between the observed and theoretical vertical wavelength.

The preference of the elbow joint (wave source) to be settled at about around 200 hPa deserves more analysis on the nature of the diabatic heating associated with the Kelvin waves at different phase-speeds and locations. Also, it is not yet clear how the superposition between plane Kelvin waves at different wavenumbers and speeds resembles the over-turning circulation, which is simple to explain in the normal mode school of thought, found when filtering Kelvin wave over a band of wavenumbers and frequencies.

CHAPTER 3

On the Interaction Between Kelvin Waves at Different Phase Speeds and the Background Flow.

3.1 abstract

Kelvin waves have been theoreticized to be absorbed near the critical layer, where the phase speed matches the speed of the background flow. Nevertheless, it is not clear, through observations, how the structure of the Kelvin waves evolves near the critical layer or in response to vertical wind shear with or without a critical layer. A novel varying-coefficient regression technique that has been used to study evolving relationships across the seasonal cycle, is used to capture how the wavelet-filtered waves with a specific speed appear in different background winds or vertical shear regimes or a combination of both. Results show a relaxation of the in-phase relationship between the zonal wind and geopotential height anomalies at slower Doppler-shifted speeds, followed by the appearance of the Gill pattern at further reduction of the Doppler-shifted speed, demonstrating a lack of dominant Kelvin wave signals in those conditions. We define the "observed critical layer" as the layer where the signals consistent with Kelvin waves fade away irrespective of the value of the Doppler-shifted speed, which reduces to zero at the "theoretical critical layer." Results show that wave structures consistent with Kelvin waves are not present among westerly and easterly vertical shear of the zonal wind if the critical layer lies in the shear layer. The second part of the paper presents the dispersion equation of the Kelvin wave under vertical shear. The phase speed of the Kelvin wave proportionally increases with the Richardson number (and hence proportionally decreases with the vertical wind shear). The Richardson number varies with the vertical resolution of the data used, adding uncertainty to the calculated phase speed of the wave in the presence of wind shear. **Keywords** — Kelvin wave, background wind, wind shear, critical layer, Richardson number.

3.2 Introduction

Internal gravity waves [Fritts and Alexander, 2003] are absorbed by the flow before approaching the critical layer, in which the phase speed of the wave matches the speed of the flow moving in the same direction [Bretherton, 1966, Booker and Bretherton, 1967]. Near the critical layer, the wavefront aligns with the flow, trapping the wave's momentum, and horizontal phase speed, with respect to the Earth, of the wave matches the flow speed. Hence, the frequency of the wave relative to the flow diminishes to zero. The frequency of the wave relative to the flow is known as the Doppler-shifted frequency or quasi-Doppler shifted frequency as suggested by Gerkema et al. [2013] to distinguish the classical Doppler shifting between wave source and observer from that associated with two different observing references (i.e., those of the Earth and the flow) as the case here.

Kelvin waves behave similarly as they approach critical layers [Holton, 1970, Lindzen, 1970]. The absorption of Kelvin waves and small scale gravity waves in eastward flow and Rossby-gravity waves and especially the small scale gravity waves [Pahlavan et al., 2021b] in westward flow contributes to the downward propagation of the zonal wind of the quasi-biennial oscillation [QBO, Baldwin et al., 2001a] theory introduced by Lindzen and Holton [1968].

Kelvin and small scale gravity wave absorption contributes to the descending of the westerly phase of the QBO, while the evanescence of small scale gravity waves and to less extent the Rossby-gravity waves are found to be associated with descending of the easterly phase of the QBO [e.g., Ern and Preusse, 2009a,b, Yang et al., 2011b, 2012, Kim and Chun, 2015a,b, Pahlavan et al., 2021a,b], indicating that the source of the downward zonal wind is the absorption of the upward waves' momentum as theorized by Lindzen and Holton [1968].

Most of the studies about the interaction between Kelvin waves and the QBO are either theoretically-based or include analysis of certain QBO events associated with Kelvin wave signals filtered at a bulk of wavenumbers and frequencies, which might wipe out details about the evolving structure of the Kelvin waves while approaching the critical layer. In this study, we apply a combination of wavelet analysis and a new form of linear regression to analyze the interaction of eastward-moving waves at specific phase speeds centered at a given geographical location and pressure level as they vary with the background flow at certain speeds rather than with respect to the QBO phases or events. Kelvin waves

in the stratosphere emerge in response to motion induced in the stratosphere from the troposphere. The directly forced motions can be associated with different types of waves or forced disturbances in the stratosphere. Whether a given forced disturbance yields a Kelvin wave depends at a minimum on whether the quasi-Doppler shifted dispersion curve includes a Kelvin wave at the timescale of the forcing. When the direct forced signals at a given speed project directly onto Kelvin waves, Kelvin-like signals then appear in the regression maps on the same timescales. The approach diagnoses Kelvin wave-like signals when such waves dominate in a given background wind setting, and reveals other types of disturbances under conditions that do not favor Kelvin waves, allowing us to intuit from the wave statistics whether Kelvin wave signals are consistent with the theory. Non-Kelvin disturbances are anticipated under conditions in which Kelvin waves do not form, because forcing from the troposphere occurs over a wide range of scales including those in which Kelvin waves cannot occur in the given environment [Salby and Garcia, 1987]. The characteristics of the waves at different background flow speeds that are greater than, less than, or equal to the phase speed of the Kelvin waves are documented using the 30 years of ERA-interim reanalysis. To accomplish the objective, we use a novel regression method that enables us to set a specific value of a background state variable (such as background zonal wind at a given height), in order to diagnose the linear relationship between a wavelet-filtered predictor index and fields of data during the specified background condition. The wavelet and the regression techniques are discussed in section 4.4. The behavior of the filtered waves at different background wind speeds is discussed in section 3.4.3, followed by discussing the behavior of the wave during variable wind shears and background winds in section 3.4.4. A dispersion equation for the Kelvin waves within a background wind shear is derived in section 3.5.

3.3 Data

Daily ECMWF interim reanalysis (ERA-I) data from 1979 to 2017 on 2.5° grid were used [Dee et al., 2011]. High resolution radiosonde observations during the dynamics of the Madden Julian Oscillation (DYNAMO) field campaign were used to calculate the Richardson number [Johnson et al., 2019]. Anomalies were constructed by first regressing the raw data against the first four harmonics of the seasonal cycle, then by subtracting the mean and predicted seasonal cycle of 1980-2010 from the raw data [Narapusetty et al., 2009a]. Data

used to represent the background state conditions retained the longterm mean and seasonal cycle.

3.4 Methods

3.4.1 Wavelet-Based Index.

Contrary to the common technique of filtering Kevin wave between two distinct equivalent depths and wavenumbers [Wheeler and Kiladis, 1999, Wheeler et al., 2000], data are filtered at a specific phase speed and wavenumber using a partial wavelet transform, to study the interaction of the wave signal at particular phase speed with a predetermined-speed of the background flow as we discuss in section 4.4.2. The wavelet kernel is designed following Roundy [2017b] and Shaaban and Roundy [2021a] as a two-dimensional array (see Eq. 3.1) where the rows and the columns represent the time t and longitude x.

$$\psi(x,t) = \frac{1}{\sqrt{a\pi}}\frac{1}{\sqrt{b\pi}}\cos(2\pi(f_x x - f_t t))\exp(-\frac{x^2}{b})\exp(-\frac{t^2}{a}) \tag{3.1}$$

The length of the time dimension is 200 days, which is enough to capture the slowest Kelvin wave. The longitude dimension matches the reanalysis data resolution 2.5° with 144 points in the 360°. Although wavenumber four is targeted, because it is a center of strong Kelvin wave activity in previous works [e.g., Wheeler and Kiladis, 1999], the localized filter implies a superposition between waves of different wavenumbers that peak at wavenumber four, a price paid for the sake of the localization. a and b are usually called the scaling factors, f_x and f_t are the spatial and temporal frequency. Parameter a is related to the temporal frequencies f_t as $a = 8\left(\frac{2\pi f_t}{2\pi}\right)^{-3/2}$ in order to localize each scale to include a similar number of cycles in the template. To apply the filter, the kernel is centered at our base longitude at 80°E along the equator, as we are interested in Kelvin waves over the Indian ocean, and at a particular day of the reanalysis, so the dot product between the kernel and the corresponding block of reanalysis data is the value of the wave index at that day. We used the zonal wind anomalies at different pressure levels to create the wavelet base index. Signals are selected from parts of the spectrum previously demonstrated to contain Kelvin wave-like signals [e.g., Roundy, 2019], though they may also include non Kelvin components. To find the value for the next day, the kernel is slid one day ahead, and the same dot product is repeated.

The wavelet index is the signal in the reanalysis data at the base point that best projects onto the 2D wavelet kernel. This index serves as the independent variable of the regression analysis. As reanalysis data is measured relative to an observer on the Earth, then the phase speed c of the patterns correlated with this wavelet index is the speed relative to an observer on the Earth, which could be calculated as $\frac{f_t}{f_x}$. We refer to the wavelet indexes with their phase speeds. For example, the 20 m s^{-1} index refers to the dot product of the 20 m s^{-1} wavelet kernel with the reanalysis. Hence, the 20 m s^{-1} index used in regression model targets patterns correlated with the 20 m s^{-1} signal at the base point and the pressure level.

3.4.2 The Varying-Coefficients Wavelet Regression and Statistical Significance Test.

The structure of the waves at different phase speeds c can be studied by regressing the dynamical fields of the reanalysis data against the wavelet indexes at different phase speeds. A linear regression between a centered predictor x and a similarly centered predictand y is the covariance between x and y divided by the variance of x. Yet, this wavelet regression doesn't enable us to analyze the structure of the Kelvin wave during a specific dynamical condition of the background flow (speed, wind shear, static stability, etc.). Roundy [2017a] developed a new form of linear regression that allows regression coefficients to evolve continuously across the calendar year by modeling the variance and covariance quantities used to calculate the regression slope coefficients based on the harmonics of the seasonal cycle. Roundy [2017a] showed that these two quantities have seasonal cycles, so that a fit of the seasonal cycle can be used to create continuously seasonally varying regression slope coefficients relating x and y. Yet these variance and covariance quantities can vary with other factors beyond the seasonal cycle, including the mean state background zonal wind. In this study, instead of allowing regression slopes to vary with the seasonal cycle, we allow them to vary with the background zonal wind, vertical shear of the zonal wind, and a combination of both. We replace the harmonics of the seasonal cycle in the matrix X of Roundy (2017a) with time series of the background variables of interest here. As an example, consider that we are interested in finding the structure of dynamical fields associated with the 22 ms^{-1} Kelvin wave at 50 hPa. Then, we create an index for the 22 m s^{-1} Kelvin wave at 50 hPa, and then project a selected dynamical field on this index. Yet, if we need to find the structure

of the wave signal only when the background flow (total wind speed) U has a specific value, for example, 11 m s^{-1}, which is half of the specified wave speed, then we create a regression model relating the wavelet filtered base index with fields of data in a way that allows the slope coefficients to vary continuously with the background flow indexes, as follows: (1) regress the time series square of the 22 m s^{-1} Kelvin wave index on the total wind along the equator at 50 hPa (to extract the relationship between wave variance and the background flow), (2) regress the time series of the products of the 22 ms^{-1} Kelvin wave index and any dynamical field (zonal wind anomaly, geopotential anomaly, etc) that we are interested to find its pattern on the same total wind at 50 hPa (hence, we get the relationship between the covariance and the background flow), (3) substitute the value of the background wind, 11 m s^{-1}, in the regression model in step 1 to find the estimated variance in the given background state and also substituting the same background speed in the regression model in step 2 to find the estimated covariance in the same state, (4) lastly, we get the slope coefficient when the background wind speed is 22 m s^{-1} by dividing the estimated covariance by the estimated variance calculated in step 3. The resulting regression maps show the waves at the base pressure level and longitude base point that occur at that speed and in the given base state. Regressed signal seen at other pressure levels or at distance from the base point show the part of the remote signal that is correlated in time with the signal near the base point. This remote signal will generally include altered wavenumber characteristics (which indicate changes in phase speed as the waves move between environments).

Following Roundy [2017a], we use a non-parametric bootstrap test. Our objective is to test whether the the varying regression coefficient is statistically different from zero, assuming the null hypotheses of no relationship. 10,000 samples of the wavelet index are created with replacement [see ch. 5 Wilks, 2011] then 10,000 regression coefficients are calculated, which form the sampling distribution against which the null value of zero is compared. We use the 90% confidence level, so if the slope lies between the 500 and 9,500 quantiles, then we reject the null hypothesis and the slope is statistically significant at the 90% level. Since these wavelet signals can contain more than just Kelvin waves (for example, they can also include eastward advected Rossby waves), conclusions about Kelvin waves are diagnosed not just by statistical significance of a difference from zero, but by the extent to which the regressed pattern takes on characteristics consistent with Kelvin waves. For example, a result that shows eastward flow in a trough on the equator, with cyclonic gyres to the north and south,

it suggests that Kelvin waves do not dominate wave signals at the given speed in the given background circumstances.

3.4.3 Regressed Wave Structures in Different Background Wind States.

Figure 3.1 shows regressed geopotential and wind anomalies at 50 hPa associated with the 24 m s^{-1} filtered wave at the same vertical level, 50 hPa, at specific background wind speeds using the varying regression technique described in section 4.4.2. The background wind U is the zonal mean zonal wind at 50 hPa at the equator. Figure 3.1a,b, and c represent the pattern of the $c = 24$ m s^{-1} filtered wave associated with -17, 9, and 17 m s^{-1} background flow. The speed adjusted for quasi-Doppler shifting, is $c - U$. Hence, for example, targeting the 30 m s^{-1} wave under background wind speed of 30 m s^{-1} indicates that the phase speed of the pattern relative to the background flow is zero m s^{-1} (which could not be a Kelvin wave).

Figure 3.1a shows an in-phase relationship between the wind and geopotential suggesting the presence of a Kelvin wave. The highest amplitudes of the Kelvin wave are over the Indian Ocean, reflecting the location of the base index and the localization of the wave. The in-phase relationship between the geopotential and wind relaxes as the background wind shifts from easterlies (Fig.3.1a) to westerlies (Fig.3.1a,c). Also, the meridional wind component intensifies with the strengthening of the background westerly flow. The deviation of the regressed wave from the Kelvin wave structure described by Matsuno [1966] occurs when the quasi-Doppler shifted speed $c - U$ is reduced from 41 m s^{-1} to 7 m s^{-1}. The same behavior was also found when targeting slower waves (e.g. 20, 16, and 14 m s^{-1}), and the quadrature pattern appears at slower westerly wind background flows as we target slower waves (not shown). The fading of the Kelvin wave structure with smaller the quasi-Doppler adjusted speeds encourages us to analyze the wavelet filtered waves in greater detail at slower quasi-Doppler adjusted speeds. Theoretical studies suggest that the gravity wave (and also Kelvin wave) decays before approaching the critical level [Bretherton, 1966, Booker and Bretherton, 1967, Holton, 1970, Lindzen, 1970]. Although fast Kelvin waves exist in the stratosphere and the mesosphere, only base indexes with speeds less than the maximum eastward velocity of the zonal mean background flow are considered. Box-plot diagrams are used to represent the range of the background zonal mean zonal wind at 70, 50, 30 hPa as shown in Fig. 3.2. The

basic state flow at those levels is negatively skewed due to the QBO [Baldwin et al., 2001a]. As the maximum value of the zonal mean zonal wind at 50 hPa is 17.3 m s^{-1} (see Fig. 3.2), then we select wavelet indexes targeting slower phase speeds than 24 m s^{-1} Kelvin wave shown in Fig. 3.1. Figure 3.3 presents regressed geopotential and wind anomalies at 50 hPa associated with the 20 and 16 m s^{-1} wave filtered at 50 hPa when the background speeds are 17 and 15 m s^{-1}. The corresponding quasi-Doppler adjusted phase speeds are 3 and 1 m s^{-1}. Negative gepotential anomalies with cyclonic motions straddle the equatorial Central and Western Indian Ocean, while a latitudinally narrow negative geopotential anomaly with easterlies lies to the east of the equatorial Maritime Continent. This pattern is similar to the famous Gill pattern [Gill, 1980]. At the aforementioned quasi-Doppler adjusted speeds, the wavelet index projects on a Gill-like pattern rather the Matsuno Kelvin wave, suggesting the possibility of the absorption of the Kelvin waves that were clearly observed at a faster quasi-Doppler adjusted speeds. A possible explanation of the Gill-type pattern is the response of the atmosphere to direct forcing from below under background conditions in which the local atmosphere cannot produce a Kelvin wave.

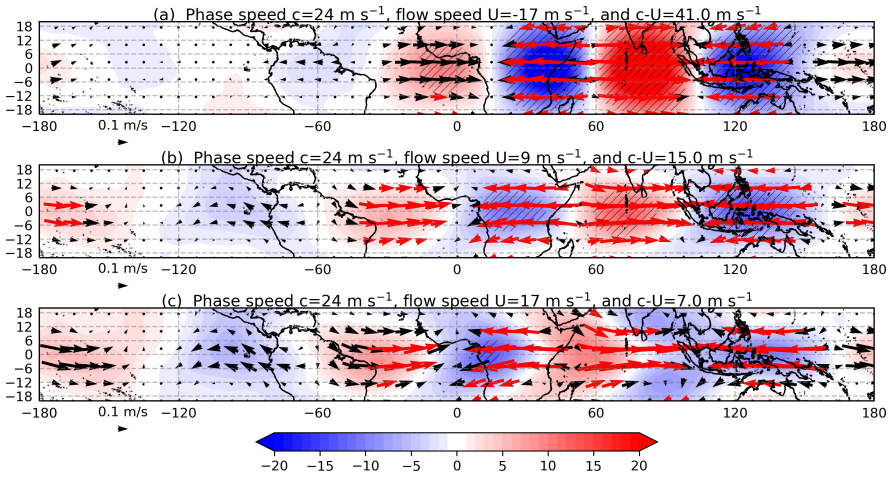

Figure 3.1: Shading represent regressed 50 hPa geopotential with an interval of 1 m^2 s^{-1} and 50 hPa wind vectors represent wind, with the key wind represents 0.1 m s^{-1}. The regressed geopotential and wind are associated with the 24 m s^{-1} wave filtered at 50 hPa when the zonal mean zonal wind (U) at 15 m s^{-1} is (a) -17 m s^{-1} (b) 9 m s^{-1} (c) 17 m s^{-1}. Red wind vectors and hatched geopotential are statistically significant at the 90% level using the 10,000 samples of the bootstrap test.

The lagged-longitude structure of the zonal wind and geopotential associated with the 14 m s^{-1} Kelvin wave filtered at 50 hPa at different background speeds U is depicted in

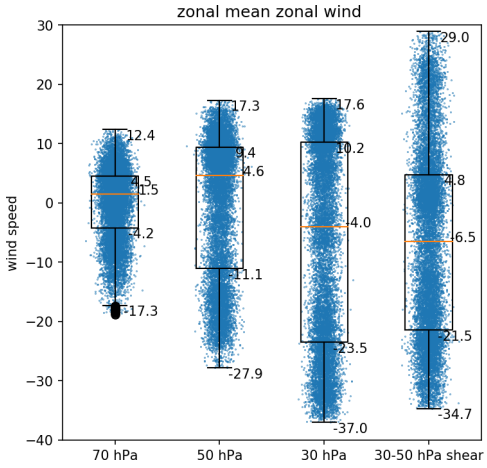

Figure 3.2: Box-plots overlaid with scatter plots of the zonal mean zonal wind at 70, 50, 30 hPa, and the 30-50 hPa wind shear. The red line inside the box represents the median. The box outlines the first (q1) and third (q3) quartile, and its width is the inter-quartile range (IQR). The whiskers' endpoints refer to the minimum (q1-1.5 IQR) and maximum (q3+1.5 IQR) values, and the points beyond the whiskers are considered outliers. The distribution of the zonal wind is also show in the scattered dots. The dots are spread randomly in the horizontal within their clusters to make it easier to view the distribution of events along the vertical axis.

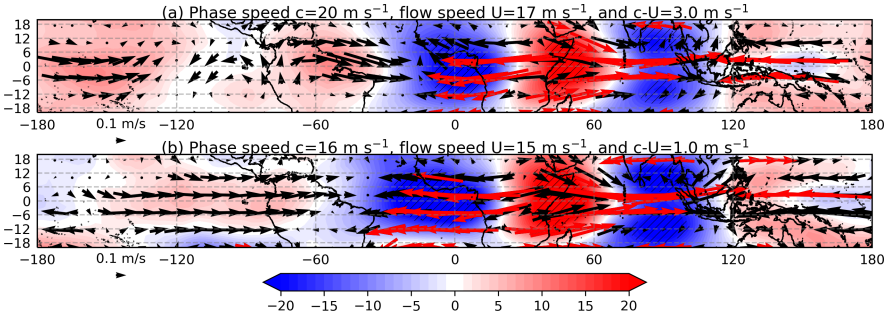

Figure 3.3: As in Fig. 3.1 except (a) the 20 m s^{-1} Kelvin wave is used when the background speed is 17 m s^{-1}, and (b) the 16 m s^{-1} is targeted when the background speed is 15 m s^{-1}.

Fig. 3.4. The phase lines imply an eastward phase velocity. The wave period is $\sim$ 7 days, consistent with the wavelet frequency, and it does not vary a lot with the background flow. The structure of the Kelvin wave is clear between the -19 m s^{-1} and 1 m s^{-1} background flows where the quasi-Doppler shifted speeds are 33 and 13 m s^{-1} as shown in Fig 3.4a and b. The regressed pattern at 1 m s^{-1} background flow is stronger when compared to the regression against the wavelet base index in -19 m s^{-1} flow. During 11 m s^{-1} westerly flow, the 14 m s^{-1} Kelvin disappears, as suggested by the quadrature relationship between

the zonal wind and the geopotential (which indicates that a Kelvin wave is no longer the dominant signal at that height). This behavior was also observed with the 20 and 16 m s^{-1} waves (see Fig. 3.3).The fading of the Kelvin waves at small quasi-Doppler shifted speed is a robust dynamical phenomena as it was also observed at 30 and 70 hPa using filtered-waves at different phase speeds among different background winds. At higher pressure levels, the background wind decreases, thus slower Kelvin waves could reach the critical layer.

The vertical structure of the regressed waves at different quasi-Doppler shifted speeds is shown in Figure 3.5. The lagged-vertical structure of regressed zonal wind and geopotential anomalies associated with the same wavelet index and background speeds, as in Fig. 3.4. The alternative weakening and strengthening of the zonal wind and geopotential along the phase lines results from the coarse resolution in the vertical and the logarithmic scale axes in the plotting algorithm. The phase lines imply a downward phase velocity that is consistent with the dynamics of the stratospheric Kelvin wave. Kelvin waves propagate vertically when the quasi-Doppler shifted speeds are 33 and 13 m s^{-1} as presented in Fig. 3.5a and b. Yet, when the background wind is adjusted so that the quasi-Doppler shifted speed is reduced to 3 m s^{-1}, a quadrature relationship between zonal wind and geopotential height anomalies suggests that a Kelvin wave signal is absent, consistent with the hypothesis that it is absorbed below the critical layer.

3.4.4 The Structures of Regressed Waves among Different Background Flows and Vertical Shears.

The association of the vertical shear of the zonal mean of zonal wind with the structure of the regressed waves is also analyzed using the same technique used with the varying background winds. The 30–50 hPa vertical shear index is defined as the zonal mean zonal wind at 30 hPa minus that at 50 hPa without dividing by the vertical spacing between the two levels to get more sense of the index values. We replace the background flow index with the 30–50 hPa vertical shear (see Fig. 3.2). Then, the dynamical variables (zonal wind, geopotential, etc) at 30 hPa (top of the shear layer) associated with the 24 m s^{-1} wavelet index at the same level are computed at different values of the 30–50 hPa wind shear. During easterly vertical wind shear (-12 m s^{-1}, Fig. 3.6), Kelvin wave structure is clear. Yet during the westerly shear (18 m s^{-1}, Fig. 3.6), the zonal wind anomalies are shifted eastward with

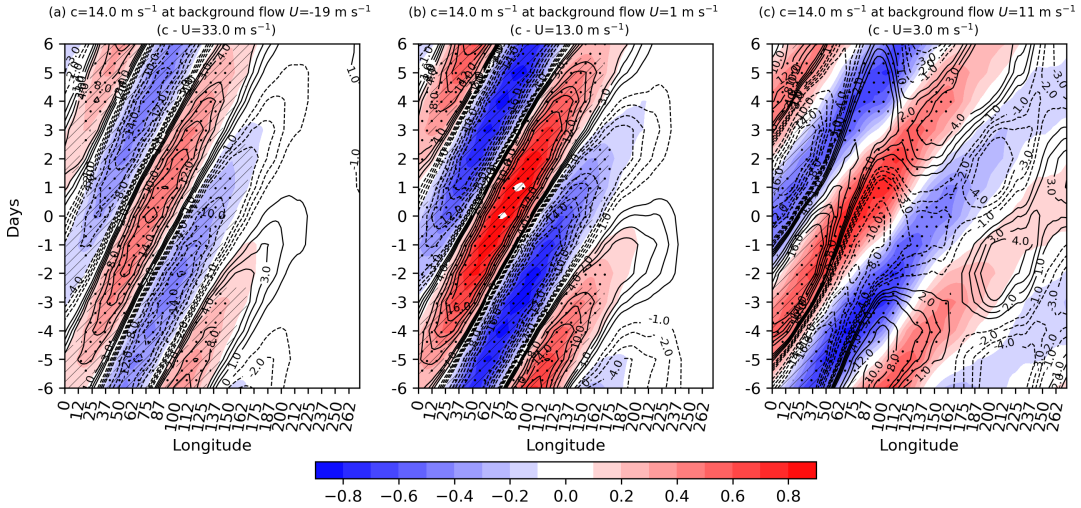

Figure 3.4: Lagged-longitude diagram of regressed zonal wind anomalies (shaded, interval of 0.1 m s^{-1}) and geopotential anomalies (contours, interval of 1 m^2 s^{-1} when values between -4 and 4 m^2 s^{-1}, and an interval of 2 m^2 s^{-1} otherwise) at the 50 hPa on the 14 m s^{-1} filtered wave at 50 hPa when the background flow at 50 hPa is (a) -19, (b) 1, and (c) 11 m s^{-1}. Dots and hatching indicate that the zonal wind and geopotential are statistically significant at the 90% level based on 10,000 sample bootstrap test.

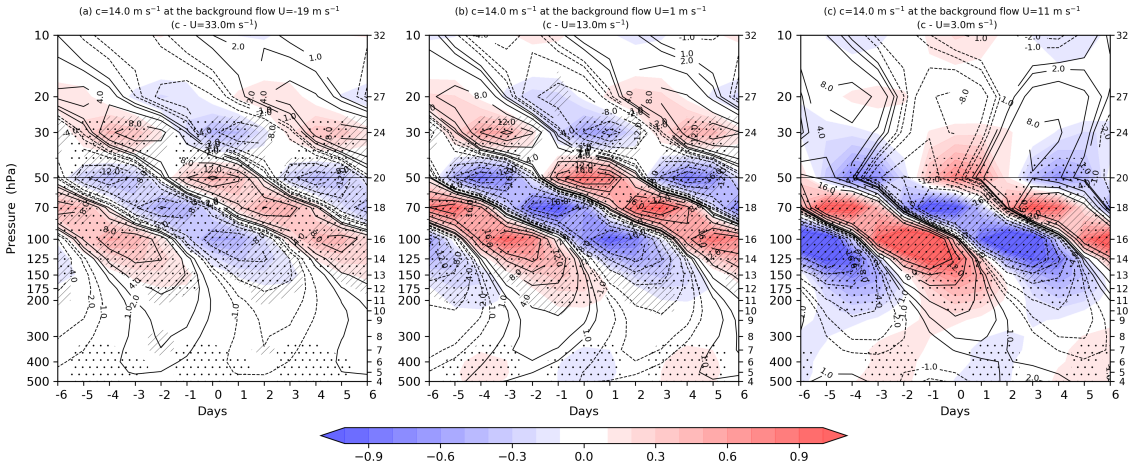

Figure 3.5: Lagged-vertical level map of regressed zonal wind anomalies (shaded, interval of 0.1 m s^{-1}) and geopotential height anomalies (contour, intervals -16, -12, -8, -4, -2, -1, 1, 2, 4, 8, 12, and 16 m^2 s^{-1}) on 14 m s^{-1} filtered wave at 50 hPa when the background wind at the same level is (a) -19, (b) 1, and (c) 11 m s^{-1}. Statistical test is the same as in Fig. 3.4.

respect to the geopotential anomalies, and the gepotential and zonal wind anomalies are weaker than that during the easterly vertical wind shear.

To further understand the behavior of the filtered waves during westerly and easterly

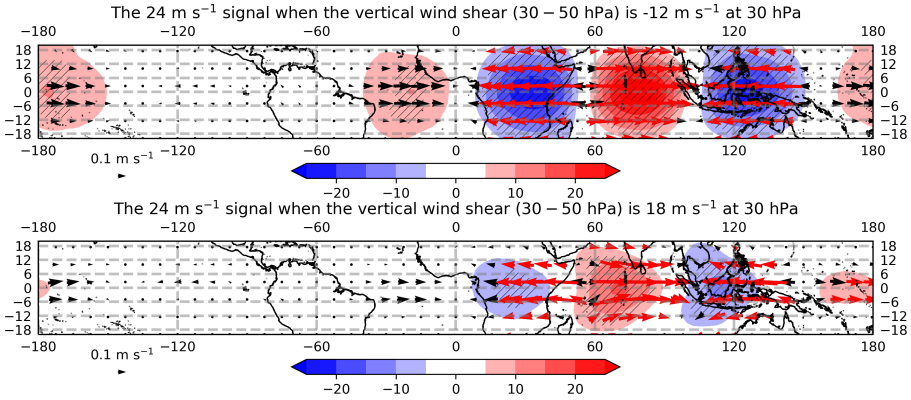

Figure 3.6: Regressed geopotential (shaded, interval of 5 m^2 s^{-1}) and wind anomalies at 30 hPa on the 24 m s^{-1} signal filtered at 30 hPa when the 30–50 hPa layer is -12 m s^{-1} (upper panel), 18 m s^{-1} (lower panel). Hatching represents statistically significant geopotential height anomalies and red vectors represent statistically significance at the 90% level based on 10,000 members bootstrap resembling.

vertical wind shear, we examine lagged maps of the 14 m s^{-1} filtered wave during both westerly and easterly shear at the base, 50 hPa, and the top, 30 hPa, of the 30–50 hPa shear layer. First, we present the 14 m s^{-1} wave at 30 hPa during -10 m s^{-1} and 18 m s^{-1} wind shear, as shown in Fig. 3.7a and b. It is clear that the 14 m s^{-1} wave maintains the Kelvin wave structure during the easterly shear (Fig. 3.7a), but it loses this structure during the westerly shear (Fig. 3.7a). The quadrature relationship between the zonal wind and geopotential persists with increasing westerly wind shear (not shown). The structure of the filtered waves at 50 hPa is opposite to that at 30 hPa as the Kelvin wave is maintained at 18 m s^{-1} westerly shear and disappears at the -24 m s^{-1} easterly shear. Yet, Kelvin wave characteristics are also observed at -10 m s^{-1} wind shear. The waves captured at -24 m s^{-1} (Fig. 3.7c) are slower than the Kelvin wave found during 18 m s^{-1} (Fig. 3.7d). Yet, we do not expect that a pattern that deviates from the Kelvin wave structure would obey the Kelvin wave dispersion characteristics. To summarize, the Kelvin wave structure intensifies with westerly shear at 50 hPa and easterly shear at 30 hPa.

The gradual evanescence of the Kelvin wave at 30 hPa with the westerly and at 50 hPa with the easterly shear might be attributed to the gradual reduction of the quasi-Doppler shifted speed somewhere between 30 and 50 hPa (hence the appearance of the critical layer). To test this hypothesis, we compare the regressed fields associated with the same shear profiles but with and without a critical layer. To do that, we use a multiple regression

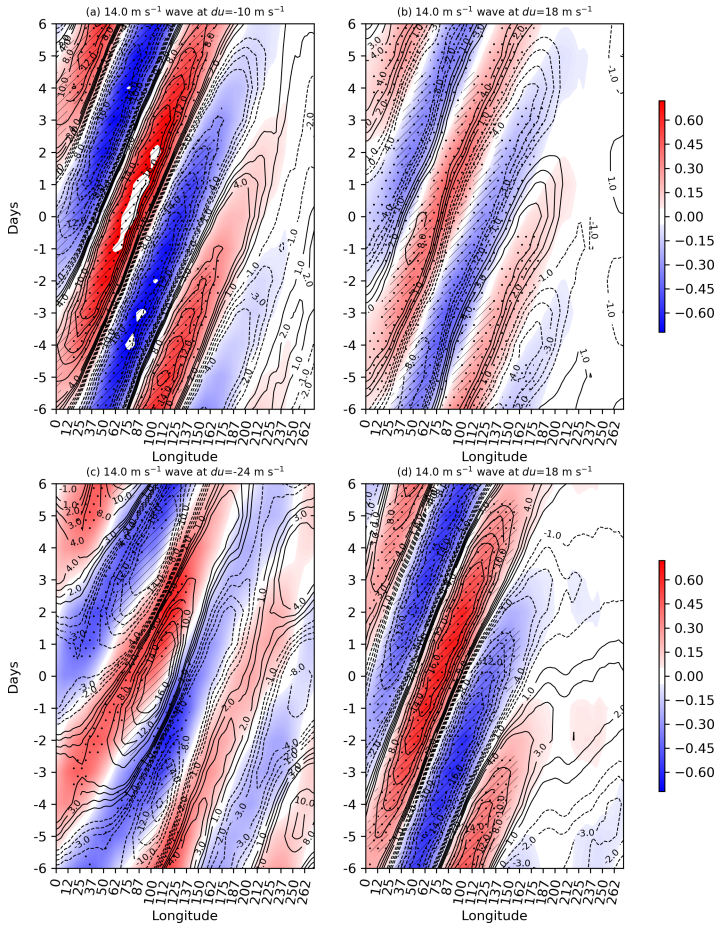

Figure 3.7: Regressed wind (shaded, interval of 0.1 m s^{-1}) and geopotential (contours, an interval of 1 m^2 s^{-1} when values between -4 and 4 m^2 s^{-1}, and an interval of 2 m^2 s^{-1} otherwise) at (a-b) 30 hPa on the 14 m s^{-1} Kelvin wave filtered at 30 hPa for (a) -10 m s^{-1} wind shear, and (b) 18 m s^{-1} wind shear based on the 30–50 hPa and at (c-d) 50 hPa on the 14 m s^{-1} Kelvin wave filtered at 50 hPa for (a) -24 m s^{-1} wind shear, and (b) 18 m s^{-1} wind shear based on the 30–50 hPa Dotes and hatching have the same meaning as in Fig. 3.4.

analysis with two indexes: the 30–50 hPa shear index, and the zonal mean zonal wind at 30 hPa. Hence, for the same vertical wind shear profile, we can compare the regressed pattern at continuum of quasi-Doppler shifted speeds. We found that the 14 m s^{-1} wavelet projects on the quadrature pattern under 18 m s^{-1} wind shear (see Fig. 3.7). Yet, would the 14 m s^{-1} wavelet projects on the Kelvin wave structure if 18 m s^{-1} shear profile did not include the critical layer? To test that, we revisit the regressed fields associated with the 14 m s^{-1} wavelet when the 30–50 hPa wind shear is 18 m s^{-1}, but at two different values of the quasi-Doppler shifted speed: 23 m s^{-1} (Fig. 3.8a) and 7 m s^{-1} (Fig. 3.8b). As expected,

Kelvin wave structure, however weak, prevails at 23 m s^{-1}, and a semi-quadrature structure exists at 7 m s^{-1}. Hence, according to the analyzed wavelets, the absence of the critical layer is necessary to observe Kelvin wave signals.

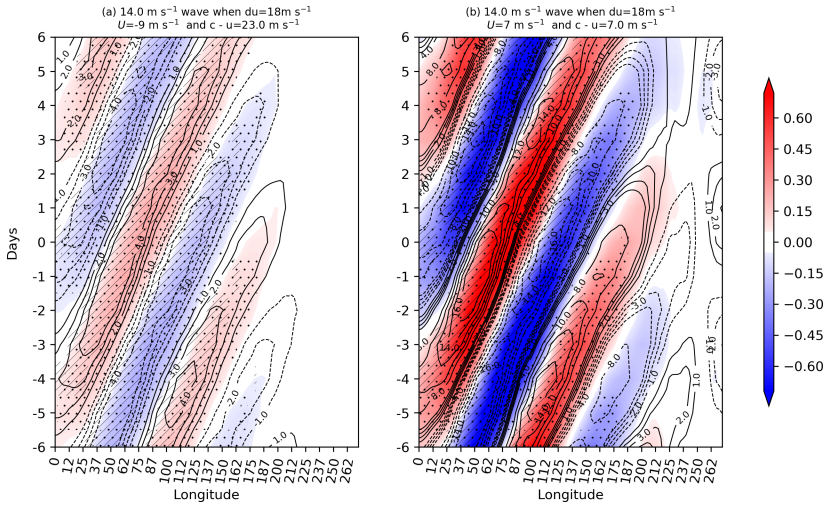

Figure 3.8: The same as Fig. 3.7, yet with targeting the wind and geopotential at the 50 hPa using the 14 m s^{-1} Kelvin wave filtered at 30 hPa for (a) -24 m s^{-1} wind shear, and (b) 18 m s^{-1} wind shear based on the 30-50 hPa. .

3.5 Dispersion Equation of the Kelvin Wave Under Shear.

Motivated by the regression analysis of the wave among shear layer, we derive a simple formula for the dispersion equation of the Kelvin wave under a vertical shear of the zonal wind. A primitive model on a beta plane linearized about the zonal mean flow with neither forcing nor dissipation is used following Andrews et al. [1987, see ch 3 and 4]. The beta plane approximation is widely used for studying the equatorially confined waves [Matsuno, 1966, Gill, 1980]. The model is the following:

$$u_t^{'} + \overline{u}u_x^{'} + \overline{u}_z w^{'} + \phi_x^{'} = 0 \tag{3.2a}$$

$$\beta y u^{'} + \phi_y^{'} = 0 \tag{3.2b}$$

$$\phi_z^{'} = H^{-1} R\theta^{'} e^{-kz/H} \tag{3.2c}$$

$$u_x^{'} + \rho_o^{-1}(\rho_o w^{'})_z = 0 \tag{3.2d}$$

$$\theta_t^{'} + \overline{u}\theta_x^{'} + \overline{\theta}_z w^{'} = 0 \tag{3.2e}$$

The variables $u^{'}, w^{'}$, ϕ, $\theta^{'}$ are the zonal wind, vertical wind, geopotential, and potential temperature deviations from the zonal means. The prime and overbar refer to the deviation of the zonal mean and the zonal mean. β is the beta parameter, or the meridional gradient of the Coriolis parameter at the equator, H is the scale height, $k \equiv \frac{R}{c_p}$, where R is the gas constant of the dry air and c_p specific heat at constant pressure. The first three equations represent the horizontal momentum equations and the hydrostatic equation. The last two equations represent the continuity equation and the thermodynamical equation. Note that z is the log-pressure height which, however close to the geometric height, simplifies the derivations [Holton and Hakim, 2012, Andrews et al., 1987]. Following Andrews et al. [1987], we use a solution of the following form to derive the dispersion equations:

$$\begin{pmatrix} u^{'} \\ w^{'} \\ \phi^{'} \\ \theta^{'} \end{pmatrix} = e^{z/2H} Re \begin{Bmatrix} \hat{u}(y) \\ \hat{w}(y) \\ \hat{\phi}(y) \\ \hat{\theta}(y) \end{Bmatrix} e^{i(kx+mz-\omega t)} \tag{3.3}$$

where k and m are the horizontal and vertical wavenumbers, and ω is the angular frequency. We present the dispersion equations in the following three scenarios:

1. No background wind $\overline{u} = 0$ (and hence no vertical shear $\overline{u}_z = 0$).
   From Eqs. (3.2a) and (3.2b), we get the geopotential amplitude $\hat{\phi}(y) = u_o \frac{\omega}{k} exp(-\frac{\beta k}{2\omega} y^2)$.
   From Eqs. (3.2c) and (3.2e), we get $(-i\omega)(\frac{1}{2H} + im)\phi^{'} + N^2\omega^{`} = 0$, thus after substituting the $\hat{\phi}(y)$, we can get $w^{'}$, which after plugged in the continuity equation Eq. (3.2d), we get $m^2 - \frac{i\sigma}{2H}m - \frac{1}{\sigma} = 0$, where $\sigma = (\frac{\omega}{kN})^2$. Hence $m_{1,2} = \frac{i\sigma}{4H} \pm \sqrt{\frac{-\sigma^2}{(4H)^2} + \frac{1}{\sigma}}$. Yet, after utilizing Boussinesq approximation, we get the traditional dispersion equation of the Kelvin wave
   $$\frac{\omega}{k} = -\frac{N}{m} \tag{3.4}$$
   where $m < 0$ for stratospheric Kelvin wave.

2. Constant background flow with no vertical shear $\overline{u}_z = 0$.
   The effect of the background flow is recovered when adding the advection terms $\overline{u}u^{'}_x$

and $\overline{u}\theta_x^{'}$. Hence, the dispersion equation under background zonal wind is

$$\frac{\omega}{k} - \overline{u} = -\frac{N}{m} \tag{3.5}$$

3. Background wind and vertical wind shear.

   By adding the $\overline{u}_z w^{'}$, we can get the dispersion equation under vertical shear of the zonal wind. By eliminating $\theta^{'}$ by combining Eqs. (3.2c) and (3.2e), we get

$$w^{'} = \frac{-(\phi_{zt}^{'} + \overline{u}\phi_{zx}^{'})}{N^2} \tag{3.6}$$

   Then, by substituting the value of $w^{'}$ in Eqs. (3.2a) and (3.2d), and getting eliminating $\phi^{'}$, we get

$$-\frac{(\omega - k\overline{u})i}{\frac{m\overline{u}_z}{N^2}(\omega - k\overline{u}) - ik} = \frac{kN^2}{m^2}\frac{1}{\omega - k\overline{u}} \tag{3.7}$$

   and after solving for the $\omega - k\overline{u}$, then we get

$$\omega - k\overline{u} = \frac{k\overline{u}_z}{2m}i \pm \frac{kN}{2m}\sqrt{4 - R_i^{-1}} \tag{3.8a}$$

$$\text{or} \quad \omega - k\overline{u} = \frac{k\overline{u}_z}{2m}i \pm \frac{k\overline{u}_z}{m}\sqrt{R_i - 0.25}, \text{ if} \quad \overline{u}_z \neq 0 \tag{3.8b}$$

   where R_i is the gradient Richardson number $R_i \equiv \dfrac{N^2}{\overline{u}_z^2}$.

In the absence of the vertical shear, the dispersion equation under shear (3.8a) reduces to $\omega - k\overline{u} = -\dfrac{kN}{m}$. The appearance of the Richardson number is not surprising, it indicates whether the instability caused by the shear is enough to overcome the static stability. The 0.25 in $\sqrt{R_i - 0.25}$ is the theoretical threshold distinguishing stable ($Ri > 0.25$) and unstable flow ($Ri < 0.25$). The internal gravity wave amplitude was found, by Booker and Bretherton [1967], to drop exponentially by $-2\pi\sqrt{R_i - 0.25}$ if critical level were encountered in a stable flow. The dispersion equation (3.8) enables us to analyze the variability of the phase speed of the Kelvin waves with the vertical wind shear (as enclosed in Ri). If R_i is less than 0.25, then Kelvin wave dissipates, and $\omega - k\overline{u}$ becomes imaginary, expressing the growth rate of the disturbance $\dfrac{k\overline{u}_z}{2m}\left[\dfrac{1}{2} \pm \sqrt{|R_i - 0.25|}\right]$, which varies proportionally with the wavelength. On the other hand, if R_i is larger than 0.25, then $\sqrt{R_i - 0.25}$ is real, and the frequency

becomes $\frac{k\overline{u}_z}{m}\sqrt{R_i - 0.25}$ and the growth rate reduces to $\frac{k\overline{u}_z}{2m}$.

Figure 3.9 shows the dispersion lines of the Kelvin wave with 4.5 Km vertical wavelength at different values of the R_i. The phase speed of the Kelvin waves increases with the increases of the R_i and achieves its maximum speed at the absence of the shear (when R_i reduces to infinity). The phase speed of the Kelvin wave increases from 14.9 to 16.8 m s^{-1} when R_i increases from 1 to 5, but it increases from 1.1 to 7 m s^{-1} when R_i just increases from 0.251 to 0.3. Hence, the phase speed of the Kelvin wave changes rapidly when the R_i is close to the threshold values 0.25. To help make sense of that, Fig. 3.10 presents the phase speed of the Kelvin wave as a function in R_i. The Kelvin wave achieves half its maximum speed (its speed in the absence of the shear) when R_i increases from 0.25 to 0.33, then it approaches 90% of maximum speed when R_i hits 1.32. Such rapid increases of the phase speed of the Kelvin waves with such small increases of the R_i motivates us to calculate R_i in the stratosphere. To do that we used the DYNAMO high resolution radiosonde observations launched at Addu atoll airport, Gan island, Maldives. We used high resolution radiosonde observations in order to calculate R_i at different vertical resolution. Figure 3.11 shows box-plots diagram of unfiltered R_i at the following vertical resolutions: 100, 600, 1100, 1600 m. The median and to a lesser extent the minimum value of the R_i increases with the vertical resolution of the data and it is larger than 1 at all resolutions. The threshold value (0.25) of the R_i is found in the lower quartile of R_i when the vertical resolution is 100 and 600 m. Hence, R_i calculated on fine vertical resolution could be associated with slower Kelvin wave than that associated with coarse grid. The same conclusion was also observed when analyzing the radiosonde data at different times.

The wavelet filtering and the varying-coefficient regression techniques served as a tool of precision that enabled us to appoint the targeted wave speed and simultaneously choose the surrounding background speed or vertical shear or both. Three patterns were observed while reducing the quasi-Doppler shifted speed by modifying the background wind. The first pattern is the classical Kelvin wave, which appears at high quasi-Doppler shifted speeds. Then, at a slower quasi-Doppler shifted speeds, we get the second pattern which resembles a quadrature relationship between the wind and the geopotential anomaly. For simplicity, we call the second pattern a "relaxed" Kelvin wave. The "relaxed" Kelvin wave was also found by Roundy [2017b] when analyzing the tropospheric Kelvin waves at different phase

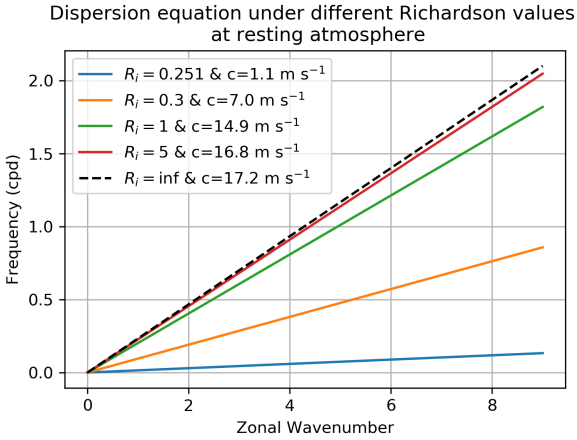

Figure 3.9: Dispersion equation as a function in the Richardson number for Kelvin wave with 4.5 Km vertical wavelength, and static stability is 0.0240 s^{-1}.

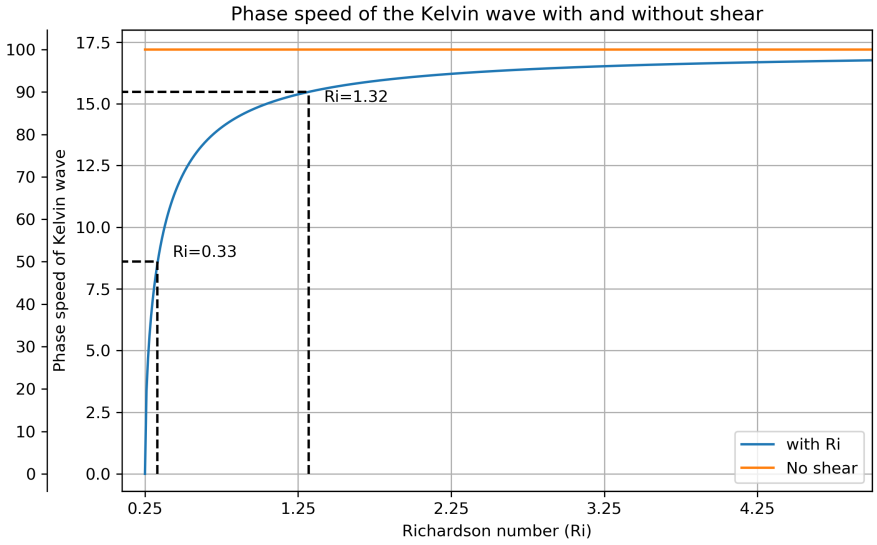

Figure 3.10: Phase speed of the Kelvin wave as a function in the Richardson number. The vertical wavelength of the Kelvin wave is 4.5 km, and static stability of 0.0240 s^{-1}. The orange line shows the speed of the Kelvin wave in the absence of vertical wind shear (recall Eq. (3.4)). The second y axes shows the percentage of the phase speed of the Kelvin waves with shear to that without shear.

speeds. This deviation of the slower waves from the traditional tropospheric Kelvin wave expresses the growing role of the convection. Yet, in the stratosphere, the wave dynamics rather than the moist dynamics is responsible for the appearance of the "relaxed" Kelvin wave. Lastly, when the quasi-Doppler shifted speed reduces to zero or negative values, we

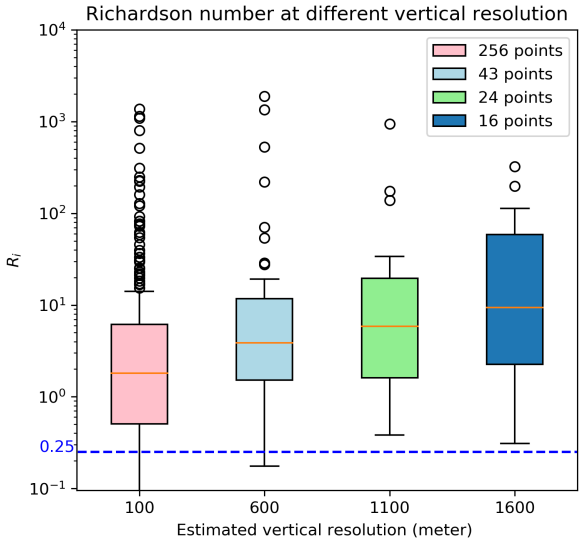

Figure 3.11: Gradient Richardson number calculated using high resolution radiosonde launched at June 22, 2011, at Addu Atoll airport, Gan Island, Maldives, during DYNAMO field campaign. The observations are from 199.9 hPa to 5.6 hPa (where the balloon burst). The vertical resolutions are the grid size used to calculate static stability, and vertical shear of the zonal and meridional wind. The circles above the whiskers are the outliers. The red line inside the boxes refer to the median. The legend indicates that the number of the points found at the corresponding vertical resolution.

get the third pattern, which is the well known Gill structure Gill [1980]. The Gill pattern is a forced response, on the contrary to the Kelvin wave, which could be a forced response or free mode [Hendon and Salby, 1994]. The transition of the Kelvin wave to the "relaxed" Kelvin structure, and finally to the Gill pattern reflects the existence of varying frequency sources that originate from the variation of the background wind in the stratosphere rather than being a direct projection of the tropospheric sources. In other words, a continuum of background speeds might act as a source of frequencies. Although the reduction of the quasi-Doppler shifted speed is, in essence, responsible for the observed patterns, other factors, that are outside the scope of this study, might also play a role like the Newtonian cooling or Rayleigh damping or both.

We found that the "relaxed" Kelvin wave appears before approaching the critical layer. Hence, it is intuitive to differentiate between what we suggest the "observed critical layer" and the "theoretical critical layer." We define the "observed critical layer" as the layer in

which the wave structure begins to fade away, and the "theoretical critical layer" as the layer in which the quasi-Doppler shifted speed reduces to zero. The quasi-Doppler shifted speed associated with the "observed critical layer" is faster than that associated with the "theoretical critical layer". Such definition, however simple, has a critical implication on our understanding of the eddy-background flow interaction. Traditionally, a comparison between the wave phase speed and the background wind speed was enough to decide if such eddy can transfer momentum to the mean flow, which might be misleading. Actually, waves that are a few meters per seconds faster than the background flow still might be absorbed by the mean flow. This behavior was also observed by Randel and Held [1991] when studying the absorption of meridional transient tropospheric eddies. The difference between the "theoretical critical layer" and the "observed critical layer" is the dissipation factors like the Newtonian cooling and Rayleigh friction that are implicitly taken into account in the "observed critical layer."

We found that Kelvin wave could be absorbed at 30 hPa during 30-50 hPa westerly shear. This absorption is responsible for the descent of the westerlies with time, which is a well known mechanism for the formation of the westerly phase of the QBO [plumb, 1981]. We found also that the Kelvin wave could be absorbed at 50 hPa during the 30-50 hPa easterly shear. Yet, such absorption cannot force the easterly shear to descend because Kelvin wave can propagate through westward flow without absorption, and the descending of the easterly shear occurs with the bombardment of westward-moving waves like the tropical Rossby wave or mixed Rossby gravity wave. Absorption of the Kelvin wave at the base of the easterly shear layer might be associated with the fluctuation of the tropopause near 100 hPa [Ryu et al., 2008]. By using a multiple linear regression against the vertical shear and background wind, we found that Kelvin wave is apparently absorbed if the critical layer were met irrespective of the shear. That result is consistent with the early findings of Holton and Lindzen's work.

The reason behind revisiting the dispersion equation is to get more insight into the effect of the vertical wind shear on the phase speed of the Kelvin wave. Although several studies focused on propagation of the Kelvin waves under vertical shear [e.g., Holton, 1970, Lindzen, 1971, 1972, Plumb and Bell, 1982], the variability of the dispersion properties with Richardson number, surprisingly, has not gain much attention. We found that under a

very large Richardson number, the dispersion equation under shear reduces to the classical dispersion equation without shear. On the other hand, if the Richardson number lies between 0.25 and 1, the phase speed of the Kelvin wave decreases sharply. In most theoretical studies back in the 1970 and 1980s, Richardson number has been assumed to be very large, a consequence of the lack of observations with a high vertical resolution in the stratosphere. We found that Richardson number decreases when using observations with fine resolution in the vertical, which add uncertainties when using the dispersion equation under vertical shear. Although Kelvin wave is considered a large-scale circulation, the actual absorption of Kelvin wave occurs in thin vertical layer. Based on our analysis of Kelvin wave, we did not observe a change in the horizontal phase speed at different vertical shear near the base point of the wavelet index.

CHAPTER 4

On the MJO Phase Speed Among Different Background Moisture and Zonal Wind Base States.

4.1 abstract

The variability of the phase speed of the Madden Julian oscillation (MJO) is poorly understood, due to the unsettled dynamics of the MJO. The authors present a simple pathway to relate the phase speed of the convective signal of the MJO with the background states over the Indian Ocean, using the ECWMF reanalysis. Results show that fast MJO events are associated with wetter background states over East Africa and the Indian Ocean, whereas slow MJO is associated with dry background states. Relaxation of the coupling between the convective MJO and its circulation has been previously linked to faster propagation of MJO circulation signals east of the Dateline. Yet, results show that fast MJO exhibits strong active and inactive phases with structure suggesting more hierarchical convection. Results support that moisture mode dynamics may be relevant to the amplitude of the MJO, but its eastward phase speed may be higher during periods of enhanced low-level moisture because these periods have anomalously weak upper tropospheric easterly background wind.

Keywords — MJO, phase speed, background state, moisture mode.

4.2 Introduction

The Madden Julian oscillation [MJO Zhang, 2005] is the dominant intraseasonal mode in the tropics. Although there is no consensus among the tropical community on its dynamics or how to best trace its signal [Straub, 2013], the MJO could be described as a cluster of convection coupled with large-scale atmospheric circulation moving eastward with an average speed of 5 m s^{-1} over the warm pool, then the large-scale circulation accelerates eastward over the Eastern Pacific, where coupling to convection is much weaker [Salby and Hendon, 1994, Bantzer and Wallace, 1996].

Different theories have been introduced to explain the slowness of the MJO over the

Indian Ocean when compared to faster tropical waves. The distinction among those theories reflects, in essence, the variety of dynamics proposed to explain the MJO. The suggestion that MJO is a slow Kelvin wave has been well theorized [e.g. Chang and Lim, 1988, and many others]. This avenue retains some esteem, as it is supported by recent observations; for example, MJO-similar structure arose when targeting slow signals that follow the dispersion properties of the Kelvin waves [Roundy, 2012, 2014, 2019].

Aside from the wave perspective of the MJO, moisture or moist static energy arose as a primary variable to attempt to understand the physics of the MJO. For instance, fluctuations of the moist static energy has been found to be in phase with precipitation, not only on the intraseasonal scale, but also on the background and synoptic scales [Inoue and Back, 2015]. The moist static energy, which is a quasi-conserved quantity in moist processes, gained its importance over tracers that focus on moisture specifically, by accounting for temperature (sensible heat) along with the moisture (latent heat). Zhao et al. [2013], Li et al. [2015], and Zhu and Hendon [2015] found that the initiation of the MJO is preceded by the advection of background moisture by the zonal wind associated with the previous MJO. Jiang et al. [2018] found that horizontal advection of background moisture by the MJO flow is essential also for the northward propagation of the MJO during northern summer. Moreover, Stachnik et al. [2015] found that the termination of MJO convection is preceded by negative anomalies of moisture over equatorial Indian Ocean. Analysis of the moist static energy budget has suggested several potential mechanisms that might maintain and propagate the MJO. In an aqua-planet model, Andersen and Kuang [2012] found that the tendency of the moist static energy is in phase with the horizontal advection of the background moisture by the MJO flow, suggesting that horizontal advection may contribute to the eastward propagation of the MJO. The same results have been replicated by Hsu and Li [2012] using ECWMF Reanalysis ERA-40, and by Sobel et al. [2014] using data from the Dynamics of the MJO (DYNAMO) field program. Moreover, Wang et al. [2017] and Kim [2017] compared the MSE structure in models associated with propagating versus non-propagating MJO signals. Their distinction between propagating and non propagating MJO is based on total-field subseasonal signals, so it is possible that MJO-events deemed non propagating emerge from the interference pattern generated by superposition between MJO and equatorial Rossby wave signals and thus still include propagating MJO signals. They found that the MSE is in quadrature with the MSE tendency in the models with propagating MJO, while the MSE is in phase with the

MSE tendency in the models with non-propagating MJO. Using aqua-planet simulations, Xianan et al. [2020] found that the simulated intraseasonal oscillation propagates westward if a prescribed uniform SST (which produces an off-equatorial peak in moisture) is used instead of SST gradients (which produces a peak of moisture at the equator). It is unclear the extent to which the mechanisms in subseasonal variability in these models conform to the mechanisms in observations, including the different factors in models and observations that determine the time mean balance between eastward and westward-moving intraseasonal modes.

The proposed essential role of the advection of background moisture by the MJO wind for the initiation and termination of MJO convection, the propagation versus the stalling of the MJO, and the eastward versus the westward propagation of proposed simple model MJO-like disturbances implicitly indicates that the background moisture or MSE could modulate the MJO phase speed. This paper analyzes the association between background moisture and the phase speed of the MJO. Previous work on moisture mode theory has suggested relationships between the phase speed of the MJO and moisture gradients. Other works have suggested that increased convective activity, increased moisture, and increased precipitation rates are associated with slower MJO signals. Hence, we analyze the variability of the MJO phase speed with different states of the background moisture at different locations over the Indian Ocean and Eastern Africa. Section 4.4 discusses the filtering technique used to filter the data for the MJO band, and the regression technique used to isolate the structure of the MJO at different levels of background moisture. The variability of the MJO phase speed with background moisture is presented in section 4.4.4. The vertical structure of the MJO associated with different phase speeds is discussed in section 4.4.6. Finally, in section 4.4.5, we show the background flow states associated with the fast and slow MJO. Results will investigate to what extent moisture and the background flow are associated with the MJO as a function of its phase speed. A subsequent paper will discuss a similar analysis of the relationship between zonal and meridional gradients of moisture and MJO phase speed.

4.3 Data

Zonal wind and specific humidity data were obtained from the daily ECMWF Interim Reanalysis [ERA-I, Dee et al., 2011] on 2.5°x2.5° grid and 32 vertical pressure levels, from

1979 to 2016, extending from 180°E to 180°W and from 20°S to 20°N. The ERA-I moisture dataset incorporates SSM/I satellite data [Trenberth et al., 2011], making it suitable for analyzing the moisture field over Indian Ocean. The daily grided NOAA outgoing longwave radiation (OLR) dataset was obtained for the period 1979 to 2016 on a 2.5°x2.5° grid [Liebmann and Smith, 1996].

4.4 Methods

4.4.1 Spatial-temporal data filtering.

We used the discrete Fourier transformation (DFT) to extract the intraseasonal component of the ERA-I zonal wind, geopotential height, and specific humidity. Although this Fourier filtering technique guarantees a sharp frequency cutoff, it produces lobes at the edges (known as the Gibbs phenomenon), which might be partially mitigated by, for example, not using data near the beginning and end of the filtered dataset. The filtered dataset spans from 1980 to 2016. To distinguish the MJO from the bulk of the intraseasonal modes that also include westward-moving signals [Wang and Rui, 1990], we implement a spatial-temporal box filter to retain the only eastward-propagating components by selecting wavenumbers 1 - 10 and the Fourier harmonics 20 - 90 day range using two dimensional DFT following Kiladis et al. [2005], Straub [2013] and many others, yet with a slightly different wavenumber-frequency band of frequencies or wavenumbers or both. Besides the intraseasonal components, we estimate the background states by lowpass filtering data for periods larger than 90 days, retaining the longerm mean and seasonal cycle as well as interannual and longer term variability.

Several indexes have been used to trace and quantify MJO convective signal or large-scale circulation or both [Straub, 2013]. It is more convenient to use an MJO index that traces the MJO convective signal when analyzing the relationship between the background moisture and convective-MJO. We followed the technique of Zhao et al. [2013], who constructed an MJO index using only OLR data to analyze the convective initiation of the MJO. The covariance matrix of the 20 - 90 day filtered OLR anomalies confined between 40°E to 180°E and 30°S to 30°N was constructed by first rearranging the data from a three dimensional array (time, latitude, longitude) into a two dimensional array (time, latitude * longitude), then multiplying the two dimensional array with its transpose to get new array with dimension

(latitude * longitude, latitude * longitude). All analysis is based on the winter MJO from November to April, when MJO is known to peak Zhang and Dong [2004]. The result gives the covariance matrix of the data. The principal component time series were found by projecting the filtered OLR anomalies onto the EOF patterns, which are the eigenvectors of this matrix. We used the first principle component (PC1) as a predictor in the regression models to analyze the structure of the MJO. PC1 was scaled by dividing by its standard deviation.

PC1 is used as base index for the regression and composite analysis. Regression analysis senses only the time scales associated with the PC1. Variables other than the OLR data may be associated with horizontal scales that extend outside the filtered wavenumbers when regressed against PC1. Those scales would appear in the regression maps. The horizontal scales of the filtered OLR associated with PC1 are not necessarily the same among the other filtered variables. Those unseen scales might result in underestimation or overestimation of the speed of the MJO in the non-OLR filtered variables.

4.4.2 The varying-coefficients regression technique.

Roundy [2017a] developed a new regression technique that provides a continuum of regression coefficients that vary continuously across the seasonal cycle. The algorithm uses Fourier regression to predict how the variance of the predictor and the covariance between the predictor and the predictand vary with the seasonal cycle, then it takes the ratio of these quantities on a given day of the year to estimate the regression slope coefficient most likely to apply on that day. Interestingly, a revision of the same technique can be used to find regression coefficients that fluctuate with any slowly varying signal, instead of the seasonal cycle, that happens to correlate with both the variance and the covariance quantities used to calculate regression slope coefficients. The varying regression technique [Roundy, 2017a] is superior to the partial regression technique [Yule, 1907], used to find the correlation between two variables while excluding their linear fluctuation with other (third) variable that might impact the correlation value, in the sense that we see the impact of the continuum variation of third variable on the regression coefficient instead of just holding it constant. The partial regression technique is frequently used to exclude the effect of the ENSO from the Indian Ocean dipole and vise versa [Cai et al., 2011]. In this study, we use the varying regression

coefficients technique to analyze the structure and the speed of the MJO in different background moisture states, which is of an essence to the initiation and the propagation of the MJO (see sec. 4.2). A time lag regression model of the evolving MJO structure is achieved by regressing fields of data against a predictor MJO index x. Let y represent a particular dependent variable at some grid point and time lag. Our objective is to find the regression slope coefficient relating x and y in the context of another variable, such as background moisture. The technique is as follows: (1) regress the square of the MJO index x^2, on the slowly evolving signal (background moisture). The regressed values might be understood as the regressed variance of the predictor; (2) regress the product of the MJO index with the times series of the dynamics field that we are interested to analyze against the background moisture. Similarly as in step 1, the output could be understood as the regressed covariance. This dynamical field serves as the regressed variable, (3) substituting the value, that we are in interested in, of the background moisture in (2) and (1) to find the predicted covariance and the predicted variance, where their ratio is the regression coefficient associated with the prescribed value of the background moisture.

4.4.3 Statistical test.

We used the students t-test to test the statistical significance of the traditional regressions and composites. Yet implementing a parametric statistical test is challenging when considering the varying-coefficients regression that includes multiple regressions Roundy [2017a]. Hence, we used a bootstrap test following Roundy [2017a] to study the statistical significance of the varying-coefficients regression. In the context of the bootstrap test, it can be easier to describe the significance test in terms of the confidence interval rather than as a hypotheses test. To implement the test, the regression coefficients are calculated 10,000 times based on random samples from the original data, with samples taken with replacement [see ch. 5 Wilks, 2011, for details on the bootstrap technique]. Those coefficients constitute the population distribution with similar autocorrelation characteristics. To test the significance of the regression coefficient against, for example, the 90% level, we check if the calculated regression coefficient is confined between the population confidence interval, which is between 500 and 9,500 quantiles.

4.4.4 MJO phase speed among varying background moisture states.

To get better idea on the structure of the MJO that is associated with PC1 index (defined in section 4.4), we present lead-lag regression Hovmöller of the filtered zonal wind at 850 and 200 hPa (Figs. 4.1a and b), and specific humidity at 850 hPa (Fig. 4.1c). At 850 hPa, over the Indian Ocean, westerly anomalies are located to the west of the negative OLR anomalies, with easterly anomalies to the east. The reverse occurs at 200 hPa, consistent with the known vertical structure of the MJO that maps roughly onto the first baroclinic mode [Rui and Wang, 1990, and others] that resembles an overturning circulation. At day zero, specific humidity at 850 hPa peaks over the Indian Ocean, while negative values cover most of the Pacific Ocean (Fig. 4.1c). Those structures are similar to the MJO structure between phases 2 and 3 of the real-time multivariate MJO (RMM) index [Wheeler and Hendon, 2004], where the MJO convection lies over the Central Indian Ocean. The relationship between the zonal wind and the MJO convective center over the Pacific Ocean is different from that over the Indian Ocean [Zhang and Anderson, 2003]. Over the Indian ocean, the specific humidity is in quadrature with the 850 hPa zonal wind (Figs. 4.1a and c), and in phase with the MJO convection center. This intraseasonal moisture anomaly might be important for maintaining the MJO convective activity, yet the initiation and the propagation of the MJO itself have been hypothesized to be supported by the advection of the background moisture, rather than the intraseasonal moisture, by the lower tropospheric easterly zonal wind associated with the previous MJO event [Zhao et al., 2013, Straub, 2013].

The phase speed of the MJO as represented by the regressed zonal wind anomaly at 850 hPa is roughly 5.6 m s^{-1} (see reference line on Fig. 4.1a). The reference lines that mark the phase speed of the contours, subjectively fit the peak contours between -5 and 5 days. The phase speed of zonal wind at 200 hPa is a little faster (Fig. 4.1b). The abrupt acceleration of the MJO signal, represented by the upper and lower layer zonal wind and specific humidity (Figs. 4.1a-c), near the dateline has been understood as a result of the separation between the circulation and convection that were coupled over the Indian Ocean [Salby and Hendon, 1994, and many others].

To study the variability of the MJO phase speed with the background moisture, we reproduce the previous lagged regression Hovmöllers, but at specific values of background moisture using the varying regression coefficient that we discussed in section 4.4. In order to

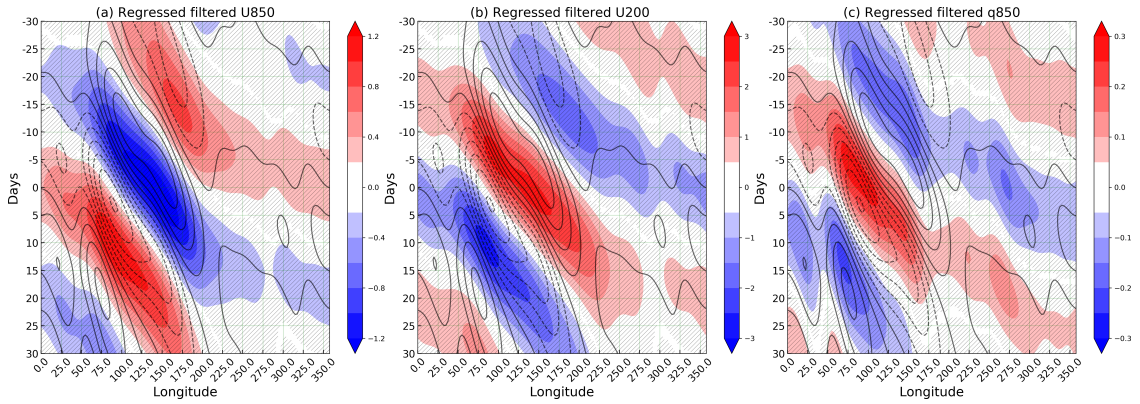

Figure 4.1: Lagged regression of (a) 20 - 90 days eastward filtered zonal wind at 850 hPa, shaded at an interval of 0.2 m s^{-1} , (b) 20 - 90 days eastward filtered zonal wind at 200 hPa, shaded at an interval of 0.5 m s^{-1}, (c) 20 - 90 days eastward filtered specific humidity at 850 hPa, shaded at an interval of 0.05 g kg^{-1}. All those variables were regressed against PC1 (see text for more information about the PC1). Hatched areas are statistically significantly different from zero above the 90% level based on resampling 10,000 sample utilizing bootstrap statistical test.

implement varying coefficient regression, we construct background moisture indexes. Figure 4.2 show box-plots of the background moisture over different regions proximate to the Indian Ocean. For the most part, the minimum, median, and maximum values of the background moisture increase from Eastern Africa to the Maritime continent, consistent with the eastward gradient of the climatological moisture over the Indian Ocean, while the total variance decreases eastward. In this paper, we focus on the MJO phase speed associated with the background moisture fluctuation over Eastern Africa. We also analyze the variability of the MJO phase speed with background moisture over the western Indian Ocean, Eastern Indian Ocean, and the Maritime Continent regions as half of MJO convective events were reported to initiate over the Eastern Indian Ocean and Western Pacific Matthews [2008], Straub [2013].

Figure 4.3 presents varying coefficient lag-regressions of the filtered zonal wind at 850 hPa when the background moisture over Eastern Africa is 7 g kg^{-1}, 9 g kg^{-1}, and 11 g kg^{-1}. We choose those values because they are close to the minimum, median, and maximum values of the background moisture (see Fig. 4.2), thus reflecting the phase speed of the MJO across the range of background moisture. The phase speeds of the MJO, as represented by the filtered 850 hPa zonal wind, when the 850 hPa background moisture is 7 and 11 g

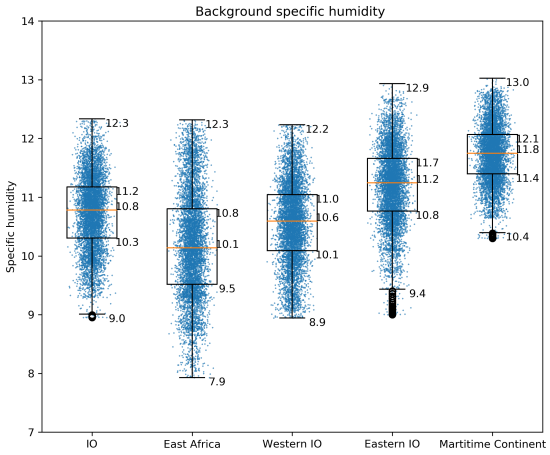

Figure 4.2: Box-plots of the background (¿ 90 days) specific humidity over different locations over the Indian Ocean, superimposed on scatter plots of the same variable that is spread horizontally using random function in order to get an idea on the density of the background specific humidity at each value. The background specific humidity is averaged over the Indian Ocean basin (10°S - 10°N, 50°E - 90°E), East Africa (10°S - 10°N, 35°E - 55°E), Western Indian Ocean (10°S - 10°N, 55°E - 72.5°E), Eastern Indian Ocean (10°S - 10°N, 72.5°E - 90°E), and Maritime-continent (10°S - 10°N, 90°E - 107.5°E). The lower, middle, and upper sides of the box-plot represent the first, second (median), third quarterlies, where the lower and upper fences represent the minimum and maximum values, and circles represent outliers.

kg^{-1} are 4.28 and 6.43 m s^{-1} (Fig. 4.4a and c), suggesting that the phase speed of the MJO increases with the moisture content at 850 hPa. The phase speed of the MJO using traditional linear regression (Fig. 4.1a), which is 5.6 m s^{-1}, lies between the upper and lower limit of the MJO phase speed found at 7 and 11 g kg^{-1} (Fig. 4.4a and c), indicating that the traditional regression expresses the weighted mean phase speeds across the population of background moisture states. The spatial structure of the MJO varies with its speed as slow MJO (Fig. 4.3a) extends horizontally more than fast MJO (Fig. 4.3c). We reproduced Fig. 4.3 using background moisture over the Western Indian Ocean, Eastern Indian Ocean, and Maritime Continent, and we found that the phase speed of the MJO also increases with moisture (not shown), consistent with the results we found using background moisture over Eastern Africa. We extend this analysis by presenting the lagged zonal wind over 200 hPa associated with the background moisture over Eastern Africa, as shown in Fig. 4.4. Inclusion of the wind data is important because the upper tropospheric wind might influence the MJO phase speed by advection, but it might also be associated with changes in lower tropospheric

humidity. For example, strong upper tropospheric westerly anomalies over the equatorial Indian Ocean tend to occur with lower tropospheric easterly anomalies, which may increase the low level moisture over the western Indian Ocean. The phase speed of the zonal wind at 200 hPa increases with the background moisture, but with slower rate than that of the zonal wind at 850 hPa. We produced the same figure using background moisture over the Western Indian Ocean, Eastern Indian Ocean, Maritime Continent, and we found that the increases of the phase speed with background moisture are largest when using background moisture over the Maritime Continent. Besides the observed increases of the phase speed of the filtered zonal wind with the background moisture, the amplitude of the filtered zonal wind intensifies, reflecting a stronger MJO signal in the variable (Fig. 4.4).

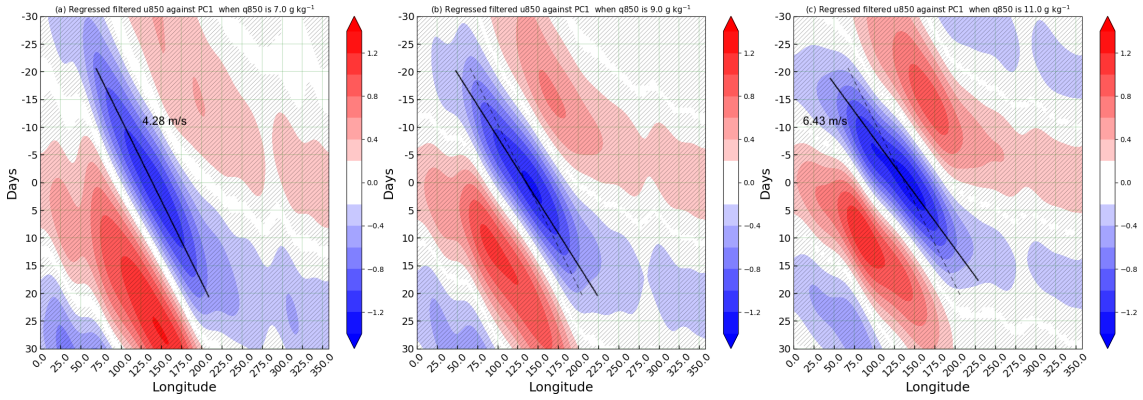

Figure 4.3: Lagged regression of 20 - 90 days eastward filtered zonal wind at 850 hPa on PC1 when the background moisture over Eastern Africa is (a) 7 g kg^{-1}, (b) 9 g kg^{-1}, (c) 11 g kg^{-1}. Shading is in interval of 0.2 m s^{-1}. Hatching indicates that the field is statistically significant from zero above the 90% level using a bootstrap statistical test. The solid reference lines approximate the phase speed of the contours lines peak between -5 and 5 days. The dashed reference lines in panel b and c are the reference solid line shown in panel a.

In order to verify the results produced by the method of varying regression slope coefficients, we present composite Hovmöller that show the MJO phase speed as expressed by the 850 hPa filtered zonal wind at low and high 850 hPa background moisture as shown in Fig. 4.5. We composite around the days when time in PC1 exceed 1 standard deviation simultaneous with background moisture values in its lowest quartile (Q1), which includes also the outliers. We repeat the process for background moisture values in their highest quartile (Q2), Figure 4.5b. Our choice of selecting days associated with 1STD of PC1 and Q1 or Q2 is arbitrary, but is the most common in the literature. A drawback of the composite analysis

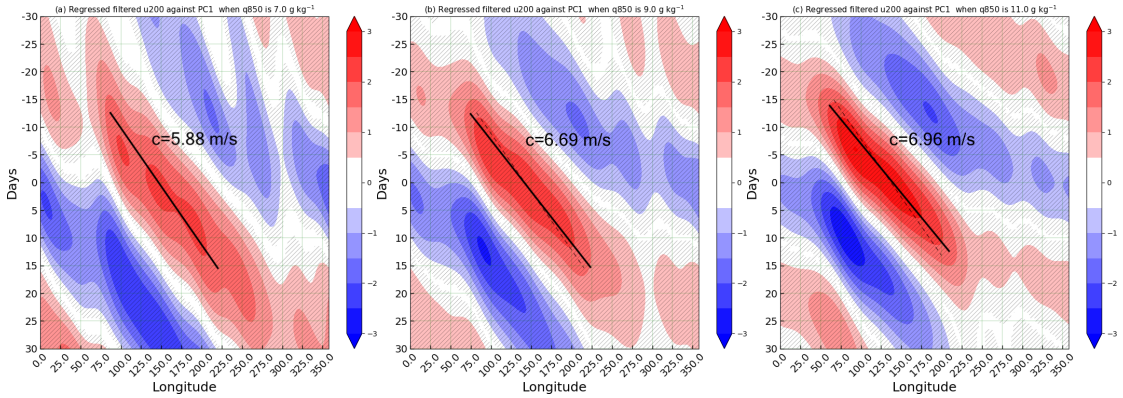

Figure 4.4: The same Lagged regression in Fig. 4.3, except for the zonal wind at 200 hPa instead of zonal wind at 850 hPa.

when compared to the varying regression method is that we cannot find a clear structure at a specific value of the background moisture because a composite requires a population of events over which to average, but few events land at a particular value, making us unable to assess statistical stability. Figure 4.5 shows that the phase speeds of the filtered 850 hPa zonal wind at low and high moisture are 4.8 and 6.6 m s^{-1} consistent with the previous results.

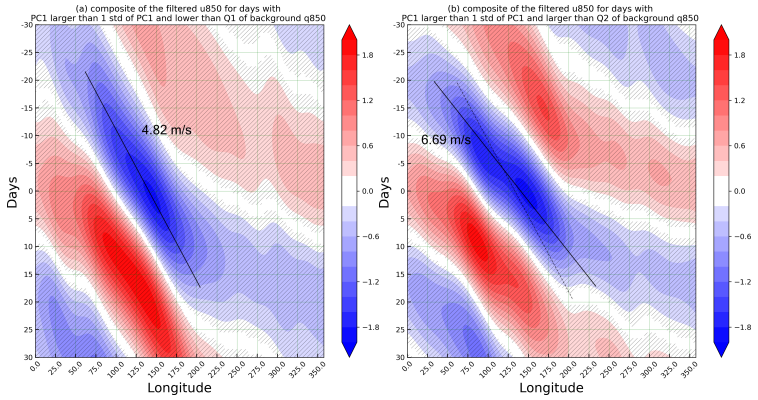

Figure 4.5: Composites of the filtered zonal wind at 850 hPa for days with (a) PC1 larger than 1STD of PC1 and lower than Q1 of the 850 hPa background moisture, (b) PC1 larger than 1STD of PC1 and larger than Q2 of the 850 hPa background moisture. Shading is in interval of 0.2 m s^{-1}. Hatching indicates that the underling shading is statistically significantly different from zero at the 90% level using t-test analysis.

4.4.5 Background states associated with the MJO

To better inform our understanding of the association between the background moisture and the acceleration of the MJO over the Indian Ocean, we present the relationship between the background moisture over Eastern Africa and the background zonal wind. Background zonal wind could advect the MJO, and comparable magnitude of the background zonal wind and MJO zonal wind might lead to nonlinear advection. The background wind might also associate with different background moisture states, so that it is possible that an association attributed to moisture could actually be explained by wind. Figure 4.6 shows the regressed background zonal wind against the the background specific humidity over Eastern Africa. The upper level circulation shown in Fig. 4.6 is in agreement with the the upper level circulation during El Niño and positive Indian Ocean dipole, reflecting weakening of the Walker circulation during Fall and spring associated with wet years over western Indian Ocean and Eastern Africa Shaaban and Roundy [2017]. Figure 4.6 was reproduced again but using background moisture over the western Indian Ocean, Eastern Indian Ocean, and Maritime Continent. We anticipated that the circulation pattern associated with the background moisture over the Maritime Continent would resemble a pattern opposite to that shown in Fig. 4.6, yet, surprisingly, we got circulations (not shown) that also matches El Niño and positive Indian Ocean dipole. Presumably suggesting the subsidence over the Maritime Continent raises the background moisture at the lower levels.

4.4.6 The vertical structure of the MJO associated with different background moisture states.

Figure 4.7 presents the vertical structure of the zonal wind associated with PC1 when the background moisture is 7 g kg^{-1} and 12 g kg^{-1}, following the method of varying regression slope coefficients. The vertical structure of the zonal wind is stacked, where a positive anomaly field lies above a negative anomaly field or vice versa. The stacked structure is usually observed over the Indian Ocean, in contrast to the tilted structure, where tilted positive or negative signed anomalies extend across the vertical column, which is usually observed over the Maritime continent and the Pacific Ocean Sperber [2003], Kiladis et al. [2005]. At first glance, the two signed stacked structure of the zonal wind (Fig. 4.7) suggests a structure consistent with the first baroclinic mode. Yet, the intensification of the zonal

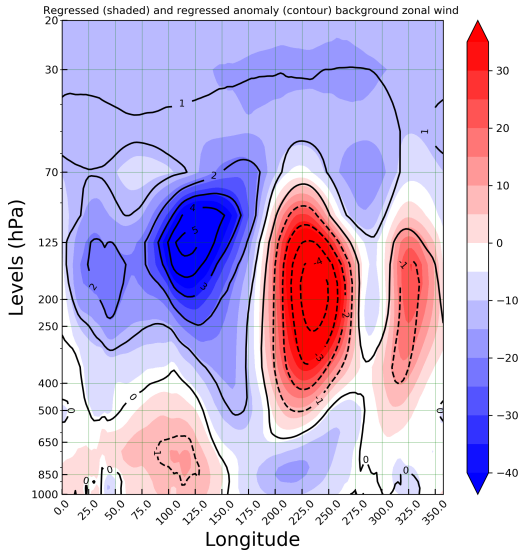

Figure 4.6: Longitude-level maps of regressed background (shaded) and regressed background anomaly (contoured) of the zonal wind averaged between -10° and 10° against background specific humidity index over East Africa at 850 hPa. Shading is contoured every 0.1 g kg^{-1}. Hatched contours are statistically significant from zero above the 90% level using statistical t-test.

wind with height suggests that more baroclinic modes would be needed to account for either the intensified zonal wind above 500 hPa or the lessening of the zonal wind below 500 hPa structure Rui and Wang [1990]. On the other hand, the Kelvin wave part of the MJO could be understood as radiative wave, instead of a superposition between the baroclinic modes. Hence, the vertical structure of the MJO could be described in terms of radiative waves to the extent that Kelvin wave dynamics explain its structure Roundy [2019]. At 7 g kg^{-1} (Fig. 4.7a), the westward tilt of the zonal wind in the troposphere and the eastward tilt in the stratosphere suggest structure similar to the radiative structure of the Kelvin wave, with upward-energy transfer in the stratosphere and downward-energy in the troposphere [Shaaban and Roundy, 2021b]. The vertical structure of the filtered zonal wind when the background moisture is 7 g kg^{-1} (Fig. 4.7a) is less stacked than that at 12 g kg^{-1} (Fig. 4.7b). Moreover, the upper level westerlies at 12 g kg^{-1} (Fig. 4.7b) are stronger than at 7 g kg^{-1} (Fig. 4.7a) over Eastern Africa and also over Maritime Continent (not shown), expressing stronger upper air outflow that might result from intensification of the convection.

Figure 4.8 shows an eastward 20 - 90 day filtered specific humidity associated with the 7 g kg^{-1} (Fig. 4.8a) and 12 g kg^{-1} (Fig. 4.8b) background moisture over Eastern Africa.

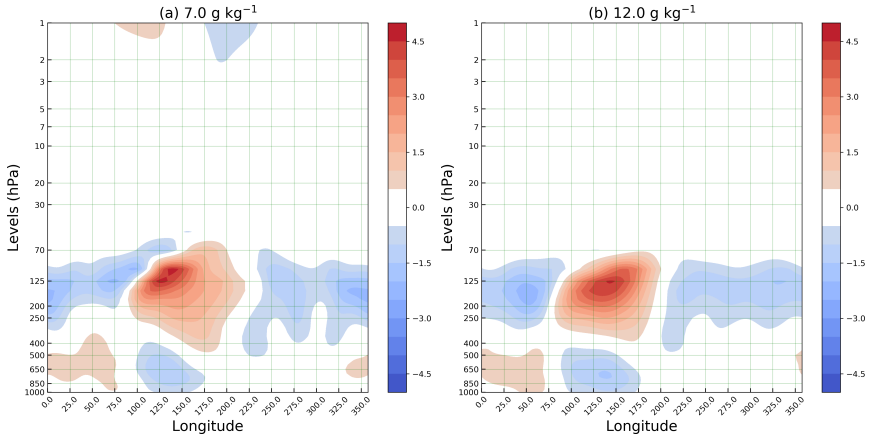

Figure 4.7: Longitude-level maps of regressed eastward 20 - 90 days filtered zonal wind against PC1 when the 850 hPa background moisture is (a) 7 g kg^{-1}, (b) 12 g kg^{-1}. Shading is contoured every 0.4 m s^{-1}. Hatched contours are statistically significant different from zero above the 90% level using the bootstrap test.

The amplitude of the intraseasonal filtered specific humidity is far less than the background specific humidity when compared to the ratio of the intraseasonal and the background zonal wind. The filtered specific humidity field shows a moist column over the Indian from surface to 300 hPa, consistent with the active convective phase of the MJO, and dry column over Western Pacific, consistent with the suppressed phase (Fig. 4.8). The intraseasonal specific humidity field associated with a high background moisture (12 g kg^{-1}) resembles wave number one, while it resembles wavenumber two at low background moisture (7 g kg^{-1}). The active phase over Indian Ocean at 12 g kg^{-1} is wetter than that at 7 g kg^{-1}, also the suppressed phase over Western Pacific at 12 g kg^{-1} is drier that that at 7 g kg^{-1}. The active phase at 12 g kg^{-1} in the lower layer shows a bulging structure that might be associated with shallow convection that precedes the MJO deep convection signal [Benedict and Randall, 2007, and others]. Analyzing the asymmetry between the active and the inactive phases, at 7 g kg^{-1} or 12 g kg^{-1} associated with the PC indexes is not conclusive since a negative sign of the PC is also valid from a statistical point of view, leading to sign-swap between active and inactive phases in the regression analysis. Any asymmetry or non-linearity between the positive and negative phases cannot be deduced from regression analysis.

This study uses a novel regression technique to address the fluctuation of the MJO phase speed with low-level background moisture over Eastern Africa and the Indian Ocean. The lagged regressions of the MJO as represented by the upper and lower level zonal wind and

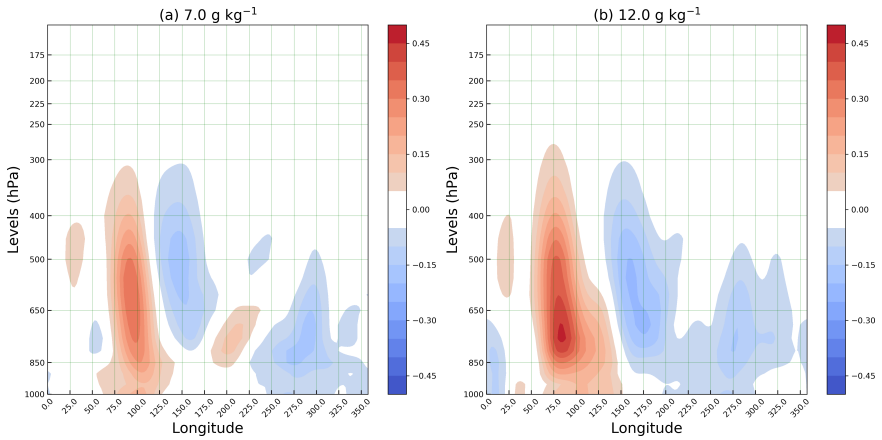

Figure 4.8: Longitude-level maps of regressed eastward 20 - 90 days filtered specific humidity against PC1 when the 850 hPa background moisture over Eastern Africa is (a) 7 g kg^{-1}, (b) 12 g kg^{-1}. Shading is contoured every 0.4 m s^{-1}. Hatched contours are statistically significant from zero above the 90% level using bootstrap statistical test.

moisture show an increase of the MJO phase speed with increases of the low-level background moisture over Eastern Africa and Indian Ocean (Fig. 4.3 and 4.4). On the other hand, some authors have suggested that convection is likely to reduce the phase speed of tropical modes. For example, shallower convection has been theorized to associate with higher baroclinic modes, so would decrease the phase speed of the tropical mode; also, the static stability is reduced in the convective environment, so that tropical waves slow down [Zhang, 2005, Kiladis et al., 2009a]. Hence, the finding that MJO accelerates during wetter background moisture states suggests that other dynamics may control the phase speed of the MJO. For example, background wind effects, such as westward advection of the upper tropospheric circulation signal associated with the MJO, by background easterly wind, would slow the MJO relative to its average speed when that wind is anomalously strong. Figure 8 shows that when lower tropospheric moisture is high over the tropical Indian Ocean, upper tropospheric background wind tends to be less easterly than average, which would yield faster eastward movement. We found that fast MJO resembles a strong active and inactive phase of the intraseasonal moisture compared to the slow MJO (Fig. 4.8), consistent with predictions of a moisture mode theory. It is yet unclear whether the phase speed signal we observe in association with background moisture is consistent with moisture mode theory, which is focused on horizontal gradients of moisture more than the total background moisture. Aside from the Matsuno modes, Sobel et al. [2014] found a moisture mode moving eastward

under an equatorward moisture gradient and a weakly horizontal temperature gradient. This moisture mode was used later as a new foundation for MJO dynamics [e.g. Adames and Kim, 2016, Chen and Wang, 2019]. A subsequent paper will apply the above techniques to assess the associations of MJO phase speed with zonal and meridional moisture gradient configurations.

The energy source for these moisture mode instability models that sustains their eastward propagation is feedback between the convection and the large-scale circulation. Fuchs and Raymond [2005, 2007, 2017] constructed several shallow and vertically resolved models to simulate the moisture mode phase speeds and growth rates. They found that the wind-induced surface heat exchange (WISHE) is responsible for the eastward propagation of the moisture mode in their models. WISHE acts as a source of moisture and moist static energy. When the easterly anomalies at the east of the convection collocate with the background easterlies acting to increase the latent heat to the east of the convection it would lead to the growth and movement of the convection. Although that WISHE is known to work under background easterlies (such as the climatological conditions over the Pacific Ocean), the background zonal wind over the Indian Ocean associated with the background moisture is not systematically easterly (Fig. 4.6). Hence, WISHE could work over the Indian Ocean. The direction of the background moisture gradients over the Indian Ocean are also reversed from those over the Pacific. Moisture modes can exist without WISHE. If moisture gradually recharges the boundary layer everywhere, but if background moisture is more concentrated to the east, anomalous easterly wind that swaps the sign of the total wind would be able to transport moist air westward, thereby allowing advection of background moisture to support a moisture mode.

The intraseasonal moisture associated with the fast MJOs resembles wavenumber one (Fig. 4.8a), while slower MJOs project onto higher wavenumbers (Fig. 4.8b). The moist phase of the MJO moisture field associated with fast MJO shows a bulging structure to the east, which is absent in the slow MJO. The bulging structure might be associated with progressive pattern of shallow and congestus convection, which is theorized to moisten the atmosphere before the initiation of the deep convection Benedict and Randall [2007]. Hence, the absence of the shallow convection might reflects a rather weaker and slower MJOs. In terms of the traditional vertical normal structure of MJO, the The bulging structure of the

fast MJO indicates that baroclinic modes beyond the first baroclinic mode are required to account for the bulging structure, consistent with Haertel et al. [2008] who suggested the baroclinic structure of the MJO could be represented mainly using the first two baroclinic modes. Yet, at the same time, adding more higher baroclinic modes might reflect a slower propagation of the MJO. In terms of the radiative vertical structure of the MJO, the fast MJO resemble vertical structure close to the slow, moist Kelvin wave [Shaaban and Roundy, 2021b]

Aside from the moisture mode, the background upper-level zonal wind, associated with high background moisture over Eastern Africa, is less easterly than the seasonal average background wind, which would result in less westward advection, thereby yielding higher than average eastward phase speed. The magnitude of upper-level background zonal wind anomaly is comparable to the average phase speed of the MJO, strongly suggesting a role for a nonlinear advection of the MJO by the background upper flow. That is, the MJO may be faster in these moist environments because moist environments tend to be associated with upper tropospheric westerly wind anomaly, which would result in faster eastward propagation. More analysis is needed to estimate the relative contribution of the nonlinear advection versus moisture mode dynamics to MJO propagation. Could a bulb of the moisture be sustained by lower levels support of moist static energy irrespective of the effect of the upper air steering levels? Alternatively, if a moist coupled upper tropospheric Kelvin wave is a good mode of the MJO, the results presented here would suggest that the MJO might move faster across the Indian Ocean during moist periods because of advection by the westerly background wind that tends too occur in the basin at the same time.

CHAPTER 5

Conclusion

Eastward-moving convection near the equator includes a broad continuum of signals known as Kelvin waves and the Madden Julian oscillation (MJO). This dissertation analyzes the vertical structures and propagation characteristics of these signals, along with how they evolve differently during different background conditions. Chapter two shows that the tropospheric Kelvin wave could behave as a radiating wave as its counterpart stratospheric Kelvin wave. The horizontal structure of the Kelvin waves at specific phase speeds among different background zonal wind is presented in chapter three. Finally, we document in chapter four the variability of the MJO phase speed over the Indian Ocean among different background conditions. The findings in this dissertation were, in essence, led by a variety of novel statistical techniques that enabled us to examine the structure of tropical modes moving upward or downward at specific phase speeds and also the structure of the tropical modes at varies background conditions.

Kelvin waves and other Matsuno modes, are well presented as radiating waves in the stratosphere. Yet, vertical structure of their tropospheric counterpart, which was observed later, is explained in the tropical literature in terms of standing modes. It is not clear why such an explanation was proposed in the first place or agreed upon later by the community. Filtering Kelvin waves, especially the moist ones, over a bulk of wavenumbers and frequencies usually conflates simple plane waves structures found more easily in the stratosphere. Also, the urge to use simple boundary conditions when solving the tropospheric shallow water or primitive equation model may have motivated adopting the standing mode.

Using wavelet regression, we were able to find the Kelvin wave structure at a specific locations and at particular phase speeds. Then by regressing upward and downward phase filtered anomalies against the wavelet filtered indices, we found that the downward-phase signals occupy the troposphere as expected from an energy source settled at the upper troposphere with energy being directed downward. We found that the tropospheric waves share characteristics of the radiating stratospheric Kelvin wave similar to the Boussinesq model

Kelvin wave, including the following: an in-phase relationship between the zonal wind and height, quadrature relationship between the zonal wind and temperature, in-phase between the zonal and vertical wind in the stratosphere and out-of-phase relationship between the zonal and vertical wind.

The observed vertical wavelength of the regressed stratospheric waves is consistent with that of the calculated ones for the fast waves. Yet, for the slow waves, the observed wavelength is longer than the theoretical wavelength. In the troposphere, the vertical tilt of the 14 to 30 m s^{-1} waves shows the same vertical tilt suggested by the dispersion equation, that a dry environment (high static stability) might favor fast waves as the air parcel is forced to return to its equilibrium quickly compared to the moist environment. On the other hand, slow waves prefer a moist environment (low static stability). Under the radiative view of the tropical waves, the reduction of the phase speed of the modes in a moist environment could be understood in association with the reduced stability frequency rather than the superposition between higher-order baroclinic modes as in the normal modes view of the tropical waves.

Chapter three discusses the structure of the Kelvin waves at different background zonal wind and vertical wind shear. Instead of tracing wave packets ~~among~~ slowly varying background wind, a hierarchy of regressions was used to target signal at specific phase speed and specific environmental conditions (e.g., background flow, vertical wind shear). The capability of that technique to pull out waves at specific phase speed and background zonal wind makes it ideal for analyzing the structure of the wave near the critical layer. The horizontal structure of the Kelvin waves among easterly background zonal wind resembles the structure found by Matsuno. However, at a reduced quasi-Doppler shifted speed, zonal wind anomalies shifts eastward with respect to the geopotential, then at further reduction of the quasi-Doppler shifted speed, twin cyclones appear to the east of the base point as a part of the Gill pattern trough, with a relaxed Kelvin ridge with a meridional component of wind to the west of the base point. The evanescence of the Kelvin waves structure during background westerlies and its flourish with background easterlies is consistent with the quasi-Doppler shifted dispersion property of the Kelvin waves. The fading of the Kelvin waves' structure before encountering the critical layer suggests that dissipation factors are in play. Hence, differentiating between the theoretical and observed critical layer is useful to understand the

critical layer interaction. We found that Kelvin waves fade in westerly shear but propagate across easterly shear layer as suggested before by Lindzen and Holton in their theorization for the QBO. The absorption of the Kelvin wave in westerly shear is attributed to the critical layer's existence within the shear layer.

The behavior of the Kelvin waves under background zonal wind is well understood theoretically and in observations. However, under vertical wind shear, many aspects of the Kelvin waves are still not clear. In chapter two, we drove a dispersion equation for the Kelvin wave that accounts for the vertical wind shear of the zonal wind. We found that Kelvin waves decelerate under vertical wind shear of the zonal wind. Also, growth rate arose, suggesting an amplified mode of the Kelvin waves under vertical wind shear. The phase speed of the Kelvin waves was found to be associated with the Richardson number of the background environment. The value of the Richardson number changes with the vertical resolution of the data, hence raising questions on the actual depth of the vertical shear that Kelvin wave senses ~~actually~~.

In chapter four, we shed light on the variability of the phase speed of the MJO among different background conditions, as has been done with Kelvin waves in chapter three using the same varying regression technique. MJO as represented by the 850 hPa filtered zonal wind accelerates over the Indian Ocean with ~~the~~ increases of ~~the~~ background moisture (>90 days) over East Africa. The same behavior was also found using the background moisture over the western Indian Ocean and the eastern Indian Ocean. Also, the moisture field associated with the MJO intensifies with the background moisture. The acceleration of the moist MJO during moist background conditions contradicts the well-known deceleration of moist Kelvin waves discussed in chapter two. Hence, either wave dynamics are not altogether the key dynamics for the MJO, or other factors act to compensate for the role of the wave dynamics. This finding enriches the debate on the nature of the MJO and the extent to which the MJO could be understood as a moist Kelvin wave as the following: we found that the background moisture over East Africa is associated with a relaxation of the upper air background easterlies over the IO supporting the eastward propagation of the MJO. The classical work of the Matsuno modes ignores the role of the advection, yet given the advection's role, in this case, the advection of the intraseasonal field by the background wind could work against the role being acted by the reduced static stability. Future work

will consider budgeting analysis of the momentum equation. On the other hand, MJO could be understood as a moisture mode. We found that the MJO moisture field intensifies during wet background conditions with a vertical structure that resemble an evolving convective pattern. That might reflect positive feedback between the precipitation, which is one of the moisture mode theory pillars. Future work will include a comparison between the dispersion characteristics deduced from the wave (Matsuno) dynamics with that of the moisture mode against the observation might shed more light on the nature of the MJO.

The results found in this dissertation reveals that the reduction of the static stability is not consistent with the acceleration of the MJO during wet environments. However, reducing the static stability is key to understand the reduction of the phase speed of the moist Kelvin waves under the radiating wave paradigm where superposition between classical normal mode under the rigid tropopause is not the case. Analyzing the Kelvin waves' radiative characteristics could also be done by assuming a rigid lid at the top of the atmosphere (0 hPa), which is an implicit assumption in the upward-downward wave decomposition. Those vertical structures of the new normal mode should be different from the traditional ones. Background wind and shear affect the phase speed and structure of the stratospheric Kelvin waves, as discussed in chapter three. Also, relaxation of the background easterlies during moist environment over the Indian Ocean might accelerate the MJO. In case the reduction of the phase speed of the MJO is not compensated by the advection by the background flow, then a new paradigm is needed to understand the dynamics of the MJO. Given that the MJO moisture filed during moist background states, then analyzing MJO as moisture mode might be a promising avenue.

Supplementary material

S.1 Supplementary material of chapter 1

S.1.1 Upward and downward data decomposition of artificial and real data.

Since the vertical grid is uneven, it is helpful to test the decomposition algorithm on an ideal signal before applying it to the real data. To accomplish that, we resolve a simple ideal upward-phase wave (Fig. S1a) into upward-phase and downward-phase components, and as expected, the upward-phase component (Fig. S1b) resembles all the ideal signal while the downward-phase component is almost zero (Fig. S1c). The sum of the upward-phase and downward-phase components (Fig. S1d) is almost identical to the ideal signal, and the difference between them is almost zero as shown in Fig. S1e. We used upward-phase and downward-phase phrases in this supplementary document to distinguish them from the upward and downward waves in the manuscript which refer to the energy propagation rather than the phase direction, which agrees with the bulk of atmospheric waves' literature.

We know that the patterns in the reanalysis data are far more complicated than simple sinusoidal signals. For example, pressure and density decrease by e^{-1} over scale height in the troposphere, vertical velocity decreases rapidly above the tropopause, and temperature fluctuations increase rapidly above the tropopause. Thus, we artificially create the signal of a sinusoidal upward-phase wave with an amplitude that decays with height (Fig. S1f), and decompose it into upward-phase and downward-phase components. As before, most of the filtered signal appears in the upward-phase component (Fig. S1g), except a pattern in the form of a reflection at the upper boundary. Similar apparent reflections also appear in the downward-phase component at the upper and lower boundary (Fig. S1h). Those reflections in the upward-phase and downward-phase components are out of phase; hence, they cancel each other after summation (Fig. S1i-j). The reflections at the boundaries appear due to the aperiodicity of the dataset in vertical space. However, those artifacts must wash out once the upward-phase and downward-phase components are combined. Since most of the reanalysis dataset exists on unevenly sampled pressure levels, we included all vertical wavenumbers in the upward-phase and the downward-phase components. This approach minimizes artifacts

of the uneven grid.

We present the upward-phase and downward-phase components of the QBO zonal wind as a demonstration of the efficiency of the filter technique on real data. We chose the QBO zonal wind because we know beforehand that it propagates downward, hence we expect that most of the amplitude of the QBO is embedded in the downward-phase component. Figure S2a shows the unfiltered zonal wind from 1990 to 2005 averaged between 10°S and 10°N and at 80°E. Zonal wind structure between 70 and 5 hPa resembles the QBO. As expected, the downward component contains most of the QBO amplitudes (Fig. S2c), whereas high-frequency upward oscillations dominate most of the upward-phase component (Fig. S2b).

S.1.2 Vertical wavelengths and speeds of the tropospheric and stratospheric Kelvin waves.

c	7	11	14	16	20	28	30
L_t	5.3(3.4)	7.4(5.8)	9.3(7.8)	10.1(8.6)	12.3(10.6)	16.9(15.1)	17.8(16.1)
w_t	0.32(0.2)	0.7(0.5)	1.1(0.9)	1.38(1.1)	2.1(1.8)	4.1 (3.7)	4.6(4.1)
L_s	1.9(2.5)	2.9(3.5)	3.6(4.1)	3.9(4.5)	5.3(5.8)	7.4(7.9)	7.7(8.2)
w_s	0.12(0.15)	0.27(0.33)	0.44(0.5)	0.54(0.6)	0.91(1)	1.79(1.9)	1.9(2.1)

Table S1: Horizontal phase speed c (m s^{-1}), associated tropospheric and stratospheric vertical wavelengths L_t and L_s (km), and tropospheric and stratospheric vertical velocity w_t and w_s (km day^{-1}). Numbers outside parentheses are calculated using zonal mean of the zonal wind during periods of enhanced variance of the U850 base index. Numbers inside the parentheses are the same except using the zonal wind at 80°E. The tropospheric background wind is vertically averaged between 1000 and 200 hPa, and the stratospheric background wind is vertically averaged between 100 and 30 hPa. The tropospheric and stratospheric Brunt-Väisälä frequency are based on lapse rate of -7 and 2.5 k km^{-1} and scale height of 6.1 km.

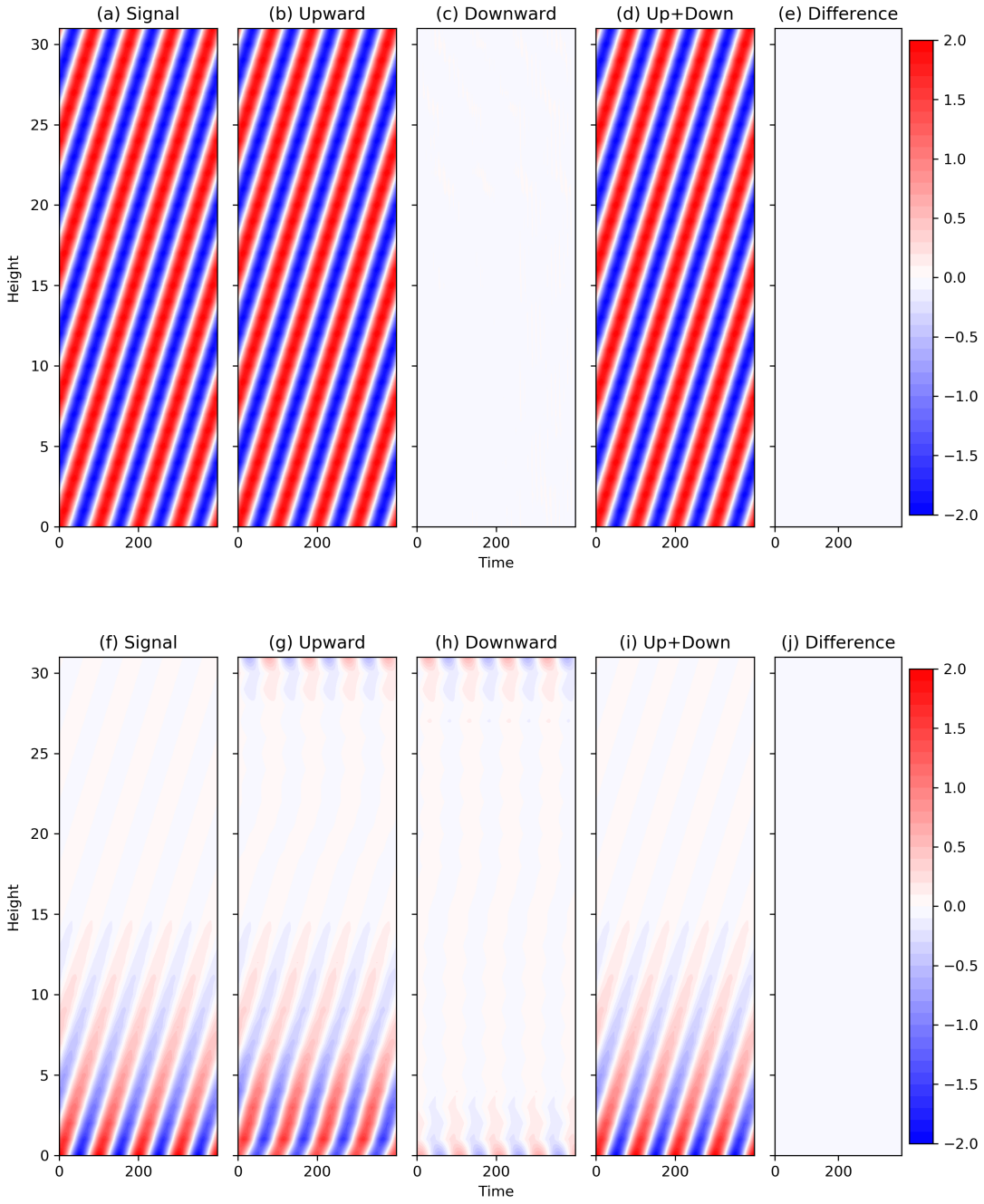

Figure S1: Decomposition of (a) a sinusoidal upward-phase wave (top panel) into (b) the upward-phase component, (c) the downward-phase component, (d) the sum of both upward-phase and downward-phase components, (e) Difference between the signal and the sum of both upward-phase and downward-phase components. The same decomposition is repeated for (f) a decaying upward-phase wave with height (bottom panel), g, h, i, and j have the same meanings as b,c,d, and e.

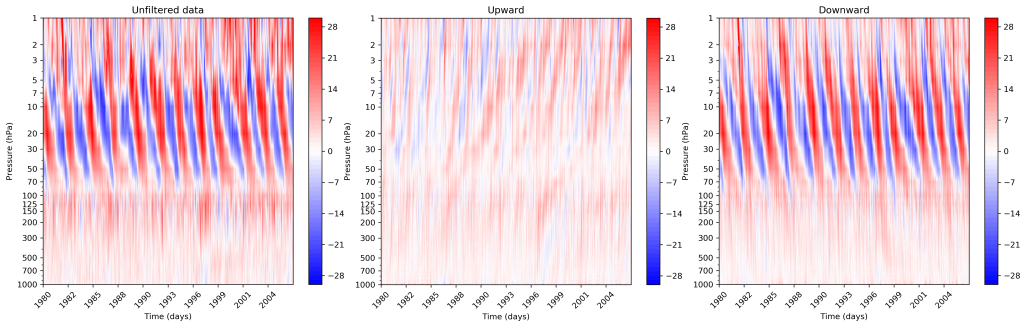

Figure S2: Decomposition of (a) unfiltered zonal wind (shaded at interval of 1 m s^{-1}) at 80°E averaged between 10°S and 10°N into, (b) upward -phase component, and (c) downward-phase component. Westerlies are in red and easterlies are in blue.

BIBLIOGRAPHY

Ángel F. Adames and Daehyun Kim. The MJO as a Dispersive, Convectively Coupled Moisture Wave: Theory and Observations. *Journal of the Atmospheric Sciences*, 73(3): 913–941, 02 2016. ISSN 0022-4928. doi: 10.1175/JAS-D-15-0170.1. URL https://doi.org/10.1175/JAS-D-15-0170.1.

Joseph Allan Andersen and Zhiming Kuang. Moist Static Energy Budget of MJO-like Disturbances in the Atmosphere of a Zonally Symmetric Aquaplanet. *Journal of Climate*, 25(8):2782–2804, 04 2012. ISSN 0894-8755. doi: 10.1175/JCLI-D-11-00168.1. URL https://doi.org/10.1175/JCLI-D-11-00168.1.

D.G. Andrews, C.B. Leovy, and J.R. Holton. *Middle Atmosphere Dynamics*. International Geophysics. Elsevier Science, 1987. ISBN 9780080954677. URL https://books.google.com/books?id=4CPLCQAAQBAJ.

M. P. Baldwin, L. J. Gray, T. J. Dunkerton, K. Hamilton, P. H. Haynes, W. J. Randel, J. R. Holton, M. J. Alexander, I. Hirota, T. Horinouchi, D. B. A. Jones, J. S. Kinnersley, C. Marquardt, K. Sato, and M. Takahashi. The quasi-biennial oscillation. *Reviews of Geophysics*, 39(2):179–229, 2001a. doi: 10.1029/1999RG000073. URL https://agupubs.onlinelibrary.wiley.com/doi/abs/10.1029/1999RG000073.

M. P. Baldwin, L. J. Gray, T. J. Dunkerton, K. Hamilton, P. H. Haynes, W. J. Randel, J. R. Holton, M. J. Alexander, I. Hirota, T. Horinouchi, D. B. A. Jones, J. S. Kinnersley, C. Marquardt, K. Sato, and M. Takahashi. The quasi-biennial oscillation. *Reviews of Geophysics*, 39(2):179–229, 2001b. URL https://agupubs.onlinelibrary.wiley.com/doi/abs/10.1029/1999RG000073.

Christian H. Bantzer and John M. Wallace. Intraseasonal Variability in Tropical Mean Temperature and Precipitation and Their Relation to the Tropical 40–50 Day Oscillation. *Journal of the Atmospheric Sciences*, 53(21):3032–3045, 11 1996. ISSN 0022-4928. doi: 10.1175/1520-0469(1996)053⟨3032:IVITMT⟩2.0.CO;2. URL https://doi.org/10.1175/1520-0469(1996)053<3032:IVITMT>2.0.CO;2.

James J. Benedict and David A. Randall. Observed Characteristics of the MJO Relative to Maximum Rainfall. *Journal of the Atmospheric Sciences*, 64(7):2332–2354, 07 2007. ISSN 0022-4928. doi: 10.1175/JAS3968.1. URL https://doi.org/10.1175/JAS3968.1.

John R. Booker and Francis P. Bretherton. The critical layer for internal gravity waves in a shear flow. *Journal of Fluid Mechanics*, 27(3):513–539, 1967. doi: 10.1017/S0022112067000515.

F. P. Bretherton. The propagation of groups of internal gravity waves in a shear flow. *Quarterly Journal of the Royal Meteorological Society*, 92(394):466–480, 1966. doi: 10.1002/qj.49709239403. URL https://rmets.onlinelibrary.wiley.com/doi/abs/10.1002/qj.49709239403.

Kirk Bryan. A numerical method for the study of the circulation of the world ocean. *Journal of Computational Physics*, 4(3):347 – 376, 1969. ISSN 0021-9991. URL http://www.sciencedirect.com/science/article/pii/0021999169900047.

Wenju Cai, Peter van Rensch, Tim Cowan, and Harry H. Hendon. Teleconnection pathways of enso and the iod and the mechanisms for impacts on australian rainfall. *Journal of Climate*, 24(15):3910 – 3923, 2011. doi: 10.1175/2011JCLI4129.1. URL https://journals.ametsoc.org/view/journals/clim/24/15/2011jcli4129.1.xml.

C-P. Chang and H. Lim. Kelvin Wave-CISK: A Possible Mechanism for the 30–50 Day Oscillations. *Journal of the Atmospheric Sciences*, 45(11):1709–1720, 06 1988. ISSN 0022-4928. doi: 10.1175/1520-0469(1988)045⟨1709:KWCAPM⟩2.0.CO;2. URL https://doi.org/10.1175/1520-0469(1988)045<1709:KWCAPM>2.0.CO;2.

Guosen Chen and Bin Wang. Dynamic moisture mode versus moisture mode in MJO dynamics: importance of the wave feedback and boundary layer convergence feedback. *Climate Dynamics*, 52(9-10):5127–5143, May 2019. doi: 10.1007/s00382-018-4433-7.

Lyubov G. Chumakova, Rodolfo R. Rosales, and Esteban G. Tabak. Leaky rigid lid: New dissipative modes in the troposphere. *Journal of the Atmospheric Sciences*, 70(10):3119–3127, 2013. URL https://doi.org/10.1175/JAS-D-12-065.1.

U. Das and C. J. Pan. Strong kelvin wave activity observed during the westerly phase of qbo – a case study. *Annales Geophysicae*, 31(4):581–590, 2013. doi: 10.5194/angeo-31-581-2013. URL https://www.ann-geophys.net/31/581/2013/.

D. P. Dee, S. M. Uppala, A. J. Simmons, P. Berrisford, P. Poli, S. Kobayashi, U. Andrae, M. A. Balmaseda, G. Balsamo, P. Bauer, P. Bechtold, A. C. M. Beljaars, L. van de Berg, J. Bidlot, N. Bormann, C. Delsol, R. Dragani, M. Fuentes, A. J. Geer, L. Haimberger, S. B. Healy, H. Hersbach, E. V. Hólm, L. Isaksen, P. Kållberg, M. Köhler, M. Matricardi, A. P. McNally, B. M. Monge-Sanz, J.-J. Morcrette, B.-K. Park, C. Peubey, P. de Rosnay, C. Tavolato, J.-N. Thépaut, and F. Vitart. The era-interim reanalysis: configuration and performance of the data assimilation system. *Quarterly Journal of the Royal Meteorological Society*, 137(656):553–597, 2011. doi: 10.1002/qj.828. URL https://rmets.onlinelibrary.wiley.com/doi/abs/10.1002/qj.828.

Juliana Dias and George N. Kiladis. Influence of the basic state zonal flow on convectively coupled equatorial waves. *Geophysical Research Letters*, 41(19):6904–6913, 2014. doi: 10.1002/2014GL061476. URL https://agupubs.onlinelibrary.wiley.com/doi/abs/10.1002/2014GL061476.

Dale R. Durran. Open boundary conditions: Fact and fiction. In P. F. Hodnett, editor, *IUTAM Symposium on Advances in Mathematical Modelling of Atmosphere and Ocean Dynamics*, pages 1–18, Dordrecht, 2001. Springer Netherlands. ISBN 978-94-010-0792-4.

Jacob P. Edman and David M. Romps. Beyond the rigid lid: Baroclinic modes in a structured atmosphere. *Journal of the Atmospheric Sciences*, 74(11):3551–3566, 2017. URL https://doi.org/10.1175/JAS-D-17-0140.1.

Kerry A. Emanuel, J. David Neelin, and Christopher S. Bretherton. On large-scale circulations in convecting atmospheres. *Quarterly Journal of the Royal Meteorological Society*, 120(519):1111–1143, 1994. URL https://rmets.onlinelibrary.wiley.com/doi/abs/10.1002/qj.49712051902.

M. Ern and P. Preusse. Quantification of the contribution of equatorial kelvin waves to the qbo wind reversal in the stratosphere. *Geophysical Research Letters*, 36(21), 2009a. doi: 10.1029/2009GL040493. URL https://agupubs.onlinelibrary.wiley.com/doi/abs/10.1029/2009GL040493.

M. Ern and P. Preusse. Quantification of the contribution of equatorial kelvin waves to the qbo wind reversal in the stratosphere. *Geophysical Research Letters*, 36(21), 2009b. doi: 10.1029/2009GL040493. URL https://agupubs.onlinelibrary.wiley.com/doi/abs/10.1029/2009GL040493.

T. J. Flannaghan and S. Fueglistaler. The importance of the tropical tropopause layer for equatorial kelvin wave propagation. *Journal of Geophysical Research: Atmospheres*, 118 (11):5160–5175, 2013. doi: https://doi.org/10.1002/jgrd.50418. URL https://agupubs.onlinelibrary.wiley.com/doi/abs/10.1002/jgrd.50418.

David C. Fritts and M. Joan Alexander. Gravity wave dynamics and effects in the middle atmosphere. *Reviews of Geophysics*, 41(1), 2003. doi: https://doi.org/10.1029/2001RG000106. URL https://agupubs.onlinelibrary.wiley.com/doi/abs/10.1029/2001RG000106.

Zeljka Fuchs and David Raymond. A simple, vertically resolved model of tropical disturbances with a humidity closure. *Tellus A: Dynamic Meteorology and Oceanography*, 59(3): 344–354, 2007. doi: 10.1111/j.1600-0870.2007.00230.x. URL https://doi.org/10.1111/j.1600-0870.2007.00230.x.

Zeljka Fuchs and David J. Raymond. Large-scale modes in a rotating atmosphere with radiative–convective instability and wishe. *Journal of the Atmospheric Sciences*, 62(11): 4084–4094, 2005. doi: 10.1175/JAS3582.1. URL https://doi.org/10.1175/JAS3582.1.

Zeljka Fuchs and David J. Raymond. A simple model of intraseasonal oscillations. *Journal of Advances in Modeling Earth Systems*, 9(2):1195–1211, 2017. doi: 10.1002/2017MS000963. URL https://agupubs.onlinelibrary.wiley.com/doi/abs/10.1002/2017MS000963.

Rolando R. Garcia and Murry L. Salby. Transient response to localized episodic heating in the tropics. part ii: Far-field behavior. *Journal of Atmospheric Sciences*, 44(2):499 – 532, 1987. doi: 10.1175/1520-0469(1987)044⟨0499:TRTLEH⟩2.0.CO;2. URL https://journals.ametsoc.org/view/journals/atsc/44/2/1520-0469_1987_044_0499_trtleh_2_0_co_2.xml.

Theo Gerkema, Leo R. M. Maas, and Hans van Haren. A note on the role of mean flows in

doppler-shifted frequencies. *Journal of Physical Oceanography*, 43(2):432–441, 2013. URL https://doi.org/10.1175/JPO-D-12-0901.

A. E. Gill. Some simple solutions for heat-induced tropical circulation. *Quarterly Journal of the Royal Meteorological Society*, 106(449):447–462, 1980. ISSN 1477-870X. URL http://dx.doi.org/10.1002/qj.49710644905.

A.E. Gill. *Atmosphere-Ocean Dynamics*. International Geophysics. Elsevier Science, 1982. ISBN 9780080570525. URL https://books.google.com/books?id=8kFPh_SvnAIC.

Patrick T. Haertel and George N. Kiladis. Dynamics of 2-day equatorial waves. *Journal of the Atmospheric Sciences*, 61(22):2707–2721, 2004. URL https://doi.org/10.1175/JAS3352.1.

Patrick T. Haertel, George N. Kiladis, Andrew Denno, and Thomas M. Rickenbach. Vertical-mode decompositions of 2-day waves and the madden–julian oscillation. *Journal of the Atmospheric Sciences*, 65(3):813–833, 2008. URL https://doi.org/10.1175/2007JAS2314.1.

Oliver J. Halliday, Stephen D. Griffiths, Douglas J. Parker, Alison Stirling, and Simon Vosper. Forced gravity waves and the tropospheric response to convection. *Quarterly Journal of the Royal Meteorological Society*, 144(712):917–933, 2018. doi: https://doi.org/10.1002/qj.3278. URL https://rmets.onlinelibrary.wiley.com/doi/abs/10.1002/qj.3278.

Dennis L. Hartmann, Harry H. Hendon, and Robert A. Houze. Some implications of the mesoscale circulations in tropical cloud clusters for large-scale dynamics and climate. *Journal of the Atmospheric Sciences*, 41(1):113–121, 1984. URL https://doi.org/10.1175/1520-0469(1984)041<0113:SIOTMC>2.0.CO;2.

Harry H. Hendon and Murry L. Salby. The life cycle of the madden–julian oscillation. *Journal of the Atmospheric Sciences*, 51(15):2225–2237, 1994. doi: 10.1175/1520-0469(1994)051⟨2225:TLCOTM⟩2.0.CO;2. URL https://doi.org/10.1175/1520-0469(1994)051<2225:TLCOTM>2.0.CO;2.

JAMES R. Holton. The influence of mean wind shear on the propagation of kelvin waves1. *Tellus*, 22(2):186–193, 1970. doi: 10.1111/j.2153-3490.1970.tb01520.x. URL https://onlinelibrary.wiley.com/doi/abs/10.1111/j.2153-3490.1970.tb01520.x.

James R. Holton and Gregory J. Hakim. *Chapter 12 - Middle Atmosphere Dynamics*, pages 413 – 452. Academic Press, Boston, fifth edition edition, 2013. ISBN 978-0-12-384866-6. URL http://www.sciencedirect.com/science/article/pii/B978012384866600012X.

James R. Holton, M. Joan Alexander, and Matthew T. Boehm. Evidence for short vertical wavelength kelvin waves in the department of energy-atmospheric radiation measurement nauru99 radiosonde data. *Journal of Geophysical Research: Atmospheres*, 106(D17): 20125–20129, 2001. doi: 10.1029/2001JD900108.

J.R. Holton and G.J. Hakim. *An Introduction to Dynamic Meteorology*. ISSN. Elsevier Science, 2012. ISBN 9780123848673. URL https://books.google.com/books?id=hcxcqQp7XOsC.

Robert A. Houze. Stratiform precipitation in regions of convection: A meteorological paradox? *Bulletin of the American Meteorological Society*, 78(10):2179–2196, 1997. URL https://doi.org/10.1175/1520-0477(1997)078<2179:SPIROC>2.0.CO;2.

Pang-chi Hsu and Tim Li. Role of the boundary layer moisture asymmetry in causing the eastward propagation of the madden–julian oscillation. *Journal of Climate*, 25(14): 4914–4931, 2012. doi: 10.1175/JCLI-D-11-00310.1. URL https://doi.org/10.1175/JCLI-D-11-00310.1.

Kuniaki Inoue and Larissa Back. Column-Integrated Moist Static Energy Budget Analysis on Various Time Scales during TOGA COARE. *Journal of the Atmospheric Sciences*, 72 (5):1856–1871, 05 2015. ISSN 0022-4928. doi: 10.1175/JAS-D-14-0249.1. URL https://doi.org/10.1175/JAS-D-14-0249.1.

Xianan Jiang, Ángel F. Adames, Ming Zhao, Duane Waliser, and Eric Maloney. A Unified Moisture Mode Framework for Seasonality of the Madden–Julian Oscillation. *Journal of Climate*, 31(11):4215–4224, 05 2018. ISSN 0894-8755. doi: 10.1175/JCLI-D-17-0671.1. URL https://doi.org/10.1175/JCLI-D-17-0671.1.

R. Johnson, W. Schubert, R. Taft, and P. Ciesielski. L3 high resolution radiosonde data: Dynamo legacy collection. version 1.0, 2019. URL https://data.eol.ucar.edu/dataset/347.237.

George N. Kiladis, Katherine H. Straub, and Patrick T. Haertel. Zonal and vertical structure of the madden–julian oscillation. *Journal of the Atmospheric Sciences*, 62(8):2790–2809, 2005. URL https://doi.org/10.1175/JAS3520.1.

George N. Kiladis, Matthew C. Wheeler, Patrick T. Haertel, Katherine H. Straub, and Paul E. Roundy. Convectively coupled equatorial waves. *Reviews of Geophysics*, 47(2), 2009a. doi: 10.1029/2008RG000266. URL https://agupubs.onlinelibrary.wiley.com/doi/abs/10.1029/2008RG000266.

George N. Kiladis, Matthew C. Wheeler, Patrick T. Haertel, Katherine H. Straub, and Paul E. Roundy. Convectively coupled equatorial waves. *Reviews of Geophysics*, 47(2), 2009b. doi: 10.1029/2008RG000266. URL https://agupubs.onlinelibrary.wiley.com/doi/abs/10.1029/2008RG000266.

Hye-Mi Kim. The impact of the mean moisture bias on the key physics of mjo propagation in the ecmwf reforecast. *Journal of Geophysical Research: Atmospheres*, 122(15):7772–7784, 2017. doi: 10.1002/2017JD027005. URL https://agupubs.onlinelibrary.wiley.com/doi/abs/10.1002/2017JD027005.

Y.-H. Kim and H.-Y. Chun. Momentum forcing of the quasi-biennial oscillation by equatorial waves in recent reanalyses. *Atmospheric Chemistry and Physics*, 15(12):6577–6587, 2015a. doi: 10.5194/acp-15-6577-2015. URL https://www.atmos-chem-phys.net/15/6577/2015/.

Y.-H. Kim and H.-Y. Chun. Contributions of equatorial wave modes and parameterized gravity waves to the tropical qbo in hadgem2. *Journal of Geophysical Research: Atmospheres*, 120(3):1065–1090, 2015b. doi: 10.1002/2014JD022174. URL https://agupubs.onlinelibrary.wiley.com/doi/abs/10.1002/2014JD022174.

P.H. LeBlond and L.A. Mysak. *Waves in the Ocean*. Elsevier Oceanography Series. Elsevier Science, 1981. ISBN 9780080879772. URL https://books.google.com/books?id=TYGIwzz_k8kC.

Tim Li, Chongbo Zhao, Pang-chi Hsu, and Tomoe Nasuno. Mjo initiation processes over the tropical indian ocean during dynamo/cindy2011. *Journal of Climate*, 28(6): 2121–2135, 2015. doi: 10.1175/JCLI-D-14-00328.1. URL https://doi.org/10.1175/JCLI-D-14-00328.1.

Brant Liebmann and Catherine A. Smith. Description of a complete (interpolated) outgoing longwave radiation dataset. *Bulletin of the American Meteorological Society*, 77(6):1275–1277, 1996. ISSN 00030007, 15200477. URL http://www.jstor.org/stable/26233278.

Richard S. Lindzen. Planetary waves on beta-planes. *Monthly Weather Review*, 95(7): 441–451, 1967. URL https://doi.org/10.1175/1520-0493(1967)095<0441:PWOBP>2.3.CO;2.

Richard S. Lindzen. Internal equatorial planetary-scale waves in shear flow. *Journal of the Atmospheric Sciences*, 27(3):394–407, 1970. doi: 10.1175/1520-0469(1970)027⟨0394:IEPSWI⟩2.0.CO;2. URL https://doi.org/10.1175/1520-0469(1970)027<0394:IEPSWI>2.0.CO;2.

Richard S. Lindzen. Equatorial Planetary Waves in Shear. Part I. *Journal of the Atmospheric Sciences*, 28(4):609–622, 05 1971. ISSN 0022-4928. doi: 10.1175/1520-0469(1971)028⟨0609:EPWISP⟩2.0.CO;2. URL https://doi.org/10.1175/1520-0469(1971)028<0609:EPWISP>2.0.CO;2.

Richard S. Lindzen. Equatorial Planetary Waves in Shear: Part II. *Journal of the Atmospheric Sciences*, 29(8):1452–1463, 11 1972. ISSN 0022-4928. doi: 10.1175/1520-0469(1972)029⟨1452:EPWISP⟩2.0.CO;2. URL https://doi.org/10.1175/1520-0469(1972)029<1452:EPWISP>2.0.CO;2.

Richard S. Lindzen. The interaction of waves and convection in the tropics. *Journal of the Atmospheric Sciences*, 60(24):3009–3020, 2003. URL https://doi.org/10.1175/1520-0469(2003)060<3009:TIOWAC>2.0.CO;2.

Richard S. Lindzen and James R. Holton. A theory of the quasi-biennial oscillation. *Journal of the Atmospheric Sciences*, 25(6):1095–1107, 1968. URL https://doi.org/10.1175/1520-0469(1968)025<1095:ATOTQB>2.0.CO;2.

Jian Ling and Chidong Zhang. Diabatic Heating Profiles in Recent Global Reanalyses. *Journal of Climate*, 26(10):3307–3325, 05 2013. ISSN 0894-8755. doi: 10.1175/JCLI-D-12-00384.1. URL https://doi.org/10.1175/JCLI-D-12-00384.1.

Brian E. Mapes. Convective inhibition, subgrid-scale triggering energy, and stratiform instability in a toy tropical wave model. *Journal of the Atmospheric Sciences*, 57(10):1515–1535, 2000. URL https://doi.org/10.1175/1520-0469(2000)057<1515:CISSTE>2.0.CO;2.

Taroh Matsuno. Quasi-geostrophic motions in the equatorial area. *Journal of the Meteorological Society of Japan. Ser. II*, 44(1):25–43, 1966. doi: 10.2151/jmsj1965.44.1_25.

Adrian J. Matthews. Primary and successive events in the madden–julian oscillation. *Quarterly Journal of the Royal Meteorological Society*, 134(631):439–453, 2008. doi: 10.1002/qj.224. URL https://rmets.onlinelibrary.wiley.com/doi/abs/10.1002/qj.224.

D. E. Mowbray and B. S. H. Rarity. A theoretical and experimental investigation of the phase configuration of internal waves of small amplitude in a density stratified liquid. *Journal of Fluid Mechanics*, 28(1):1–16, 1967. doi: 10.1017/S0022112067001867.

Balachandrudu Narapusetty, Timothy DelSole, and Michael K. Tippett. Optimal estimation of the climatological mean. *Journal of Climate*, 22(18):4845–4859, 2009a. doi: 10.1175/2009JCLI2944.1. URL https://doi.org/10.1175/2009JCLI2944.1.

Balachandrudu Narapusetty, Timothy DelSole, and Michael K. Tippett. Optimal estimation of the climatological mean. *Journal of Climate*, 22(18):4845–4859, 2009b. URL https://doi.org/10.1175/2009JCLI2944.1.

Hamid A. Pahlavan, Qiang Fu, John M. Wallace, and George N. Kiladis. Revisiting the quasi-biennial oscillation as seen in era5. part i: Description and momentum budget. *Journal of the Atmospheric Sciences*, 78(3):673 – 691, 2021a. doi: 10.1175/JAS-D-20-0248.1. URL https://journals.ametsoc.org/view/journals/atsc/78/3/JAS-D-20-0248.1.xml.

Hamid A. Pahlavan, John M. Wallace, Qiang Fu, and George N. Kiladis. Revisiting the quasi-biennial oscillation as seen in era5. part ii: Evaluation of waves and wave forcing. *Journal of the Atmospheric Sciences*, 78(3):693 – 707, 2021b. doi: 10.1175/JAS-D-20-0249.1. URL https://journals.ametsoc.org/view/journals/atsc/78/3/JAS-D-20-0249.1.xml.

R. A. plumb. The circulation of the middle atmosphere. *Australian Met Magazine*, 30: 107–121, 1981.

R. Alan Plumb and Robert C. Bell. Equatorial waves in steady zonal shear flow. *Quarterly Journal of the Royal Meteorological Society*, 108(456):313–334, 1982. doi: 10.1002/qj.49710845603. URL https://rmets.onlinelibrary.wiley.com/doi/abs/10.1002/qj.49710845603.

William J. Randel and Isaac M. Held. Phase speed spectra of transient eddy fluxes and critical layer absorption. *Journal of Atmospheric Sciences*, 48(5):688 – 697, 1991. doi: 10.1175/1520-0469(1991)048⟨0688:PSSOTE⟩2.0.CO;2. URL https://journals.ametsoc.org/view/journals/atsc/48/5/1520-0469_1991_048_0688_pssote_2_0_co_2.xml.

William J. Randel and Fei Wu. Kelvin wave variability near the equatorial tropopause observed in gps radio occultation measurements. *Journal of Geophysical Research: Atmospheres*, 110(D3), 2005. URL https://agupubs.onlinelibrary.wiley.com/doi/abs/10.1029/2004JD005006.

Paul E. Roundy. Observed structure of convectively coupled waves as a function of equivalent depth: Kelvin waves and the madden–julian oscillation. *Journal of the Atmospheric Sciences*, 69(7):2097–2106, 2012. URL https://doi.org/10.1175/JAS-D-12-03.1.

Paul E. Roundy. Regression analysis of zonally narrow components of the mjo. *Journal of the Atmospheric Sciences*, 71(11):4253–4275, 2014. URL https://doi.org/10.1175/JAS-D-13-0288.1.

Paul E. Roundy. Diagnosis of seasonally varying regression slope coefficients and application to the mjo. *Quarterly Journal of the Royal Meteorological Society*, 143(705):1946–1952, 2017a. doi: 10.1002/qj.3054. URL https://rmets.onlinelibrary.wiley.com/doi/abs/10.1002/qj.3054.

Paul E. Roundy. A wave-number frequency wavelet analysis of convectively coupled equatorial waves and the mjo over the indian ocean. *Quarterly Journal of the Royal Meteorological Society*, pages n/a–n/a, 2017b. ISSN 1477-870X. doi: 10.1002/qj.3207. URL http://dx.doi.org/10.1002/qj.3207.

Paul E. Roundy. Interpretation of the spectrum of eastward-moving tropical convective anomalies. *Quarterly Journal of the Royal Meteorological Society*, n/a(n/a), 2019. URL https://rmets.onlinelibrary.wiley.com/doi/abs/10.1002/qj.3709.

Paul E. Roundy and William M. Frank. A climatology of waves in the equatorial region. *Journal of the Atmospheric Sciences*, 61(17):2105–2132, 2004. URL https://doi.org/10.1175/1520-0469(2004)061<2105:ACOWIT>2.0.CO;2.

Paul E. Roundy and Matthew A. Janiga. Analysis of vertically propagating convectively coupled equatorial waves using observations and a non-hydrostatic boussinesq model on the equatorial beta-plane. *Quarterly Journal of the Royal Meteorological Society*, 138(665): 1004–1017, 2012. URL https://rmets.onlinelibrary.wiley.com/doi/abs/10.1002/qj.983.

Hualan Rui and Bin Wang. Development characteristics and dynamic structure of tropical intraseasonal convection anomalies. *Journal of the Atmospheric Sciences*, 47(3):357–379, 1990. doi: 10.1175/1520-0469(1990)047⟨0357:DCADSO⟩2.0.CO;2. URL https://doi.org/10.1175/1520-0469(1990)047<0357:DCADSO>2.0.CO;2.

Jung-Hee Ryu, Sukyoung Lee, and Seok-Woo Son. Vertically propagating kelvin waves and tropical tropopause variability. *Journal of the Atmospheric Sciences*, 65(6):1817–1837, 2008. URL https://doi.org/10.1175/2007JAS2466.1.

Naoko Sakaeda and Paul E. Roundy. The development of upper-tropospheric wind over the western hemisphere in association with mjo convective initiation. *Journal of the Atmospheric Sciences*, 72(8):3138–3160, 2015. URL https://doi.org/10.1175/JAS-D-14-0293.1.

Murry L. Salby and Rolando R. Garcia. Transient response to localized episodic heating in the tropics. part i: Excitation and short-time near-field behavior. *Journal of the Atmospheric Sciences*, 44(2):458–498, 1987. URL https://doi.org/10.1175/1520-0469(1987)044<0458:TRTLEH>2.0.CO;2.

Murry L. Salby and Harry H. Hendon. Intraseasonal Behavior of Clouds, Temperature, and Motion in the Tropics. *Journal of the Atmospheric Sciences*, 51(15):2207–2224, 08

1994. ISSN 0022-4928. doi: 10.1175/1520-0469(1994)051⟨2207:IBOCTA⟩2.0.CO;2. URL https://doi.org/10.1175/1520-0469(1994)051<2207:IBOCTA>2.0.CO;2.

B. Scherllin-Pirscher, W. J. Randel, and J. Kim. Tropical temperature variability and kelvin-wave activity in the utls from gps ro measurements. *Atmospheric Chemistry and Physics*, 17(2):793–806, 2017. doi: 10.5194/acp-17-793-2017. URL https://acp.copernicus.org/articles/17/793/2017/.

Courtney Schumacher and Robert A. Houze. Stratiform rain in the tropics as seen by the trmm precipitation radar. *Journal of Climate*, 16(11):1739–1756, 2003. URL https://doi.org/10.1175/1520-0442(2003)016<1739:SRITTA>2.0.CO;2.

Ahmed Shaaban and Paul Roundy. Upward and downward atmospheric kelvin waves across different speeds over the indian ocean. *quarterly journal of the royal meteorological society.*, 00(0):000–000, 2021a. doi: 10.1175/1520-0469(1987)044⟨0458:TRTLEH⟩2.0.CO;2. URL https://doi.org/10.1175/1520-0469(1987)044<0458:TRTLEH>2.0.CO;2.

Ahmed Shaaban and Paul Roundy. Upward and downward atmospheric kelvin waves across different speeds over the indian ocean. *Quarterly Journal of the Royal Meteorological Society*, nan(nan):nan – nan, 2021b. doi: nan. URL nan.

Ahmed A. Shaaban and Paul E. Roundy. Olr perspective on the indian ocean dipole with application to east african precipitation. *Quarterly Journal of the Royal Meteorological Society*, 143(705):1828–1843, 2017. doi: 10.1002/qj.3045. URL https://rmets.onlinelibrary.wiley.com/doi/abs/10.1002/qj.3045.

Adam Sobel, Shuguang Wang, and Daehyun Kim. Moist Static Energy Budget of the MJO during DYNAMO. *Journal of the Atmospheric Sciences*, 71(11):4276–4291, 10 2014. ISSN 0022-4928. doi: 10.1175/JAS-D-14-0052.1. URL https://doi.org/10.1175/JAS-D-14-0052.1.

Kenneth R. Sperber. Propagation and the Vertical Structure of the Madden–Julian Oscillation. *Monthly Weather Review*, 131(12):3018–3037, 12 2003. ISSN 0027-0644. doi: 10.1175/1520-0493(2003)131⟨3018:PATVSO⟩2.0.CO;2. URL https://doi.org/10.1175/1520-0493(2003)131<3018:PATVSO>2.0.CO;2.

Justin P. Stachnik, Duane E. Waliser, and Andrew J. Majda. Precursor Environmental Conditions Associated with the Termination of Madden–Julian Oscillation Events. *Journal of the Atmospheric Sciences*, 72(5):1908–1931, 05 2015. ISSN 0022-4928. doi: 10.1175/JAS-D-14-0254.1. URL https://doi.org/10.1175/JAS-D-14-0254.1.

Katherine H. Straub. Mjo initiation in the real-time multivariate mjo index. *Journal of Climate*, 26(4):1130–1151, 2013. doi: 10.1175/JCLI-D-12-00074.1. URL https://doi.org/10.1175/JCLI-D-12-00074.1.

Katherine H. Straub and George N. Kiladis. The observed structure of convectively coupled kelvin waves: Comparison with simple models of coupled wave instability. *Journal of the Atmospheric Sciences*, 60(14):1655–1668, 2003. URL https://doi.org/10.1175/1520-0469(2003)060<1655:TOSOCC>2.0.CO;2.

Taylor. The oscillations of the atmosphere. *Proceedings of the Royal Society of London A: Mathematical, Physical and Engineering Sciences*, 156(888):318–326, 1936. ISSN 0080-4630. URL http://rspa.royalsocietypublishing.org/content/156/888/318.

Christopher Torrence and Gilbert P. Compo. A practical guide to wavelet analysis. *Bulletin of the American Meteorological Society*, 79(1):61–78, 1998. URL https://doi.org/10.1175/1520-0477(1998)079<0061:APGTWA>2.0.CO;2.

Kevin E. Trenberth, John T. Fasullo, and Jessica Mackaro. Atmospheric Moisture Transports from Ocean to Land and Global Energy Flows in Reanalyses. *Journal of Climate*, 24 (18):4907–4924, 09 2011. ISSN 0894-8755. doi: 10.1175/2011JCLI4171.1. URL https://doi.org/10.1175/2011JCLI4171.1.

Stefan N. Tulich, David A. Randall, and Brian E. Mapes. Vertical-mode and cloud decomposition of large-scale convectively coupled gravity waves in a two-dimensional cloud-resolving model. *Journal of the Atmospheric Sciences*, 64(4):1210–1229, 2007. URL https://doi.org/10.1175/JAS3884.1.

John M. Wallace. General circulation of the tropical lower stratosphere. *Reviews of Geophysics*, 11(2):191–222, 1973. ISSN 1944-9208. URL http://dx.doi.org/10.1029/RG011i002p00191.

John M. Wallace and V. E. Kousky. Observational evidence of kelvin waves in the tropical stratosphere. *Journal of the Atmospheric Sciences*, 25(5):900–907, 1968. URL https://doi.org/10.1175/1520-0469(1968)025<0900:OEOKWI>2.0.CO;2.

B. Wang and H. Rui. Synoptic climatology of transient tropical intraseasonal convection anomalies: 1975?1985. *Meteorology and Atmospheric Physics*, 44(1-4):43–61, January 1990. doi: 10.1007/BF01026810.

Lu Wang, Tim Li, Eric Maloney, and Bin Wang. Fundamental Causes of Propagating and Nonpropagating MJOs in MJOTF/GASS Models. *Journal of Climate*, 30(10):3743–3769, 04 2017. ISSN 0894-8755. doi: 10.1175/JCLI-D-16-0765.1. URL https://doi.org/10.1175/JCLI-D-16-0765.1.

Matthew Wheeler and George N. Kiladis. Convectively coupled equatorial waves: Analysis of clouds and temperature in the wavenumber–frequency domain. *Journal of the Atmospheric Sciences*, 56(3):374–399, 1999. URL https://doi.org/10.1175/1520-0469(1999)056<0374:CCEWAO>2.0.CO;2.

Matthew Wheeler, George N. Kiladis, and Peter J. Webster. Large-scale dynamical fields associated with convectively coupled equatorial waves. *Journal of the Atmospheric Sciences*, 57(5):613–640, 2000. URL https://doi.org/10.1175/1520-0469(2000)057<0613:LSDFAW>2.0.CO;2.

Matthew C. Wheeler and Harry H. Hendon. An All-Season Real-Time Multivariate MJO Index: Development of an Index for Monitoring and Prediction. *Monthly Weather Review*, 132(8):1917–1932, 08 2004. ISSN 0027-0644. doi: 10.1175/1520-0493(2004)132⟨1917:AARMMI⟩2.0.CO;2. URL https://doi.org/10.1175/1520-0493(2004)132<1917:AARMMI>2.0.CO;2.

M.C. Wheeler and H. Nguyen. Tropical meteorology and climate — equatorial waves. In Gerald R. North, John Pyle, and Fuqing Zhang, editors, *Encyclopedia of Atmospheric Sciences (Second Edition)*, pages 102–112. Academic Press, Oxford, second edition edition, 2015. ISBN 978-0-12-382225-3. doi: https://doi.org/10.1016/B978-0-12-382225-3.00414-X. URL https://www.sciencedirect.com/science/article/pii/B978012382225300414X.

D.S. Wilks. *Statistical Methods in the Atmospheric Sciences*. Academic Press. Elsevier Science, 2011. ISBN 9780123850225. URL https://books.google.com/books?id=IJuCVtQ0ySIC.

Jiang Xianan, Eric Maloney, and Hui Su. Large-scale controls of propagation of the madden-julian oscillation. *NPJ Climate and Atmospheric Science*, 3(1), 2020.

Gui-Ying Yang, Brian Hoskins, and Julia Slingo. Convectively coupled equatorial waves. part i: Horizontal and vertical structures. *Journal of the Atmospheric Sciences*, 64(10): 3406–3423, 2007. URL https://doi.org/10.1175/JAS4017.1.

Gui-Ying Yang, Brian J. Hoskins, and Julia M. Slingo. Equatorial waves in opposite qbo phases. *Journal of the Atmospheric Sciences*, 68(4):839–862, 2011a. URL https://doi.org/10.1175/2010JAS3514.1.

Gui-Ying Yang, Brian J. Hoskins, and Julia M. Slingo. Equatorial waves in opposite qbo phases. *Journal of the Atmospheric Sciences*, 68(4):839–862, 2011b. doi: 10.1175/2010JAS3514.1. URL https://doi.org/10.1175/2010JAS3514.1.

Gui-Ying Yang, Brian Hoskins, and Lesley Gray. The influence of the qbo on the propagation of equatorial waves into the stratosphere. *Journal of the Atmospheric Sciences*, 69 (10):2959–2982, 2012. doi: 10.1175/JAS-D-11-0342.1. URL https://doi.org/10.1175/JAS-D-11-0342.1.

Kazuaki Yasunaga and Brian Mapes. Differences between faster versus slower components of convectively coupled equatorial waves. *Journal of the Atmospheric Sciences*, 71(1):98–111, 2014. URL https://doi.org/10.1175/JAS-D-13-03.1.

G. Udny Yule. On the theory of correlation for any number of variables, treated by a new system of notation. *Proceedings of the Royal Society of London. Series A, Containing Papers of a Mathematical and Physical Character*, 79(529):182–193, 1907. ISSN 09501207. URL http://www.jstor.org/stable/92723.

Chidong Zhang. Madden-julian oscillation. *Reviews of Geophysics*, 43(2), 2005. doi: 10.1029/2004RG000158. URL https://agupubs.onlinelibrary.wiley.com/doi/abs/10.1029/2004RG000158.

Chidong Zhang and Steven P. Anderson. Sensitivity of Intraseasonal Perturbations in SST to the Structure of the MJO. *Journal of the Atmospheric Sciences*, 60(17):2196–2207, 09 2003. ISSN 0022-4928. doi: 10.1175/1520-0469(2003)060⟨2196:SOIPIS⟩2.0.CO;2. URL https://doi.org/10.1175/1520-0469(2003)060<2196:SOIPIS>2.0.CO;2.

Chidong Zhang and Min Dong. Seasonality in the Madden–Julian Oscillation. *Journal of Climate*, 17(16):3169–3180, 08 2004. ISSN 0894-8755. doi: 10.1175/1520-0442(2004)017⟨3169:SITMO⟩2.0.CO;2. URL https://doi.org/10.1175/1520-0442(2004)017<3169:SITMO>2.0.CO;2.

Chongbo Zhao, Tim Li, and Tianjun Zhou. Precursor signals and processes associated with mjo initiation over the tropical indian ocean. *Journal of Climate*, 26(1):291–307, 2013. doi: 10.1175/JCLI-D-12-00113.1. URL https://doi.org/10.1175/JCLI-D-12-00113.1.

Hongyan Zhu and Harry H. Hendon. Role of large-scale moisture advection for simulation of the mjo with increased entrainment. *Quarterly Journal of the Royal Meteorological Society*, 141(691):2127–2136, 2015. doi: 10.1002/qj.2510. URL https://rmets.onlinelibrary.wiley.com/doi/abs/10.1002/qj.2510.